**Cover Page**

# Final Scientific/Technical Report

Award Number: DE-NE0008264
Recipient names: Virginia Polytechnic Institute and State University
Pacific Northwest National Laboratory
Idaho National Laboratory

Project title: **SiC-ODS Alloy Gradient Nanocomposites as Novel Cladding Materials**

Principal investigator: Kathy Lu, PhD, Professor
Materials Science and Engineering
Virginia Tech
213 Holden Hall, M/C 0237
Blacksburg, Virginia 24061
Email: klu@vt.edu
Tel: +1 540 231 3225; Fax: +1 540 231 8919

Co-PI: Thak Sang Byun, thaksang.byun@pnnl.gov, 509-371-6490,
Pacific Northwest National Laboratory

Co-PI: Isabella van Rooyen, isabella.vanrooyen@inl.gov, 208-526-4199,
Idaho National Laboratory

Project period start and end dates
10/01/2014-9/30/2018

Report submission date: 12/30/2018

Reporting period start and end dates
October 01, 2014 - September 30, 2018

## Table of Contents

## 1. Comparison of actual project accomplishments with project goals and objectives

| **Planned Milestones** | **Actual Accomplishments** |
|---|---|
| Design and creation of novel SiC-ODS alloy cladding nanocomposites with gradient compositions through colloidal processing and layer deposition.<br>Novel SiC-ODS gradient nanocomposites are designed and created. Procedures for producing such nanocomposites are made available**.** | Oxide dispersion strengthened (ODS) steel (9Cr nanostructured ferritic alloy (NFA)) has been synthesized and the particle size distribution has been characterized. The SiC particle size distribution is narrow and is within the desired range. Large and heavy ODS particles can be successfully suspended in the SiC particle suspensions. Viscosities of ODS-SiC co-suspensions with different solids loadings have been measured and the suspensions are feasible for casting purpose. Different ratios of SiC to ODS suspensions have been successfully made. Gradient SiC-ODS composites are cast and their optical images show the designed gradient structures with multiple layers of varying SiC/ODS ratios.<br>SiC-NFA composites of 3 vol% NFA, 45 vol% NFA, and 70 vol% NFA have been successfully prepared by co-suspension casting and spark plasma sintering with more than 90% relative density.<br>Pure SiC, high SiC content SiC-NFA composites (also named 0NFA, 2.5NFA and 5NFA), pure NFA, and high NFA content SiC-NFA composites (also named 100NFA, 97.5NFA and 95NFA) have been spark plasma sintered. The sintered samples show full or close to full densities. The microstructures show pore shrinkage and shape changes to spherical. The crystal structure of the sintered samples has been characterized by X-ray diffraction.<br>In order to avoid the severe reaction between SiC and NFA during the sintering process, a Cr coating on NFA powders is applied and studied under different conditions. The coating morphology and Cr content under different conditions are examined by SEM and EDS respectively. $CrCl_3$, pH, and coating temperatures are the most important factors to consider and the optimal condition for each parameter is obtained. |

| | |
|---|---|
| Thermal treatment of the designed SiC-ODS composites; investigation of corrosion resistance under high temperature water vapor; assessment of microstructural and mechanical features of the composites; evaluation of irradiation damage. | Pure nanostructured ferritic steel alloy (NFA) and NFA–silicon carbide (SiC) composites with different compositions (97.5 vol% NFA-2.5 vol% SiC and 95 vol% NFA-5 vol% SiC) have been sintered by spark plasma sintering (SPS) and systematically investigated based on XRD, SEM, density, Vickers hardness, and nano-hardness.<br>Silicon carbide-nanostructured ferritic alloy composites (SiC-NFA) have been sintered at 1950°C-2100°C by spark plasma sintering (SPS). The influence of NFA addition on the sintered SiC-NFA composites has been investigated based on densification, phase, microstructure, and mechanical property.<br>To prevent the reaction between NFA and SiC, the Cr and C layers have been coated on the NFA powders via electroless coating and solution coating method, respectively, and $Cr_3C_2$ coating on SiC particles has been achieved through a salt melt coating approach.<br>SPS sintering of SiC-NFA composites with C and $Cr_3C_2$ barriers is implemented; high density and Vicker hardness are obtained; phase composition, microstructure, elemental distribution are investigated; the fundamental understanding of the microstructural evolution is explored. |
| Nanocomposite microstructure characterization, mechanism study of nuclear cladding material evolution and degradation in actual nuclear irradiation environments, effective strategies to mitigate/reduce undesirable cladding behaviors. | Characterization of the $Cr_3C_2$@SiC-NFA composites related to the elemental ratio of Si/Fe in the matrix region and the reaction region is further conducted. The effectiveness of the carbon barrier is assessed based on the comparison between SiC-C@NFA and SiC-NFA composites.<br>The results on the experimental and theoretical simulation efforts on the ion irradiation of the SiC-NFA composites are obtained. Self-ion irradiation for high NFA and high SiC samples is completed with a targeted damage of 100 dpa under an incident ion energy of 50 MeV at room temperature. Surface morphologies of the $Fe^{++}$ irradiated high NFA sample are examined under SEM. Based on the molecular dynamics algorithm of |

| | |
|---|---|
| | SRIM 2013 software, the simulation models for both pure NFA and SiC are developed, distributions of implanted self-ion and induced recoil are generated, the energy transfer between incident ions and recoils are obtained, damage profiles are further predicted to be consistent with the experimental expectation. Damage profiles are explored for Si diffusion in NFA using SRIM simulation in order to assess the impact of Si on irradiation tolerance.<br>Ion irradiation resistance and oxidation resistance of novel SiC-NFA cladding composites are investigated. Ion irradiation resistance of pure NFA and SiC-NFA composites up to ~100 dpa is studied along with complementary SRIM simulation. The damage profile and the energy transfer process during the ion irradiation are discussed based on the SRIM simulation.<br>For the oxidation resistance study, the $Cr_3C_2$@SiC-NFA composites are oxidized in a water vapor containing atmosphere at $500^oC$-$1000^oC$ for 50 hrs. Oxidation resistance is investigated based on weight gain and oxide scale thickness.<br>Ion irradiated NFA-SiC composites and water vapor treated $Cr_3C_2$@SiC-NFA composites are studied in order to understand their irradiation and oxidation resistance. For the NFA-SiC composites, 5 MeV Si++ implementation, SRIM simulation, Bradley-Harper (B-H) theory, defect rate modeling, and TEM/EDS characterization have been combined to reveal the microstructural characteristics of the composites and offer the fundamental understanding.<br>The oxidation behavior of SiC-C@NFA composites and the irradiation resistance of $Cr_3C_2$@SiC-NFA composites are investigated and fundamentally understood by combining thermal dynamic analysis and SRIM simulation. The oxidation treatment has been performed in a water vapor containing atmosphere (air + 45 vol% $H_2O$) at 500-$1000^oC$. |

| | |
|---|---|
| Electron back scatter diffraction (EBSD) is used to obtain crystallographic information about the phase distribution and identify any new phases formed in the matrix and at the SiC-ODS interface. | Based on the EBSD results, the NFA additions pin the grain boundaries to prevent grain growth during the high-temperature SPS process. Phase transformation from 6H to 4H SiC has been identified in all three samples and occurs most probably during the high-temperature fabrication. Further, the quantity of 4H-SiC grains increases with increasing NFA content (up to 10%) because of the increasingly excess NFA sites. A random crystallographic distribution of 6H and 4H-SiC grains is determined for all three samples, although a slight indication of preference orientation in the pure SiC sample for 4H-SiC is noted.<br>Nanoindentation with multi cycle loading mode is conducted to explore the mechanical response of the $Cr_3C_2$@SiC-NFA material. The nanohardness data as a function of indentation depth in the reaction region and the NFA matrix of the $Cr_3C_2$@SiC-NFA material before and after the ion irradiation have been obtained. Both the NFA matrix and the reaction region have reduced hardness with the ion irradiation. This is probably because the ion irradiation further reduces the dislocation density and compromises the mechanical properties.<br>Molten salt synthesis method (which is commonly used for preparation of nanoparticles) is successfully used for preparing a homogeneous and dense $Y_2O_3$ coating on SiC. Investigation of the 1150$^oC$ sintered $Y_2O_3$@SiC-NFA composite using XRD shows that the $Y_2O_3$ coating was successful in suppressing the formation of detrimental iron silicides (FeSi, $Fe_3Si$). The $Y_2O_3$@SiC particles show retention in the composite with marginal dissolution in the NFA matrix. |
| Atom probe tomography is used to examine the new cladding material compositions atom by atom and identify where the species are in the composite and eventually build up the composition distribution in 3D. | The APT technique is successfully applied in determining the chemistry from the NFA phase embedded in the SiC matrix. For the SiC phase, the measured low C content is attributed to the difference in the evaporation field between C and Si. Alternatively, the measured |

| | |
|---|---|
| | stoichiometry for Sample 2 (97.5% SiC-2.5% NFA) and Sample 3 (95% SiC-5% NFA) from the precipitate shows (Fe,Cr):Si~1. For the Sample 3 (95% SiC-5% NFA), Al, Mn, Ti, and W appear to be segregated at the interface of the precipitate and the SiC matrix. |

## 2. Significant results, major findings, key outcomes

Oxide dispersion strengthened (ODS) steel (9Cr nanostructured ferritic alloy (NFA)) has been synthesized and the particle size distribution has been characterized. The particle size distribution of ODS is wide and ranges from 2.98 μm to 394.24 μm. Large particles can be successfully removed by screening. The particle size of SiC is characterized. The SiC particle size distribution is narrow and ranges from 0.17 μm to 19.90 μm and is within the desired range. Large and heavy ODS particles can be successfully suspended in the SiC particle suspension. Viscosities of ODS-SiC co-suspensions with different solids loadings have been measured and the suspensions are feasible for casting purpose. Different ratios of SiC to ODS suspensions have been successfully made. Gradient SiC-ODS composites are cast and their optical images show the designed gradient structures with multiple layers of varying SiC/ODS ratios.

SiC-NFA composites of 3 vol% NFA, 45 vol% NFA, and 70 vol% NFA have been successfully prepared by co-suspension casting and spark plasma sintering with more than 90% relative density. The XRD results of the as-sintered 45 vol% NFA-SiC and 70 vol% NFA-SiC composites show diffraction peaks from $Fe_3Si$, $Fe_5Si_3$, and $CrSi_2$, which means that SiC reacts with NFA. The microstructure of the 45 vol% NFA-SiC composite confirms the reactions. Two solutions, using a lower sintering temperature or putting a Cr coating on NFA powders, are suggested to reduce and/or avoid the reaction. The XRD results of the as-sintered 3 vol% NFA-SiC composite do not show any peaks except for those related to SiC. The fracture surface shows that the sintering temperature plays a more important role than the holding time in the 3 vol% NFA-SiC composite. Sintering at 2025°C with 5 min holding under an 80 MPa pressure yields 96% relative density for the 3 vol% NFA-SiC composite.

Pure SiC, high SiC content SiC-NFA composite (also named 0NFA, 2.5NFA and 5NFA), pure NFA, and high NFA content SiC-NFA composite (also named 100NFA, 97.5NFA and 95NFA) samples have been spark plasma sintered. Density measurement and microstructure characterization from well-polished samples are carried out in order to understand the effect of sintering temperature and sample composition on densification. The sintered samples show full or close to full densities. The microstructures show pore shrinkage and shape changes to spherical. The crystal structure of the sintered samples has been characterized by X-ray diffraction. No reaction between SiC and NFA is detected.

In order to avoid the severe reaction between SiC and NFA during the sintering process, a Cr electroless coating on NFA powders is applied and studied under different conditions. The coating morphology and Cr content under different conditions are examined by SEM and EDS respectively. $CrCl_3$, pH, and coating temperature are the most important factors to consider and the optimal condition for each parameter is obtained.

Pure SiC and high SiC content samples (0 vol% NFA-100 vol% SiC, 2.5 vol% NFA-97.5 vol% SiC, and 5 vol% NFA-95 vol% SiC samples) have been successfully sintered by spark plasma sintering (SPS). The density, crystal structure, and microstructure are systematically studied. The hardness is quantified using nanoscale array nanoindentation. The density increases as the sintering temperature increases and the addition of 2.5 vol% NFA increases the density of the composites, while the addition of 5 vol% NFA decreases the density of the composites. The hardness is not affected by the sintering temperature above 1950ºC. The addition of NFA does not decrease the hardness of the SiC matrix, while the iron-rich phase has a lower hardness. Reactions between NFA and SiC lower the hardness.

Pure nanostructured ferritic steel alloy (NFA) and silicon carbide (SiC)-NFA composites with different compositions (97.5 vol% NFA-2.5 vol% SiC and 95 vol% NFA-5 vol% SiC) have been successfully sintered by spark plasma sintering (SPS). The density, crystal structure, microstructure, and mechanical properties of the samples are systematically studied. The density increases with the sintering temperature and the addition of SiC lowers the density of the composites. All the samples are well crystallized even though no SiC can be detected by X-ray diffraction. The microstructure of the sample agrees with the density results. Secondary phases from the reactions between NFA and SiC are detected. The hardness is affected by three factors: sintering temperature, composition, and microstructure (grain boundary, secondary phases, and phase transformation). The hardness generally increases with the sintering temperature. Reactions between NFA and SiC lower the hardness. The $\alpha \rightarrow \gamma$ iron phase transformation also lowers the hardness since $\gamma$-iron has a smaller hardness than $\alpha$-iron. The tensile strength has the same trend as the hardness. The addition of SiC decreases the elastic modulus of the composites.

A Cr layer is deposited on the NFA powder via electroless coating, and three parameters: temperature, $CrCl_3$ concentration, and pH value, have been studied. Higher temperature and higher $CrCl_3$ concentration lead to higher Cr content for the coated NFA powders, and pH value has complex effects on the quality of the Cr coating layer. The mechanism of the electroless coating and these effects have also been studied. Finally, an optimal coating condition has been provided.

After water vapor treatment of high NFA composites, the outer surface evolves into $Fe_2O_3$ through breakaway oxidation without forming $Cr_2O_3$. The morphology exhibits flake-donut-stub transformation with varied growth orientation at different water vapor temperatures. The inner layer is oxidized to $(Fe,Cr)_3O_4$ with $SiO_2$ formation for the NFA-SiC composites. The total thickness of the oxidation layer is related to the sample density, composition, and thermal treatment temperature. γ-Fe precipitation in the pure NFA sample accelerates the oxidation corrosion. The NFA-SiC composites show much improved corrosion resistance, particularly for the high density samples, through the oxidation of SiC and thus $SiO_2$ formation. The NFA-SiC composites have great nuclear application potentials in the harsh moist environments.

After water vapor treatment of the high SiC composites, a new $SiO_2$ phase is produced by oxidation of the matrix SiC and the products of iron silicides. Due to the strong thermal stability of SiC and iron silicides and their corrosion resistance to water vapor, however, no continuous $SiO_2$ layers are detected. The morphology investigation shows that water vapor modifies the fracture surface by oxidizing the carbon enriched phases and pores are formed. The iron enriched domains are still maintained by the protective $SiO_2$ layer which is derived from the oxidation of iron silicides. High SiC samples are extremely corrosion resistant in high moisture environments.

A carbon coating on individual NFA particles (C@NFA) is applied to act as a reaction barrier during sintering. The carbon barrier is effective in preventing reactions at $< 1050^{o}C$ for pressureless sintering, but only at $<850^{o}C$ for spark plasma sintering (SPS) sintering. The SPS sintered SiC-C@NFA composites have high relative densities, which also show an increasing trend with the SiC content. Although the SiC phase is absent, the hardness of the composites reaches 4-7 GPa. The decomposition of SiC leads to two types of regions in the composites, the NFA matrix and the free carbon containing reaction region, both of which contain extra Si element. The effectiveness of the carbon barrier between SiC and NFA is verified based on the phase diagram analysis. The sintered SiC-C@NFA composites offer a potential system for nuclear cladding.

The $Cr_3C_2$@SiC powder is created by introducing a chromium carbide ($Cr_3C_2$) barrier layer on the SiC particle surfaces. Spark plasma sintering (SPS) of composites of 5 vol% $Cr_3C_2$@SiC-95 vol% NFA, 15 vol% $Cr_3C_2$@SiC-85 vol% NFA, and 25 vol% $Cr_3C_2$@SiC-75 vol% NFA is conducted. The $Cr_3C_2$@SiC-NFA composites can achieve the relative densities higher than 96% and comparable Vickers hardness of 5-6 GPa at 950$^{o}$C. The main phase for the composites is maintained to the original α-Fe (BCC) structure without the presence of SiC. In the reaction region, free carbon aggregates are detected, while in the NFA matrix region, silicon element is detected due to the diffusion process. The as-sintered $Cr_3C_2$@SiC-NFA composites are expected to be promising cladding materials in the harsh nuclear environments.

Characterization of the $Cr_3C_2$@SiC-NFA composites related to the elemental ratio of Si/Fe in the matrix region and the reaction region is further conducted. The effectiveness of the carbon barrier is assessed based on the comparison between SiC-C@NFA and SiC-NFA composites.

Results on the experimental and theoretical simulation efforts on the ion irradiation of the SiC-NFA composites are obtained. Self-ion irradiation for high NFA and high SiC samples is completed with a targeted damage of 100 dpa under an incident ion energy of 50 MeV at room temperature. Surface morphologies of the $Fe^{++}$ irradiated high NFA sample are examined under SEM. Based on the molecular dynamics algorithm of SRIM 2013 software, the simulation models for both pure NFA and SiC are developed, distributions of implanted self-ion and induced recoil are generated, the energy transfer between incident ions and recoils are obtained, damage profiles are further predicted to be consistent with the experimental expectation. Damage profiles are explored for Si diffusion NFA using SRIM simulation in order to assess the impact of Si on irradiation tolerance. It is found that the diffusion of Si has the ability to slightly lower the displacement damage. Therefore, it is expected that the as-sintered SiC-NFA composites have better ion irradiation tolerance.

Ion irradiation resistance and oxidation resistance of the SiC-NFA cladding composites are investigated. Study of ion irradiation resistance of pure NFA and SiC-NFA composites up to ~100 dpa along with complementary SRIM simulation has been carried out. The damage profile and the energy transfer process during the ion irradiation are discussed based on the SRIM simulation. The material surfaces are damaged to high roughness with nano-cavities, which can be explained by the Bradley–Harper (B-H) model. The NFA matrix shows ion irradiation induced defect clusters and dislocation loops, while the crystalline structure is maintained. Si diffusion in the NFA matrix decreases ion irradiation induced displacement damage. Reaction products of $Fe_3Si$ and $Cr_{23}C_6$ are identified in the SiC-NFA composites, with the former having a crystalline structure but the latter having an amorphous structure. Fundamental understanding of the ion irradiation induced damage for NFA, $Fe_3Si$, and $Cr_{23}C_6$ is obtained based on the defect reaction rate thory.

For the oxidation resistance study, the $Cr_3C_2$@SiC-NFA composites are oxidized in a water vapor containing atmosphere at 500$^o$C-1000$^oC$ for 50 hrs. Oxidation resistance is investigated based on weight gain and oxide scale thickness. Weight gain data show considerable increase in oxidation resistance with increasing $Cr_3C_2$@SiC content. The samples treated at 1000$^o$C exhibit higher oxidation compared to those at lower temperatures. The composite with 5 vol% $Cr_3C_2$@SiC shows hematite ($Fe_2O_3$) with preferentially oriented rib-type surface morphology. The composites with 15 and 25 vol% $Cr_3C_2$@SiC exhibit hematite + chromium rich spinel phase ($FeCr_2O_3$) and chromium iron oxide ($Fe_{0.7}Cr_{1.3}O_4$) respectively. Improved corrosion resistance for higher $Cr_3C_2$@SiC content samples is attributed to the formation of an amorphous $SiO_2$ middle layer due to SiC oxidation.

For the NFA-SiC composites, 5 MeV Si++ implementation, SRIM simulation, Bradley-Harper (B-H) theory, defect rate modeling, and TEM/EDS characterization have been combined to reveal the microstructural characteristics of the composites and offer fundamental understanding. It is found that the pure SiC is susceptible to ion irradiation and completely amorphizes under 110 dpa dose, while the $(Fe,Cr)_3Si$ phase in the composites exhibits outstanding irradiation resistance. For the water vapor treatment, the cross-sectional microstructure and phase composition are explored and the fundamental understanding based on the Thermo-Calc simulation is achieved in order to explain the oxidation resistance. A three-layer cross-section structure is observed with $Fe_2O_3/(Fe,Cr)_2O_3$ phases in the outer layer, $Fe_3O_4$ phase in the middle layer, and $Fe_3O_4+FeCr_2O_4+Fe_2W+Fe_2SiO_4$ phases in the inner layer. The high diffusivities of Cr and Si are critical factors for creating the protective layer ($Cr_2O_3$ + $SiO_2$), which is responsible for delaying the onset of breakdown oxidation in the 15 and 25 vol% $Cr_3C_2$@SiC composites.

The oxidation behavior of the SiC-C@NFA composites and the irradiation resistance of the $Cr_3C_2$@SiC-NFA composites are investigated and fundamentally understood by combining thermal dynamic analysis and SRIM simulation. The oxidation treatment is performed in a water vapor containing atmosphere (air + 45 vol% $H_2O$) at 500-1000$^o$C. An outer Fe-rich layer and an inner Cr-rich layer, as well as internal oxidation along grain boundaries are found in the SiC-C@NFA composites. The improved oxidation resistance for the higher SiC content composites is attributed to a delay in ‘breakaway oxidation’ due to improved kinetics for the formation of dense $Cr_2O_3$ and $SiO_2$ protective layers. The irradiation with highly energetic $Fe^{++}$ ions at room temperature has been carried out to induce a peak damage of ~200 dpa. Elemental distribution, phase composition, and defect structure are studied in order to understand the ion irradiation response. SRIM simulation reveals the damage profiles for different phase compositions. The

NFA|$_{Si}$ phase has good ion irradiation resistance with dislocation loops induced. The C phase in the NFA|$_{Si}$ matrix is prone to being partially amorphized whereas the $Cr_3C_2$ phase in the NFA|$_{Si}$ matrix is completely amorphized. These results offer important guidance for nuclear cladding material development.

Ion irradiation on spark plasma sintered (SPSed) SiC and NFA-SiC materials is carried out using 5 MeV $Si^{++}$ ions at $2.2\times10^{18}$ ions·cm$^{-2}$ fluence and characterized based on scanning electron microscopy (SEM) and Raman spectroscopy in order to understand their irradiation resistance behaviors. The surface of the samples experiences a dramatic change with the creation of well-defined dune shape microstructures, which can be explained based on the Bradley-Harper (B-H) model. The irradiation induced damage layer has a consistent thickness and agrees with the result from the SRIM simulation. Complete amorphization occurs for the SiC phase, while a crystalline structure is maintained for the $Fe_3Si$ phase.

The understanding of microstructural evolution of spark plasma sintered nanostructured ferritic alloy (NFA) and 25 vol% $Cr_3C_2$ coated SiC ($Cr_3C_2$@SiC)-NFA composite under thermal treatment at 1000°C is explored from fundamental science point of view. Unique spinodal type microstructure with distinct Cr-rich and Si-rich phases has been observed for the 25 vol% $Cr_3C_2$@SiC-NFA composite. Grain sizes are significantly smaller for the 25 vol% $Cr_3C_2$@SiC-NFA composite compared to the pure NFA, which can be attributed to the presence of grain boundary laves phases in the composite sample. Microstructure features can be directly correlated with the dissolution kinetics and phase diagrams calculated using Thermo-Calc/Dictra®. The current finding in the $Cr_3C_2$@SiC-NFA composite offers a useful guidance for developing new cladding materials.

Advanced characterization is performed on three samples: pure SiC (0 vol% Nanostructured Ferritic Alloys [NFA]-100 vol% SiC, Sample 1) and NFA-SiC composites (2.5 vol% NFA-97.5 vol% SiC, Sample 2; and 5 vol% NFA-95 vol% SiC, Sample 3). All three samples are densified by spark plasma sintering (SPS) at 2100°C and achieved high relative density between 94 and 99%. Advanced characterization using scanning electron microscopy (SEM) and electron backscatter diffraction (EBSD) has been performed on the three unirradiated samples.

SEM and subsequent digital image analysis indicate that higher concentrations of NFA enhance the formation of porosities in the evaluated samples. Elemental Si (< 1%) has been surprisingly identified in the pure SiC sample (Sample 1). The % NFA of Sample 2 (8.66 ± 1.41 NFA) is lower than that of Sample 3 (17.32 ± 1.94% NFA). Thus, digital image analysis validates that the concentration of the NFA dopant on the samples is proportional to the quantification results of the area fraction in the NFA phase.

EBSD results indicate that the NFA additions pin the grain boundaries to prevent grain growth during the high-temperature SPS process. Phase transformation from 6H to 4H SiC is identified in all three samples and occurs most probably during the high temperature fabrication. Further, it seems that the quantity of 4H-SiC grains increases with increasing NFA content (up to 10% for Sample 3) because of the increasing NFA areas. A random crystallographic distribution of 6H and 4H-SiC grains is determined for all three samples, although a slight indication of preference orientation in the pure SiC sample for 4H SiC is noted. This study provides relevant comparative information on the effects that NFA additions have on microstructural and chemical properties, with specific focus on the NFA-SiC interlayer.

Nanohardness of the SiC-NFA reaction regions and the NFA matrix in the 25 vol% $Cr_3C_2$@SiC-75 vol% NFA material before and after the high dose ion irradiation (at University of

Michigan) has been explored. It is found that ion irradiation slightly reduces the hardness of the reaction regions and the NFA matrix.

The APT technique is successfully applied in determining the chemistry from the NFA phase embedded in the SiC matrix. The measured stoichiometry from the precipitates for the 97.5% SiC–2.5% NFA and 95% SiC–5% NFA samples shows a stoichiometry of (Fe,Cr):Si~1. Uniform distribution of impurities of Cr, Al, Ti, V, Mn, and P is found inside the precipitate of the 97.5% SiC–2.5% NFA sample. For the 95% SiC-5% NFA system, Al, Mn, Ti, and W appear to be segregated at the interface of the precipitate and the SiC matrix.

An $Y_2O_3$ coating on the SiC powder has been used as a reaction barrier layer for the SiC-NFA composites. The $Y_2O_3$ coating is prepared using molten salt synthesis. The $Y_2O_3$ coating on SiC ($Y_2O_3$@SiC) can successfully suppress detrimental iron silicide reaction products during sintering of the $Y_2O_3$@SiC-NFA composites. While majority of the SiC powder is retained in the composite, marginal dissolution can be observed from the phase shift in XRD patterns. $Y_2O_3$-@SiC-NFA composites are expected to present combined advantages of both SiC and NFA materials for fuel cladding applications.

For the nanostructured ferritic alloy (NFA) and 25 vol% $Cr_3C_2$ coated SiC ($Cr_3C_2$@SiC)-NFA composite during spark plasma sintering at 950°C and under thermal treatment at 1000°C, a unique bi-phase microstructure with distinct Cr-rich and Si-rich phases has been observed for the 25 vol% $Cr_3C_2$@SiC-NFA composite, while for the NFA sample, the traditional large grain microstructure remains. Grain sizes are significantly smaller for the 25 vol% $Cr_3C_2$@SiC-NFA composite compared to those for the pure NFA, which can be attributed to the presence of grain boundary phases in the composite sample. Microstructure features can be directly correlated with the dissolution kinetics and phase diagrams calculated using Thermo-Calc/DICTRA/PRISMA®.

The composite of SiC and carbon coated nanostructured ferritic alloy (25 vol% SiC-C@NFA) is irradiated with $Kr^{++}$ ions at 1 MeV energy up to 10 dpa at 300°C and 450°C. Microstructures and defect evolution are studied in-situ using the IVEM facility at Argonne National Laboratory. The effect of ion irradiation on various phases such as α-ferrite (NFA) matrix, $(Fe,Cr)_7C_3$, and (Ti,W)C precipitates is evaluated. α-ferrite grains show continuous increase in dislocation density along with spatial ordering (or loop string) of dislocations above 5 dpa irradiation. The size of the dislocation loops at 450°C is higher than that at 300°C. The nucleation and growth of new (Ti,W)C precipitates in α-ferrite grains increase with the ion dose at 450°C. SRIM simulations are carried out to theoretically estimate the dpa damage.

**Keywords:** NFA-SiC; $Cr_3C_2$@SiC-NFA; ion irradiation; thermal treatment; APT; microstructure; hardness; $Y_2O_3$ coating on SiC; SiC-NFA composites; molten salt synthesis; reaction barrier layer, SiC, nanostructured ferritic alloy, metal matrix composite, $M_7C_3$ precipitate, Thermo-Calc, phase, in-situ ion irradiation, irradiation induced precipitation.

## 3. Research activities

<u>In light of the large volume of work conducted, in this final report, only the detailed research activities for the last quarter of the project are reported here. For the work carried out before this period, only the major findings and conclusions are included in this report for brevity.</u>

### 3.1. Introduction

In the radioactive environment of nuclear reactors, all involved structural materials are subject to irradiation damage and aging with operating time [1-8]. High neutron irradiation induced damage not only causes microstructural changes but also deterioration of macroscopic properties, and eventually decrease in the overall performance of nuclear reactors. Irradiation induced point defects [9-12], such as vacancies and interstitials, can easily accumulate and grow to large clusters, stacking faults, dislocation loops, and even cause a crystalline-amorphous transition. Meanwhile, voids, precipitates, segregates, and recrystallization can modify the mechanical performance [13-15]. Cladding materials [16] are expected to not only prevent the release of harmful radioactive neutrons, highly energetic $\alpha$ and $\beta$ particles, and $\gamma$ rays, but also maintain irradiation tolerance, physical and chemical stability, corrosion resistance, and mechanical intensity for half a century and even longer. In addition to the normal operation of the nuclear reactors, the cladding materials should also be robust enough to retain radioactive nuclear fuels in an accidental circumstance. Since a cladding component can be in contact with the coolant, its surface microstructure evolution can influence the flow features of the coolants, which subsequently affect the corrosion behavior and aging of the cladding material.

The viability of advanced nuclear energy systems strongly depends on development of new materials which can not only deliver high performance in aggressive environments at elevated temperatures but also ensure safe operations of nuclear reactors. Nanostructured ferritic alloys (NFAs), a special type of oxide dispersion strengthened (ODS) ferritic steels, are foreseen as promising structural material for both nuclear fission and fusion reactor systems [17-20]. The combination of properties such as resistance to high temperature corrosion, irradiation, and void swelling along with excellent creep and high temperature strength make NFAs very attractive for nuclear applications [21-24].

Silicon carbide (SiC) is widely considered as a candidate material for nuclear reactors. It exhibits high irradiation resistance, excellent high temperature strength, slow oxidation kinetics, and high chemical stability [25-29]. SiC and its composites are being intensely studied for their use in fusion reactors, LWR fuel claddings, and high temperature gas reactors.

Spark plasma sintered composites of SiC and NFA with and without reaction barriers ($Cr_3C_2$ and carbon) were explored in our previous research [30-33] for nuclear reactor claddings. $Cr_3C_2$ coating on SiC and carbon coating on NFA particles were carried out in order to suppress the formation of detrimental reaction products such as iron silicides ($Fe_3Si$, FeSi) [32, 34]. $Cr_3C_2$@SiC-NFA composites showed excellent mechanical and high temperature oxidation properties as reported in our previous studies [32, 35]. Such composites with combined properties of NFA and SiC can serve as a promising candidate for fuel cladding to replace existing Zircalloy based materials.

In this study, microstructural characterization was conducted for $Si^{++}$ ion irradiated SiC and NFA-SiC, which have been studied as nuclear reactor cladding materials. The focus of this work is to understand high dose irradiation effects on their surface morphologies and microstructures. The microstructural evolution of pure NFA and a 25 vol% $Cr_3C_2$ coated SiC ($Cr_3C_2$@SiC) and 75 vol% NFA mixture after spark plasma sintering at 950°C and thermal treatment at 1000$^o$C was carried out in order to have an in depth understanding of this composite as a promising nuclear cladding material. Advanced characterization using scanning electron microscopy (SEM) and electron backscatter diffraction (EBSD) was performed on three unirradiated samples.

## 3.2. Experimental

### 3.2.1. Characterization of pure SiC and NFA- SiC

Pure SiC and 2.5 vol% NFA-97.5 vol% SiC were spark plasma sintered (SPSed) to achieve relative densities of 99% and 96%, respectively, at the temperature of 2100°C. Detailed sintering conditions and sample properties can be found in our previous work [33]. Ion irradiation with a highly energetic 5 MeV $Si^{++}$ ion beam was implemented by controlling the ion flux at $3.2\times10^{13}$ $ions\cdot cm^{-2}\cdot s^{-1}$, temperature at 67°C, and irradiation time at 19 h (total fluence of $2.2\times10^{18}$ $ions\cdot cm^{-2}$), at the Michigan Ion Beam Laboratory (MIBL) of University of Michigan. Before the ion irradiation, the samples were finely polished to mirror finish with diamond polishing papers. SRIM (Stopping and Range of Ions in Matter) simulation [36] was carried out and the damage profiles were determined as shown in Fig. 1. For both the pure SiC and 2.5 vol% NFA-97.5 vol% SiC samples, the displacement damage profiles showed a slowly increasing trend from 45 dpa at the surface to 790 dpa peak at 2.0 µm depth, and a sharp drop to 0 dpa at 2.3 µm depth. Scanning electron microscopy (SEM) was used to observe the surface morphology and cross sectional microstructure. Raman spectroscopy was used to measure the bonding characteristics along the irradiation cross section.

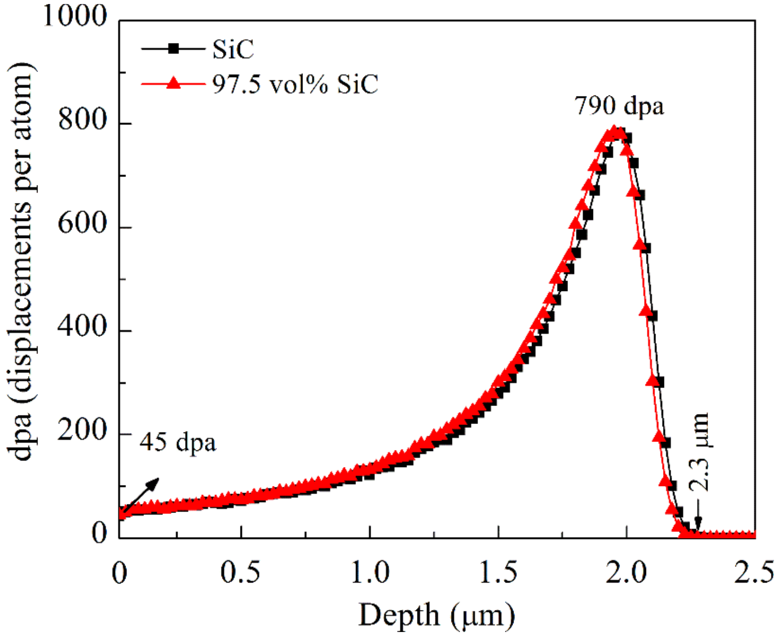

Fig. 1. Displacement damage profiles of the pure SiC and 2.5 vol% NFA-97.5 vol% SiC samples after the ion irradiation.

### 3.2.2. Characterization of pure NFA and $Cr_3C_2$@SiC-NFA

The NFA powder and 25 vol% $Cr_3C_2$@SiC-NFA powder mixture were densified using spark plasma sintering (SPS) at 950$^{o}$C with a heating/cooling rate of 50$^{o}$C/min, applied pressure of 100 MPa, and holding time of 10 minutes. Detailed procedure of creating the $Cr_3C_2$ coating on SiC and the hardness/density results of the $Cr_3C_2$@SiC-NFA sample were reported in our previous reports.

SPS densified NFA and 25 vol% $Cr_3C_2$@SiC-NFA composite were treated at 1000$^{o}$C in an argon atmosphere for 50 h. The thermal treatment was performed in a tube furnace (1730-20 HT Furnace, CM Furnace Inc., Bloomfield, NJ) with a gas flow of ~1.2 L·min$^{-1}$ at 1 atm pressure.

Microstructures were analyzed using scanning electron microscopy in the backscattered mode (FEG E-SEM QUANTA600, FEI Company, Hillsboro, OR, USA) and energy dispersive spectroscopy (BRUKER EDS). An electron backscattered diffraction (TSL/EDAX EBSD) detector attached to a focused ion beam microscope (FIB, Helios Nanolab, FEI Company, Hillsboro, OR, USA) was used to characterize grain size, grain size distribution, and grain boundary misorientation angles. The measurements were performed using 20 kV beam accelerating voltage with 70$^o$ tilt angle to the horizontal axis. EDAX Team software was used to collect data and OIM analysis software was used for post processing and data analysis.

ThermoCalc® and DICTRA® software packages were used to calculate phase diagram and understand the dissolution behaviors of SiC respectively. TCFE9 and MOBFE4 databases were used for these calculations.

### 3.2.3. Characterization of 25 vol% SiC-C@NFA composite

ThermoCalc®, DICTRA®, and PRISMA® software packages were used to calculate phase diagram and understand the dissolution behaviors of SiC and kinetics of new phase formation respectively. TCFE9 and MOBFE4 databases were used for these calculations.

The 25 vol% SiC-C@NFA composite was sintered using SPS at 950$^o$C. The details of the sintering process and the resultant material properties can be found elsewhere [37, 38]. In brief, the composite microstructure contains a matrix with Si-diffused NFA ($NFA_{Si}$), Cr-rich precipitates, and graphite precipitates due to the reactions between SiC and C@NFA. For the TEM sample preparation, the 25 vol% SiC-C@NFA composite sample was cut using a low speed saw (Beuhler Isomet) in order to obtain a 300 μm thick foil. This foil was further polished using 1200 grit papers up to 60 μm thickness. An ultrasonic disc cutter (Fischione 170) was used to obtain multiple discs with a 3 mm diameter. Further thinning was carried out using a low angle ion milling machine

(Fischione 1010 Low Angle Ion Mill). An argon ion source with 3 kV voltage and 5 mA current was used to thin the sample at a $12^o$ angle.

### 3.2.4. Sample preparation for electron back scatter diffraction

Three SEM sample mounts were polished on a series of SiC papers with grit sizes of 240 to 1200. In the final step, the samples were polished with 0.3 µm $Al_2O_3$ abrasive in a water-based suspension using a VibroMet$^{TM}$ vibratory polisher. The EBSD measurements were performed using a FEI Quanta 650 Field Emission Gun SEM. The EBSD data was acquired using TSL OIM software®. The SEM and EBSD settings, as mentioned in Table 1, were used to obtain accurate orientation mapping.

Table 1. Parameters for electron back scatter diffraction measurements.

| | | |
|---|---|---|
| SEM settings | Accelerating voltage | 20 kV |
| | Working distance | ~15 mm |
| | Step size | 0.15 µm |
| EBSD settings | EBSD camera binning mode | 4 × 4 |
| | Phase for acquisition | 4H SiC, 6H SiC |
| | Number of bands detected | 15 |

In the initial EBSD analysis using the TSL OIM analysis software®, a few data cleaning procedures were performed. A grain dilation clean-up step was performed with a grain tolerance angle of 2 degrees and the number of points is greater than 5. Subsequently, the nearest orientation correlation step was performed with a grain tolerance angle of 2 degrees and a minimum confidence index (CI) of 0.1.

### 3.2.5. Nanohardness measurement

The nanohardness was measured with a maximum load of 140 mN based on the multi cycle loading mode (Micro Materials Ltd., Wrexham Technology Park, Wrexham LL13 7YP, UK). The measurement was focused on the NFA matrix and the reaction region of the samples before and after the ion irradiation at University of Michigan (see Section 3.2.1). For each measurement of the NFA matrix and the reaction region, at least 15 nanoindents were implemented. Before the measurement, the sample surfaces were polished with a 50 nm diamond slurry.

### 3.2.6. $Y_2O_3$ coating

A $Y_2O_3$ coating on SiC particles was prepared using a molten salt synthesis method. The SiC powder was etched in a 5% HF solution for 30 minutes to remove oxide impurities on the particle surfaces. Yttrium nitrate hexahydrate ($Y(NO_3)_3.6H_2O$) salt was used as a precursor material for $Y_2O_3$. A SiC powder (0.25 grams) was mixed with $Y(NO_3)_3.6H_2O$ (0.5 grams) precursor salt using a mortar and pestle for 30 minutes. A KCl and NaCl eutectic mixture (44 wt% NaCl) was used as the molten salt for this work. 10 grams of the KCl-NaCl salt powder was added to the above mentioned mixture of SiC and $Y(NO_3)_3.6H_2O$ salt. The entire powder was ball milled using SPEX mill for 15 minutes. The mixture was added to a rectangular alumina crucible (with lid) and treated in an argon atmosphere at 800°C for 4 hours. The treated powders were dissolved in DI water to remove the KCl-NaCl salt while leaving the SiC powder with a $Y_2O_3$ coating. The estimated thickness of the $Y_2O_3$ coating (calculated using weight and density data) was around 300 nm. The powder was washed 5 times in DI water to ensure complete removal of the KCl-NaCl salt. The powder was dried in an oven at 80°C for 12 hours.

The $Y_2O_3$ coated SiC ($Y_2O_3$@SiC) powder was mixed with a NFA (Fe-9Cr-2W-0.2V-0.3$Y_2O_3$) powder at a 25:100 volume ratio using ball milling at low speeds for 15 minutes. Around 1% PAA (polyacrylic acid) was added into the powder mixture as a binder before ball milling. The mixture was compacted using a uniaxial hydraulic press (Carver, Wabash, IN, USA). Sintering of the green samples was carried out in an argon atmosphere at 1150°C for 1 hour using a horizontal tube furnace (1730-20 HT Furnace, CM Furnace Inc., Bloomfield, NJ).

Phase composition analysis of the SiC powder (before and after the molten salt based coating process) and the 1150°C sintered $Y_2O_3$@SiC sample was performed using X-ray diffraction (XRD, PANalytical B.V., Almelo, Netherlands). The $Y_2O_3$ coating quality was examined by observing the surface morphology of the SiC particles before and after the coating process using scanning electron microscopy (FEG E-SEM QUANTA600, FEI Company, Hillsboro, OR, USA).

### 3.2.7. In-situ ion irradiation using TEM

In-situ $Kr^{++}$ ion irradiation was performed with the IVEM-Tandem TEM facility at Argonne National Laboratory (ANL). The acceleration voltage for the in-situ TEM analysis was kept at 300 kV. The $Kr^{++}$ ion accelerating voltage was 1 MeV. The TEM analysis was performed on the un-irradiated (0 dpa) SiC-C@NFA composite and the irradiated sample after dose levels of

0.2, 0.5, 1, 2, 5, and 10 dpa. Detailed analysis was performed after 10 dpa dose using energy dispersive spectroscopy (EDS) and electron diffraction techniques on JEOL 2100 TEM with 200 kV accelerating voltage.

SRIM simulation was performed with a 1 MeV $Kr^{++}$ ion source and the $NFA_{Si}$ phase as the target using the SRIM-2013 (Stopping and Range of Ions in Matter) software. In total, 50,000 incident ions with a $15^o$ incident angle was used for the simulation. The results were used to estimate the dpa level from the corresponding fluence flux of the in-situ incident $Kr^{++}$ ions.

## 4. Results and discussion

### 4.1. Ion irradiation response of NFA-SiC composites

### 4.1.1. Surface microstructures of NFA-SiC after ion irradiation

The surface and cross section microstructures of the pure SiC and 2.5 vol% NFA-97.5 vol% SiC samples after the ion irradiation are shown in Fig. 2. As stated before the ion irradiation, the SPS sintered SiC and 2.5 vol% NFA-97.5 vol% SiC samples have been polished scratch free. After the 45 dpa $Si^{++}$ ion irradiation, the sample surface is heavily eroded and a new morphology with dune-shaped islands forms. The dune structure is uniform with an average diameter of ~5 µm for both the pure SiC and 2.5 vol% NFA-97.5 vol% SiC samples and no abnormal sized shapes are observed in Figs. 2a and c. However, the 2.5 vol% NFA-97.5 vol% SiC sample has a rougher and slightly irregular surface due to the effect from the NFA species. The cross sections of dune shapes for both compositions are presented in Figs. 2b and d. The height of the dune shapes is measured to be ~0.9 µm. Due to the highly energetic interactions of the incident ions and the SiC species, atomic displacement damage is produced and ordered atoms in crystalline SiC lattices are displaced. The boundary between the irradiated and unirradiated regions can be more clearly identified in Fig. 2b because the highly energetic ion irradiation causes extensive microstructure changes in the irradiated region. The thickness of the irradiation damaged layer in the SiC sample is ~2.5 µm as estimated from Fig. 2b, consistent with the SRIM simulated damage depth of 2.3 µm. On the irradiated 2.5 vol% NFA-97.5 vol% SiC sample, relatively bright particles can be observed. These bright particles are the NFA-derived species (iron silicide after sintering) in the NFA-SiC, which has been broken up under the highly energetic ion irradiation.

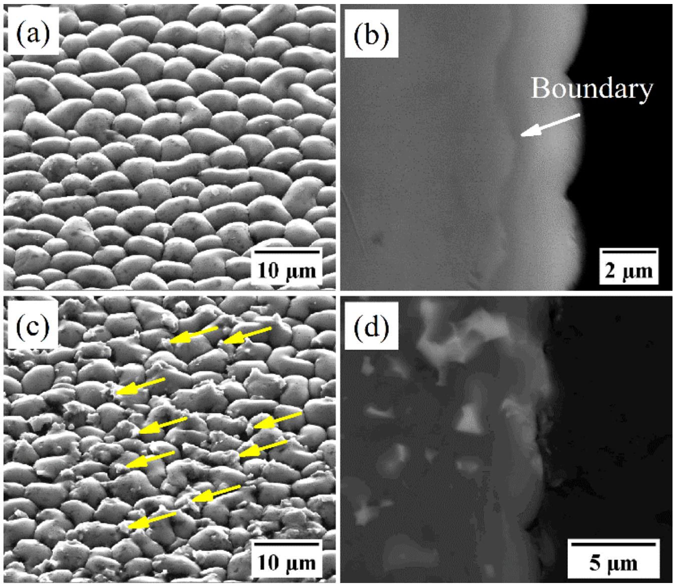

Fig. 2. Surface morphologies (at 52° tilt) and cross section microstructures of the $Si^{++}$ ion irradiated pure SiC (a, b) and 2.5 vol% NFA-97.5 vol% SiC (c, d).

### 4.1.2. Bonding characteristics of NFA-SiC after ion irradiation

Fig. 3a shows the characterization locations for the Raman spectra along the cross section of the irradiated layer in the pure SiC sample. The irradiated layer has a brighter contrast. The corresponding Raman spectra from P1-P4 are shown in Fig. 4. The Raman spectrum from P4, which locates in the unirradiated region, has sharp Raman peaks through the entire spectrum, matching with the observation from literature [39, 40]. The Raman peaks at 151 $cm^{-1}$, 242 $cm^{-1}$, and 507 $cm^{-1}$ are from the acoustic vibration modes of the Si-C bonds, while the other peaks at

769 cm$^{-1}$, 790 cm$^{-1}$, 799 cm$^{-1}$, 890 cm$^{-1}$, 972 cm$^{-1}$, 1516 cm$^{-1}$, 1525 cm$^{-1}$, 1534 cm$^{-1}$, 1548 cm$^{-1}$, 1616 cm$^{-1}$, and 1716 cm$^{-1}$ are attributed to the optical vibration modes of the Si-C bonds. Among all the peaks, the 790 cm$^{-1}$ peak is the most intensive, and the 972 cm$^{-1}$ peak is the second. However, the Raman spectra for P1-P3, which are located within the irradiated layer, exhibit huge difference from that of the unirradiated region. There are four broad peaks. The first and second peaks at 212 cm$^{-1}$ and 464 cm$^{-1}$ are identified to result from the vibrational mode of the Si-Si bonds [41-43]. The third peak centering at 790 cm$^{-1}$ is consistent with the intensive peak from the Raman spectrum at location P4. This peak is from the Si-C bonds as reported [39, 44]. The last one is at 1406 cm$^{-1}$ and derived from the C-C bonds [45-47]. The same Raman peaks are also observed from the 200 keV Ge$^{+}$ induced amorphous 6H-SiC surface [39, 48]. P3 is located at the boundary of the irradiated and unirradiated regions. The small peak at 790 cm$^{-1}$ should be from the crystalline phase. This confirms that the highly energetic irradiation to the SiC matrix leads to phase conversion from crystalline to amorphous. Some of the Si-C bonds have been broken and new Si-Si and C-C bonds have been created.

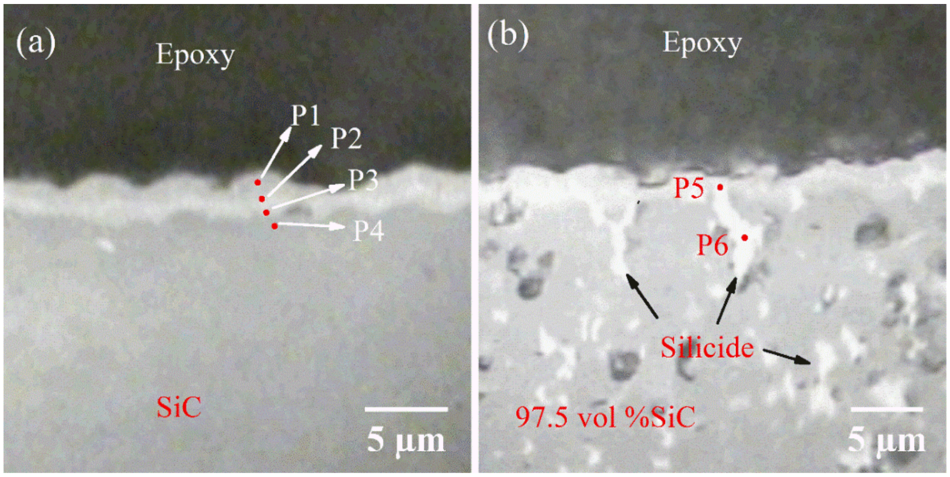

Fig. 3. Raman characterization location in the cross section of the irradiated pure SiC sample (a), and irradiated 2.5 vol% NFA-97.5 vol% SiC (b). The bright contrast layers in both (a) and (b) are caused by irradiation.

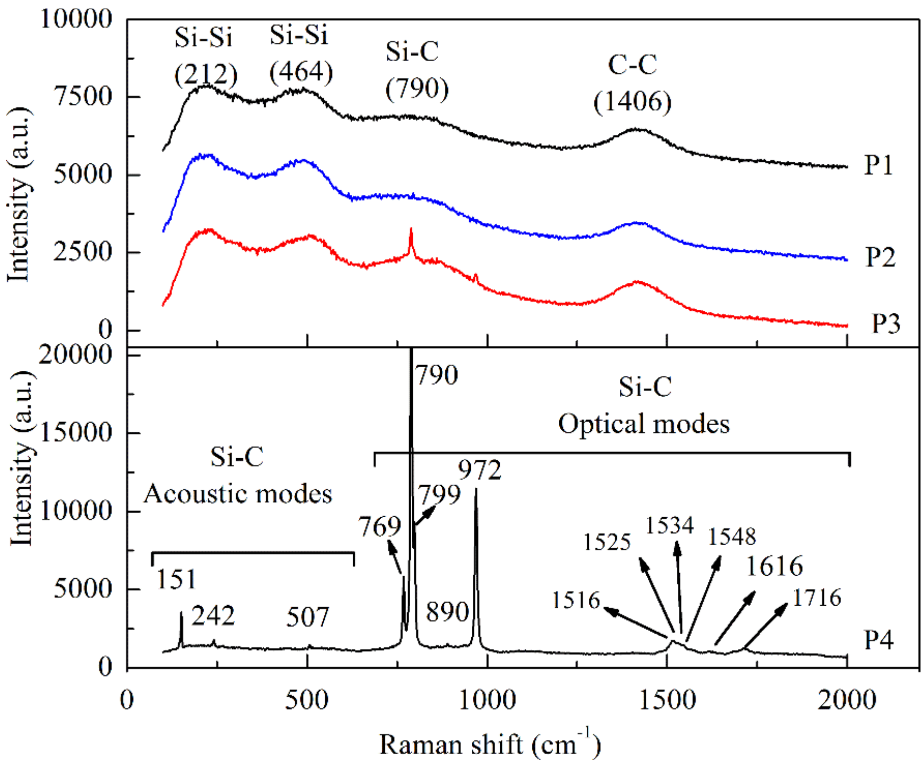

Fig. 4. Raman spectra from point P1-P4 along the cross section from the pure SiC sample as shown in Fig. 3a.

For the 2.5 vol% NFA-97.5 vol% SiC sample, iron silicide with bright contrast is observed as indicated by arrows in Fig. 3b. Its phase has been confirmed to be $Fe_3Si$ by TEM in our previous work [49]. In order to understand the irradiation response of the $Fe_3Si$ phase, point P5 with irradiation and point P6 without irradiation are analyzed using Raman spectroscopy. As shown in Fig. 5, the bright phase $Fe_3Si$ at P5 and P6 has consistent peaks of 189 $cm^{-1}$ and 321 $cm^{-1}$, meaning that the $Fe_3Si$ phase is irradiation resistant.

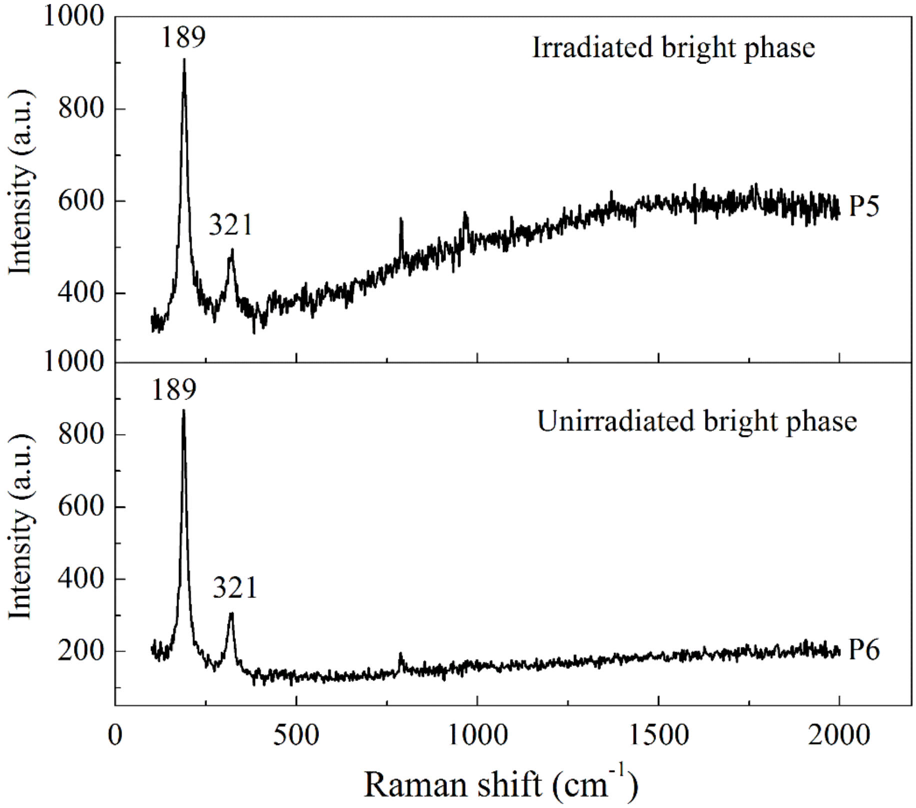

Fig. 5. Raman spectra for points P5 and P6 along the cross section of the 2.5 vol% NFA-97.5 vol% SiC sample as shown in Fig. 3b.

### 4.1.3. Fundamental understanding of ion irradiation in NFA-SiC

The ion irradiation induced surface patterns (microstructures) can be explained based on the Sigmund's theory of sputtering [50, 51] and Bradley-Harper (B-H) model [52]. The interaction of the incident ions with the targeted atoms is a complicated physical process including primary knock-on, collision cascade, energy transfer, interstitial and vacancy creation, enhanced ion diffusion and sputtering, lattice disordering, and amorphization. The combined surface smoothing and roughening effects produce well-defined, periodically arranged micron/submicron patterns, such as ripples and dunes on the ion irradiated surfaces [53-55]. The surface microstructure formation under ion irradiation is also incident angle sensitive [55], with normal incident angle producing dune structures and off-normal incident angle producing stable ripple structures.

The evolution of the surface height h(x, y, t) can be given as follows [56]:

$$\frac{\partial h}{\partial t} = -v_0 + v_x \cdot \frac{\partial^2 h}{\partial x^2} + v_y \cdot \frac{\partial^2 h}{\partial y^2} - D_x \cdot \frac{\partial^4 h}{\partial x^4} - D_y \cdot \frac{\partial^4 h}{\partial y^4} \tag{1}$$

where $v_0$ is the erosion velocity of a flat surface, $v_x$ and $v_y$ are the surface tension coefficients, $D_x$ and $D_y$ are the surface diffusion constants. $v_x$ and $v_y$ are strongly related to ion flux, ion penetration depth, sputtering yield, and surface curvature; while $D_x$ and $D_y$ are dependent on surface diffusivity, surface free energy, thermal energy, and activation energy. At the normal incident angle, the terms $v_x$ and $v_y$ in Eq. (1) have negative values and cause surface roughening, while the terms $D_x$ and $D_y$ in Eq. (1) have positive values and promote atom diffusion and surface smoothening. At the equilibrium state, the isolated dune structure with lateral periodicity is generated.

## 4.2. Microstructures in SPS sintered and thermally treated $Cr_3C_2$@SiC-NFA

### 4.2.1. SPS sintering effects on $Cr_3C_2$@SiC-NFA

Fig. 6 shows the SEM micrographs of the spark plasma sintered NFA and 25 vol% $Cr_3C_2$@SiC-NFA samples. The NFA sample shows mainly equiaxed grains along with some pores at the grain boundaries as indicated in Fig. 6a. The microstructure of the 25 vol% $Cr_3C_2$@SiC-NFA sample shows fine light and dark gray areas arranged in an intertwined fashion similar to those in spinodal decomposition as shown in Fig. 6b. Very fine and bright precipitates can also be seen in the light gray areas of the microstructure (Fig. 6b). These bright precipitates are believed to be ‘laves phases’ [35]. Figs. 7a and b show EBSD inverse pole figure maps of both the NFA and 25 vol% $Cr_3C_2$@SiC-NFA composite respectively. The NFA sample (~12 μm) has far larger grain sizes compared to the 25 vol% $Cr_3C_2$@SiC-NFA composite (~2 μm) as shown in Fig. 7.

Carbon precipitates in the 25 vol% $Cr_3C_2$@SiC-NFA composite cannot be indexed by the EBSD, thus remain as black spots in the inverse pole figure (IPF) maps as shown in Fig. 7b. Grains in the carbon precipitate areas are far smaller than the rest of the grains, resulting in a bimodal grain size distribution. Such small grains are most probably due to the pinning effect of these precipitates. The overall smaller size of the grains in the 25 vol% $Cr_3C_2$@SiC-NFA composite can be attributed to the pinning effects of the bright 'laves phase' precipitates.

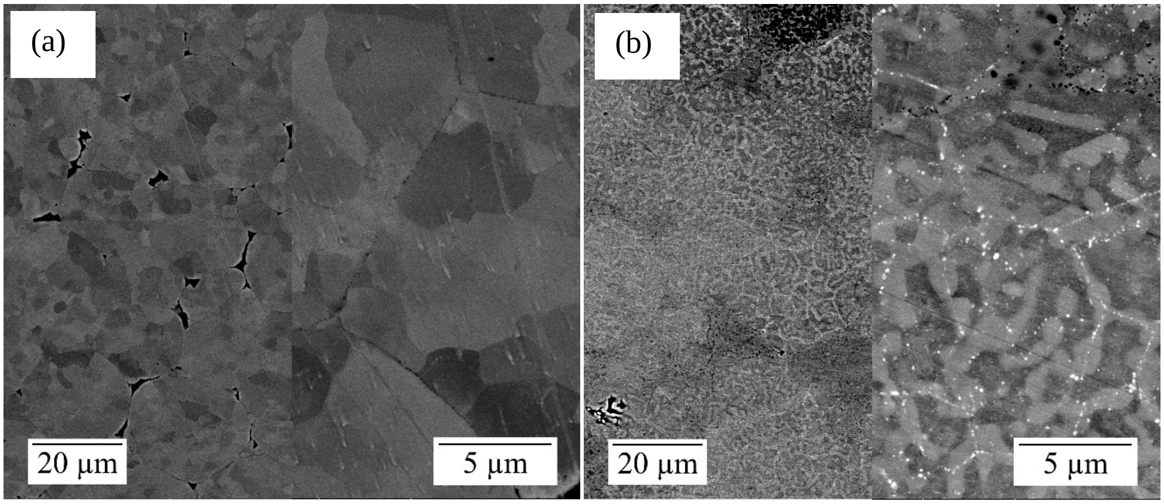

Fig. 6. SEM micrographs of (a) NFA and (b) 25 vol% $Cr_3C_2$@SiC-NFA composite after SPS sintering (the right side is the magnified image of the left side).

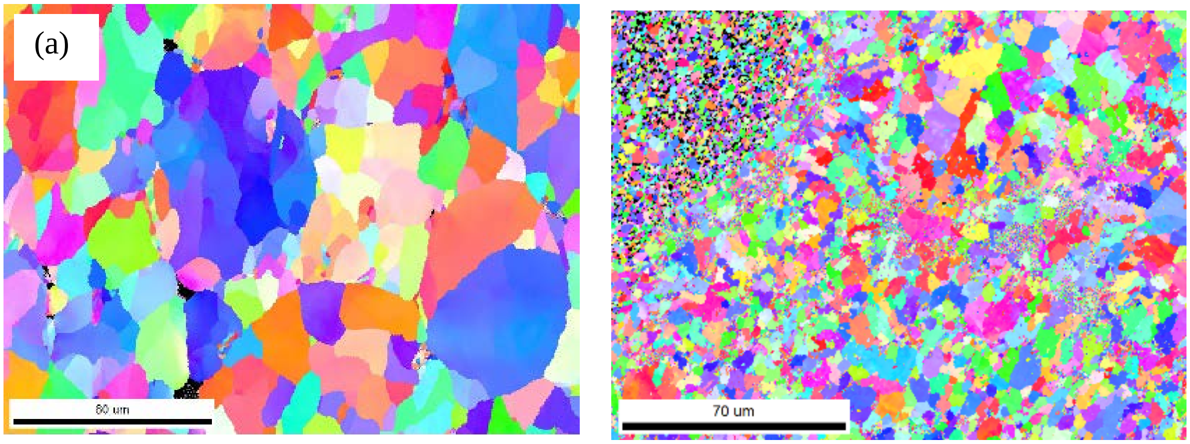

Fig. 7. IPF maps of (a) NFA and (b) 25 vol% $Cr_3C_2$@NFA-SiC composite after SPS sintering showing grain sizes and their distributions (both at the same magnification).

### 4.2.2. Thermal treatment effect on $Cr_3C_2$@SiC-NFA

Fig. 8 shows the microstructures of the NFA and 25 vol% $Cr_3C_2$@SiC-NFA composite after the thermal treatment at 1000°C for 50 h. The NFA sample (Fig. 8) shows mainly grain boundaries. The 25 vol% $Cr_3C_2$@SiC-NFA composite (Fig. 8b) shows similar spinodal type light and dark gray areas, but slightly coarser compared to the sintered microstructure in Fig. 6b. The enlarged microstructure in Fig. 8b shows bright laves phases preferentially aligned along the grain boundaries.

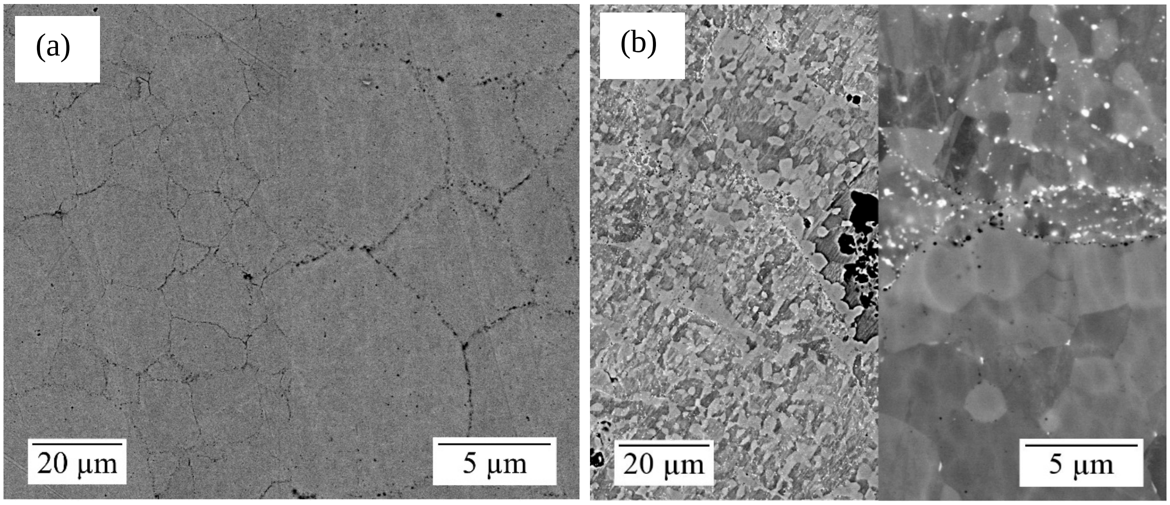

Fig. 8. BSE micrographs of (a) NFA and (b) 25 vol% $Cr_3C_2$@SiC-NFA composites after the thermal treatment at 1000°C for 50 h (the right part is the magnified image of the left part).

The IPF map of the 1000°C treated 25 vol% $Cr_3C_2$@SiC-NFA composite in Fig. 9 shows slight increase in grain size (~4 μm) compared to that of the sintered sample. The grains in the carbon precipitate-rich areas are again far smaller than the rest, similar to what is observed for the sintered composite. All the EBSD images in Figs. 7a, 7b and Fig. 9 have roughly the same magnification.

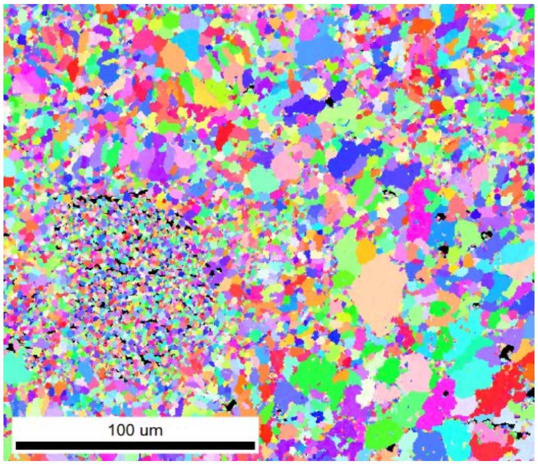

Fig. 9. IPF map of the 25 vol% $Cr_3C_2$@NFA-SiC composite after the thermal treatment at 1000°C for 50 h showing grain sizes and their distribution.

Fig. 10 shows the EDS maps of the 1000°C treated 25 vol% $Cr_3C_2$@SiC-NFA composite. There is obvious segregation of Cr and Si in the matrix. The light gray areas are Cr-rich while the dark gray areas are Si- and Fe-rich.

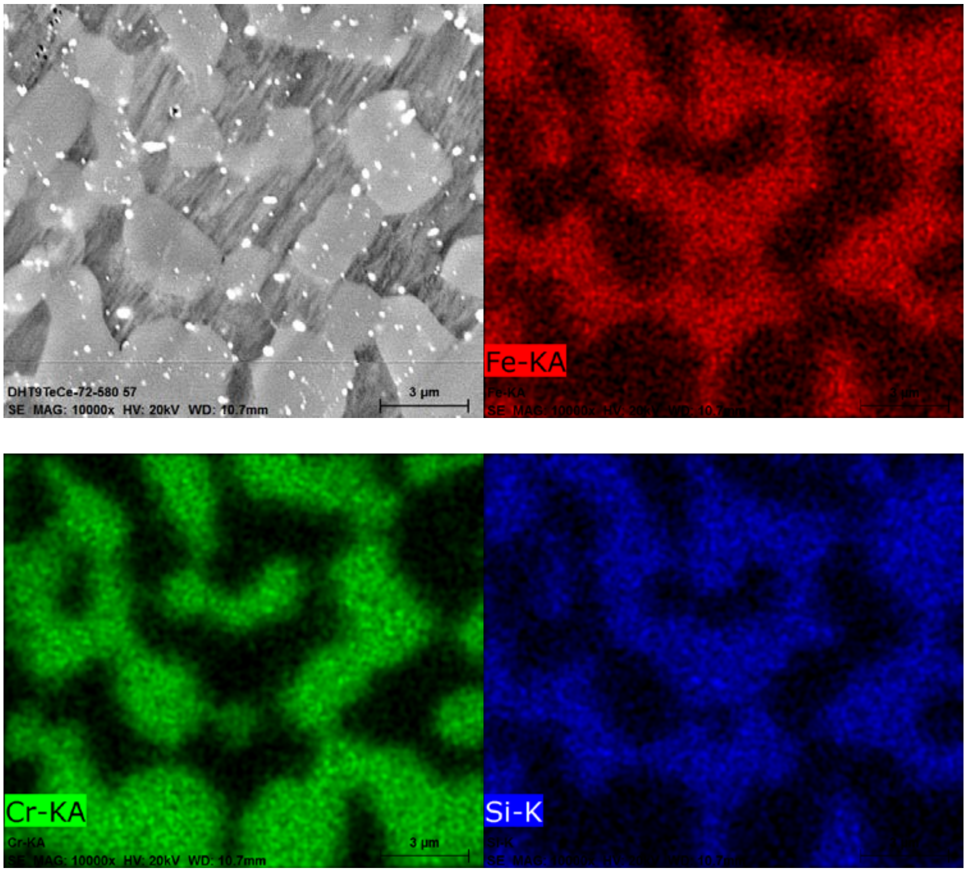

Fig. 10. EDS mapping of the 25 vol% $Cr_3C_2$@SiC-NFA sample after the thermal treatment at 1000$^o$C for 50 h showing Cr and Si segregation.

### 4.2.3. Fundamental understanding from dissolution kinetics

Dissolution kinetics of SiC has been studied using the DICTRA$^®$ software package. As Si diffuses into the NFA matrix, Cr can be seen segregating away from Si. This can be roughly correlated with Cr and Si phase separation seen in Fig. 11.

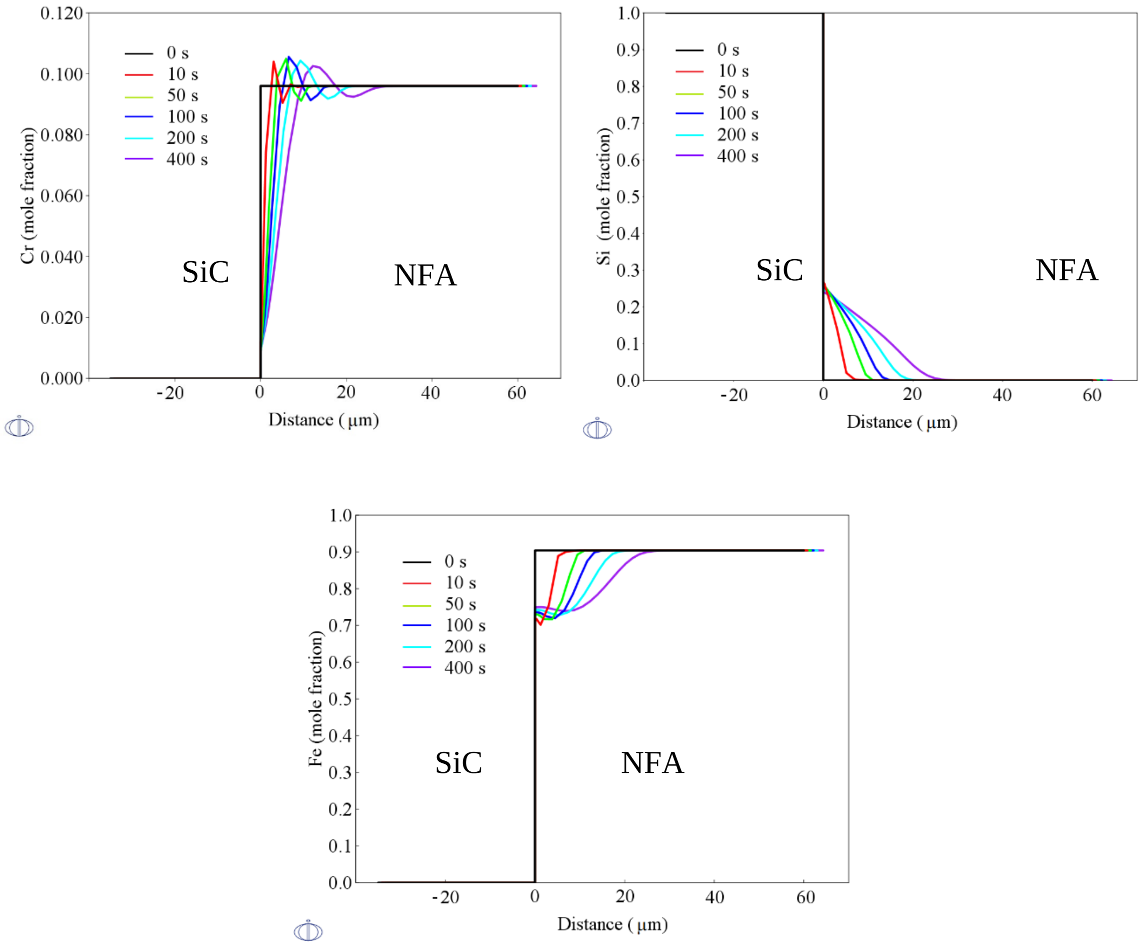

Fig. 11. Dissolution kinetics of SiC grains in the NFA matrix showing (a) Cr, (b) Si, and (c) Fe diffusion behaviors.

### 4.3. Advanced characterization results at INL

Three samples were characterized using SEM, EDS, and EBSD to determine specific features related to the NFA additions and the specific fabrication properties. All preparation and examination were performed at the Center for Advanced Energy Studies (CAES) in the Microscopy and Characterization Suite (MACS).

### 4.3.1. Scanning electron microscopy

Digital image analysis was employed to quantify the compound proportions along with porosities present on the samples (Table 2 with detailed measurements in Appendix A). Fig. 12 displays representative back scatter electron images of the three samples examined. Employing a SEM backscatter electron detector from a JEOL scanning electron microscope (model JSM-6610-LV) coupled with energy dispersive X-ray spectroscopy, along with the guidelines specified on the American Society for Testing and Materials (ASTM) E-1245 [57], the area fractions of the NFA and SiC compounds were estimated with ImageJ® using a total of 60 SEM micrographs. The results indicate that higher concentrations of NFA enhanced the formation of porosities in the evaluated samples. Elemental Si was further identified in Sample 1 (Fig. 12(a)), which is unexpected. The percentage of NFAs based on the image analysis of Sample 2 in Fig. 12(b) (8.66 ± 1.41%), is lower than those of Sample 3 in Fig. 12(c) (17.32 ± 1.94%) with larger precipitates.

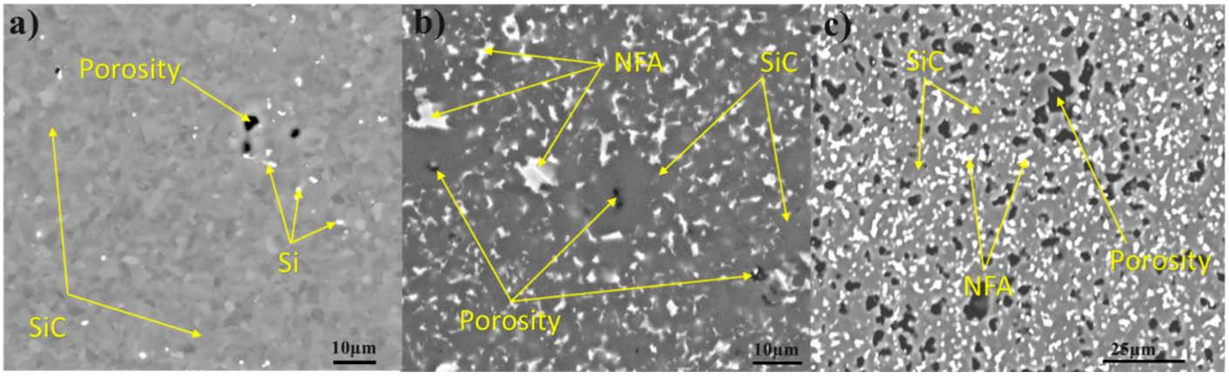

Fig. 12. Back scatter electron images of SiC – NFA doped samples (a) pure SiC, (b) SiC doped with 2.5 wt.% NFA, (c) SiC doped with 5 wt.% NFA.

Table 2. Quantification results calculated by means of digital image analysis.

| | **NFA (%)** | **Porosity (%)** |
|---|---|---|
| Sample 1 | 0.71 ± 0.23[a] | 0.16 ± 0.12 |

| | | |
|---|---|---|
| Sample 2 | 8.66 ± 1.41 | 0.18 ± 0.16 |
| Sample 3 | 17.32 ± 1.94 | 3.16 ± 1.06 |

a. Si content, no NFA.

### 4.3.2. Electron Back Scatter Diffraction

The results of the EBSD examination of the pure SiC sample are shown in Fig. 13. Equiaxed (Fig. 13a) grains with an average grain size of 2.46 ± 0.12 µm and random crystallographic distribution of both 4H and 6H SiC grains were identified with porosity fairly evenly distributed. The EBSD scan has been filtered to eliminate points with a CI value less than 0.1. These unindexed points include the NFA phases, porosity, and potentially a limited number of SiC grains with a low CI. Polishing of SiC for EBSD is notoriously difficult as reported previously [58], which could have been contributed towards SiC grains not identified.

The regions highlighted in black boxes in Figs. 14 and 15 show the unindexed regions corresponding to the NFA-based compound. The CI value corresponding to this phase was very low, so this phase has not been considered in the analysis of Sample 2 (Fig. 14) and Sample 3 (Fig. 15). From these results, it seems that the NFA additions pin the grain boundaries to prevent grain growth during the high-temperature SPS process. However, the grain sizes of the three samples (Fig. 16) should be evaluated in contents to the original powder grain sizes to determine if the original powder size of Samples 2 and 3 were not already smaller than those of the baseline SiC sample.

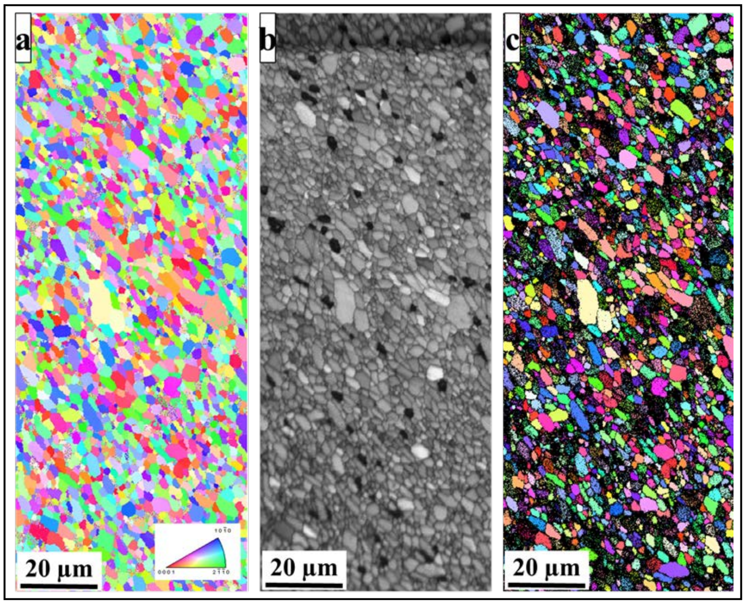

Fig. 13. (a) An inverse pole figure (IPF) map on pure SiC shows the distribution of near equiaxed grains with an average grain size of 2.46 ± 0.12 µm. (b) an image quality (IQ) map shows the distribution of grains and pores in the specific area of analysis. (c) The EBSD scan has been filtered to eliminate data points with CI value less than 0.1.

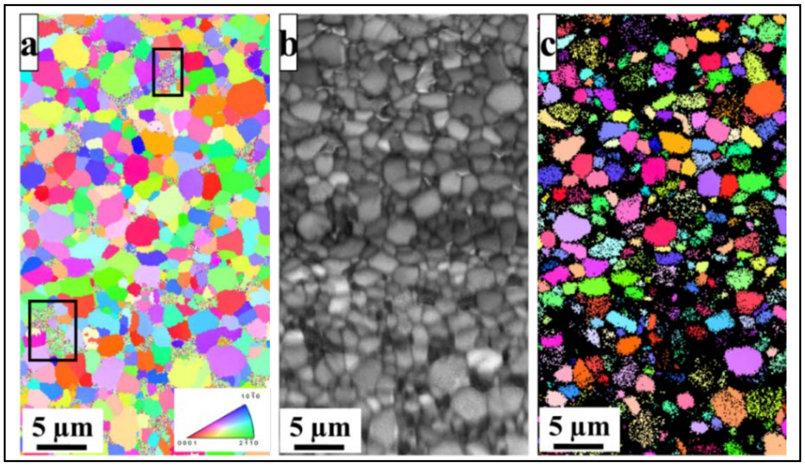

Fig. 14. (a) An inverse pole figure (IPF) map on Sample 2 shows the distribution of near equiaxed grains with an average grain size of 1.76 ± 0.08 µm. The regions highlighted in black boxes shows the unindexed regions corresponding to the NFA based compound; (b) an image quality (IQ) map

shows the distribution of grains and pores in the specific area of analysis. (c) The EBSD scan has been filtered to eliminate data points with CI value less than 0.1. The unindexed points include the porosity and NFA compound.

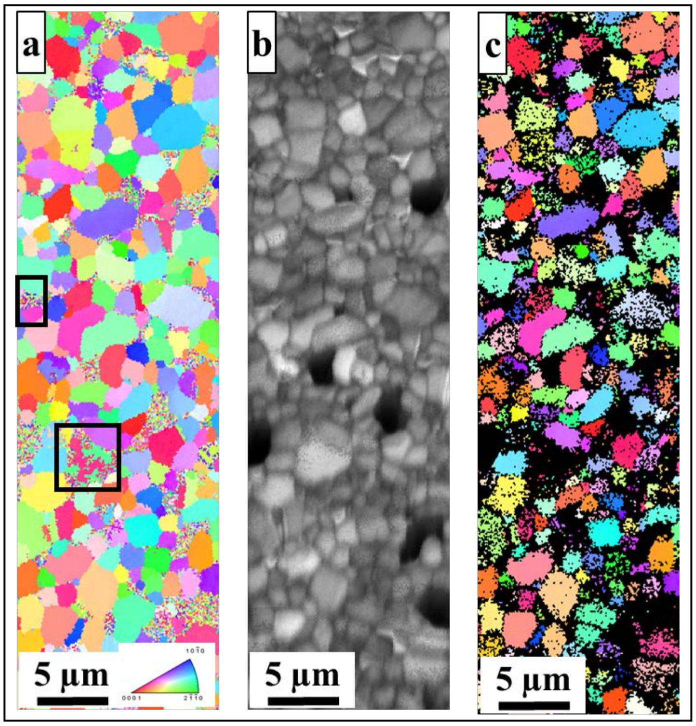

Fig. 15. (a) An inverse pole figure (IPF) map on Sample 3 shows the distribution of near equiaxed grains with an average grain size of 1.68 ± 0.06 µm. The regions highlighted in black boxes shows the unindexed regions corresponding to the NFA based compound; (b) an image quality (IQ) map shows the distribution of grains and pores in the specific area of analysis. (c) The EBSD scan has been filtered to eliminate data points with CI value less than 0.1. The unindexed points include the porosity and NFA compound.

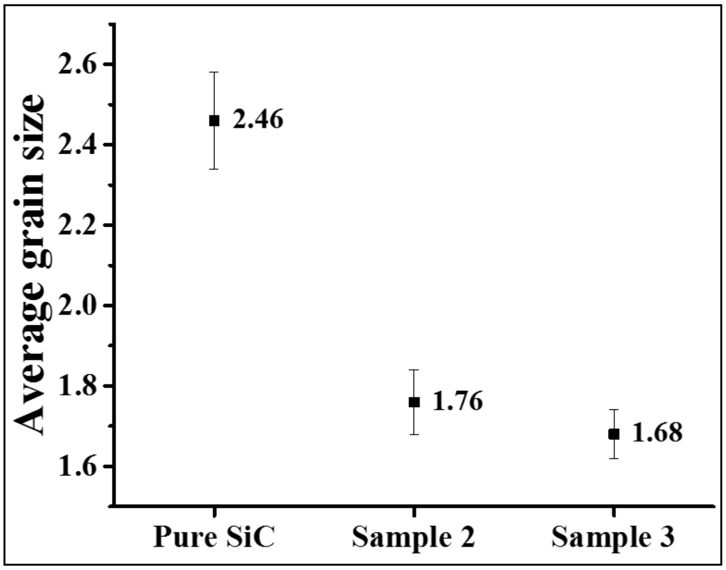

Fig. 16. A comparison of grain size variation in three SPS-fabricated SiC-based samples.

Pole figures (Fig. 17) prepared from the three samples show no significant differences when compared and shows a random crystallographic distribution of 6H and 4H-SiC grains. However, there is an indication of preferential orientation for the 4H-SiC in the pure SiC sample as shown in Fig. 17a.

The EBSD maps in Fig. 18 show the distribution of 6H-SiC (red) and 4H-SiC (green) grains for (a) the pure SiC sample ~6.6% 4H-SiC; (b) Sample 2 (97.5% SiC-2.5% NFA) with ~5.8% 4H-SiC; and (c) Sample 3 (95% SiC-5% NFA) ~10.3 % 4H-SiC. Fig. 19 the graphical comparison of the volume fraction of 4H-SiC between the three samples. From these results it is suggested that Sample 3 contains a higher fraction of 4H-SiC. However, the area of EBSD examination was smaller for Sample 3 compared with the other two samples, which should be taken into consideration.: (1) Pure SiC: 60.0 × 149.91 µm2, 2) Sample 2: 24.8 × 43.47 µm2, 3) Sample 3: 14.16 × 48.95 µm2. The smaller area was a result of the difficulty to obtain relevant surface smoothness for quality EBSD measurements.

Regardless the quantification accuracy, the fact that 4H was identified during this evaluation shows a phase transformation occurred during SPS fabrication. Further it seems that the quantity of 4H-SiC grains increased with increasing NFA content because of the increasing excess NFA sites. This is similarly to the work performed by Guo et al. 2015 [59] with $B_4C$ as the binder. Therefore, it is recommended that the NFA solubility limit for 6H-SiC be determined.

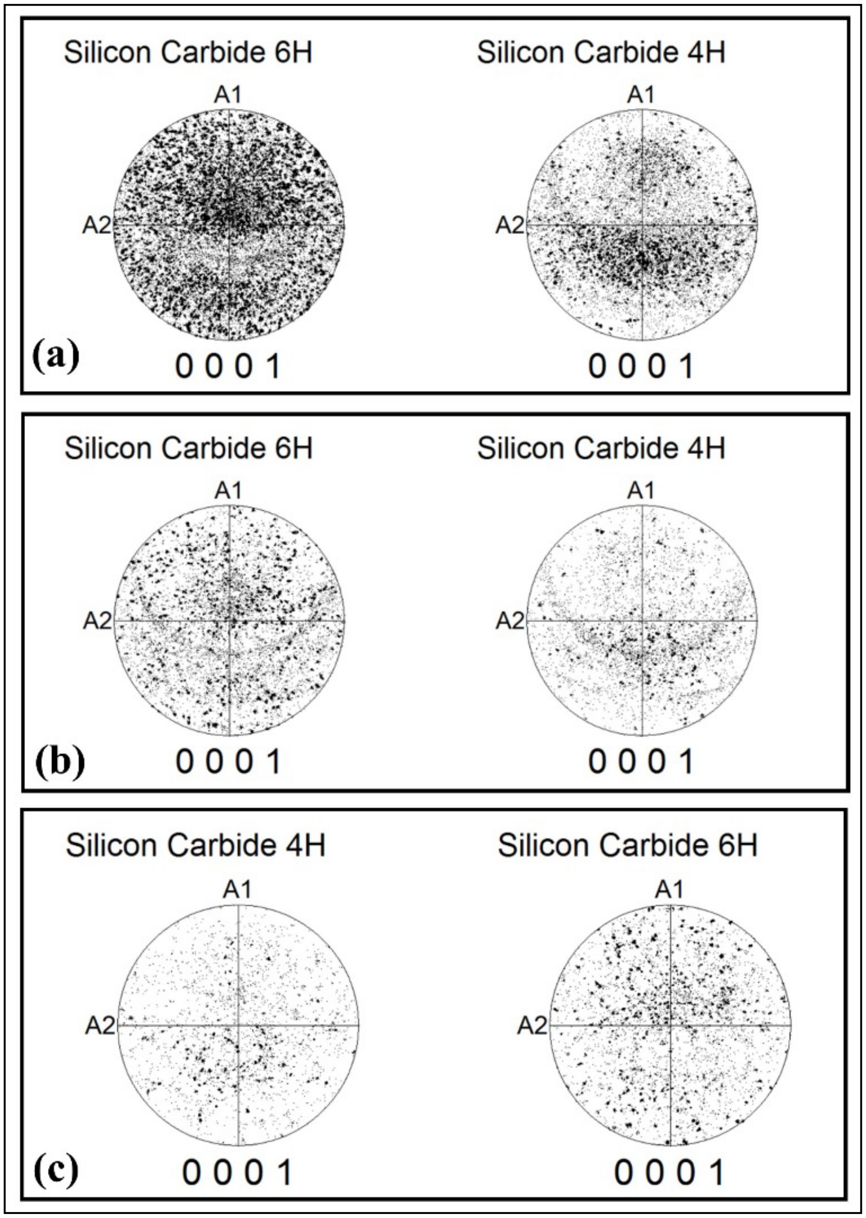

Fig. 17. Pole figures representing 4H and 6H SiC grains in the three samples.

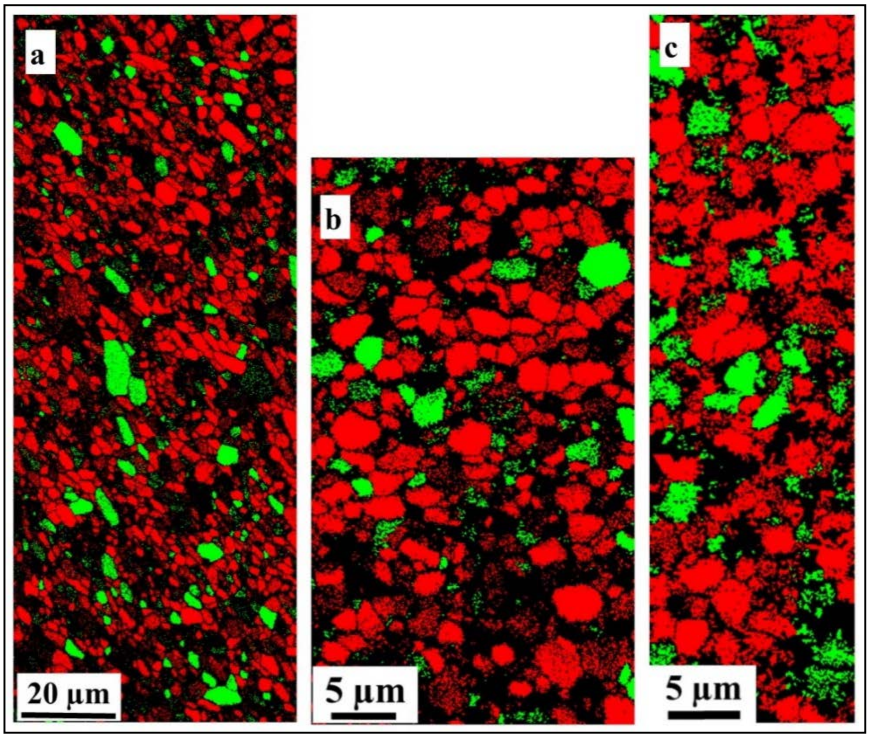

Fig. 18. These EBSD maps show the distribution of 6H-SiC (red) and 4H-SiC (green) grains for (a) the pure SiC sample ~6.6% 4H-SiC; (b) Sample 2 (97.5% SiC-2.5% NFA) with ~5.8% 4H-SiC; and (c) Sample 3 (95% SiC-5% NFA) ~10.3 % 4H-SiC.

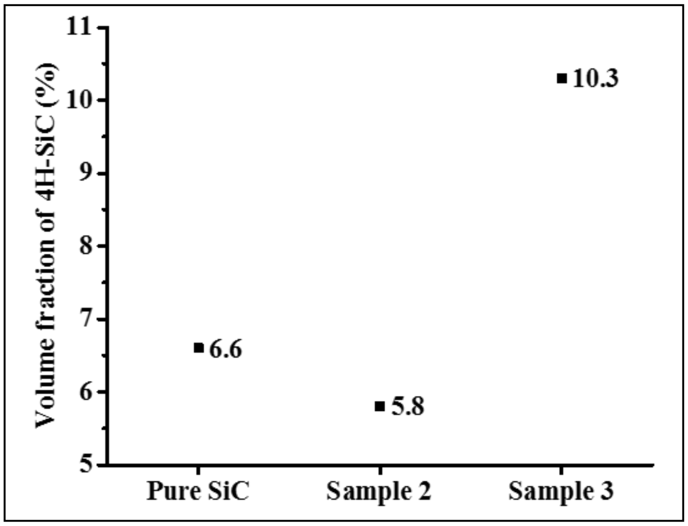

Fig. 19. A comparison of variation in volume fraction of 4H-SiC in three SPS-fabricated SiC-based samples.

### 4.3.3. Nanohardness

The nanohardness of the 25 vol% $Cr_3C_2$@SiC-75 vol% NFA material before and after the ion irradiation is shown in Fig. 20. For the NFA matrix before the ion irradiation, the nanohardness increases slightly from 9.1±2.2 GPa at ~432 nm depth to 10.5±3.9 GPa at depth ~971 nm. The hardness of the NFA matrix after the ion irradiation has the same slightly increasing trend as that before the irradiation, rising from 7.6±2.0 GPa at ~478 nm to 8.8±3.3GPa at ~832 nm. In comparison, the NFA matrix shows reduced hardness after the ion irradiation.

The nanohardness of the reaction region before and after the ion irradiation in the 25 vol% $Cr_3C_2$@SiC-75 vol% NFA sample shows a slightly different trend as shown in Fig. 20. The nanohardness before the ion irradiation keeps decreasing from 6.9±1.5 GPa at ~500 nm to 6.3±1.6 GPa at ~973 nm. The nanohardness after the ion irradiation is mostly constant at ~5.4 GPa. The ion irradiation reduces the hardness of the reaction region by >15%. In our previous work, it has been shown that the main phase in the reaction region is graphite, which is relatively soft compared to the NFA steel. Thus, the hardness of the reaction region should be lower than that of the NFA matrix.

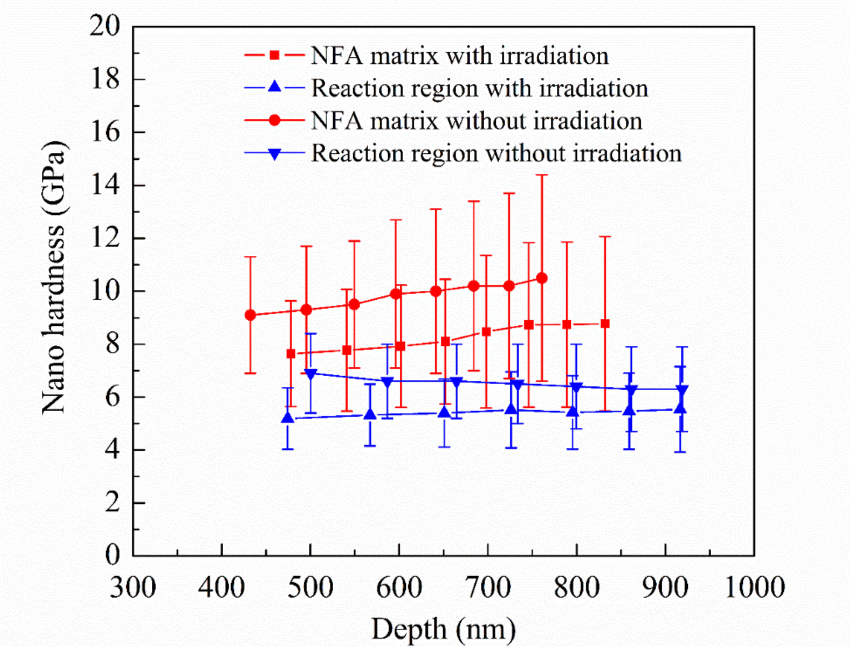

Fig. 20. Nano hardness of the 25 vol% $Cr_3C_2$@SiC-75 vol% NFA material before and after ion irradiation.

The reduced hardness in the NFA matrix and the reaction region is probably because the ion irradiation induces point defects, which diffuse into the original dislocation loops. If part of the dislocation loops is healed during the ion irradiation, it will further compromise the hardness of the material after the ion irradiation. As a new composite material, the $Cr_3C_2$@SiC-NFA still needs to be improved in this regard.

### 4.3.4. Atom probe tomography

Chemical and microstructural analyses from the two SiC-NFA composite samples (Sample 2: 97.5%SiC-2.5% NFA and Sample 3: 95% SiC-5% NFA) were performed using APT. The objective for the APT analysis is to focus the APT tip preparation on the interface between the SiC matrix and the NFA phase. Interface, matrix, and NFA phase compositional information was obtained from these tips.

APT specimens from SiC samples were prepared by standard lift-out and milling procedures using a FEI Quanta 3D SEM and focused ion beam (FIB) instrument (an example of the tips prepared are shown in Fig. 21). Data acquisition was performed using a CAMECA LEAP 4000X HR instrument operated in the laser mode with 80 pJ/pulse energy, a pulse repetition rate of 200 kHz, and data collection rate of 5 atoms per 1000 pulses. The specimens in local electrode atom probe (LEAP) were cooled to a base temperature of 55 K. Data analysis was completed with the CAMECA Integrated Visualization and Analysis Software (IVAS) Version 3.6.8. The datasets were reconstructed using radius determined from SEM image. The reconstruction parameters ranged between an image compression factor from 1.4 to 1.5 and k value from 3.1 to 3.5.

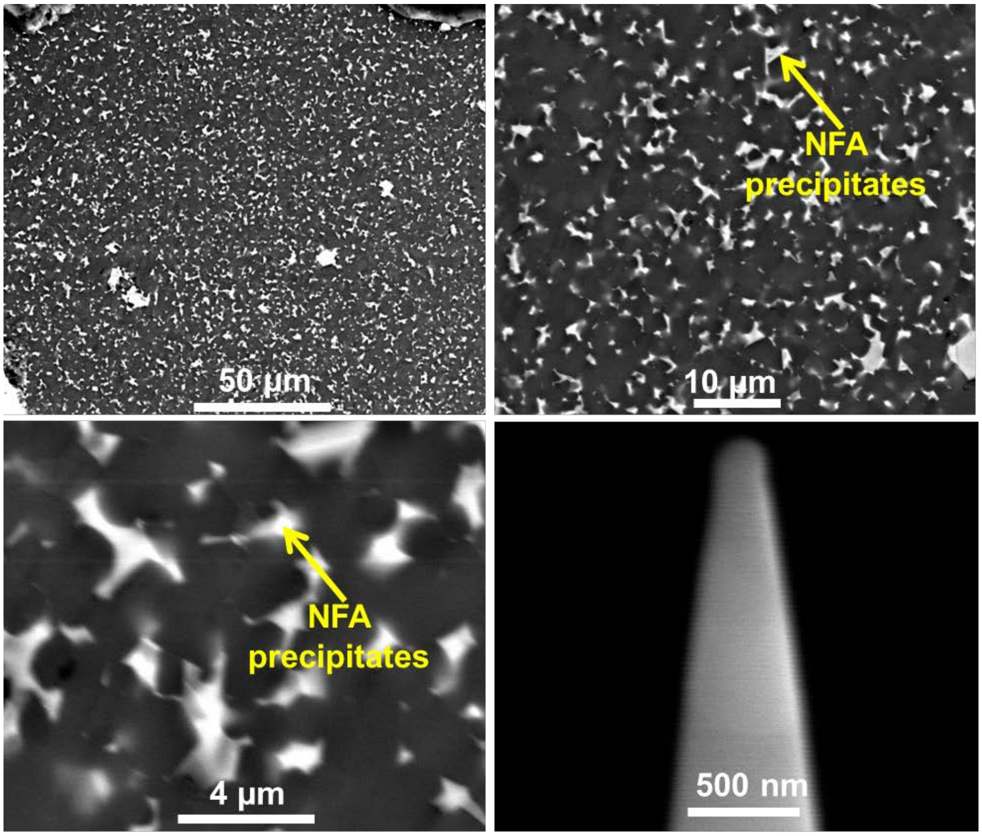

Fig. 21. An example of an APT tip from the SiC matrix from Sample 2.

Tips from Sample 2 containing the matrix and the NFA phase were made, and no interface was found to be present.

The mass spectrum obtained from SiC is shown in Fig. 22. The mass spectrum shows peaks appearing from $C^{1+,2+}$, $C_2^{1+}$, $C_4^{1+}$, $C_3^{1+,2+}$, and $Si^{1+,2+,3+}$ (predominantly $Si^{2+}$). The 3D distribution of Si and C is shown in Fig. 23 along with impurities of Cr and Al. All the species are uniformly distributed in the analyzed volume. The measured composition for SiC sample is shown in Table 3. The observed deficiency in measured C composition could be attributed to an artifact of APT for measuring composition from alloy that contains elements that differ significantly in their evaporation. The calculated evaporation fields for $Si^{1+}$, $Si^{2+}$, and $Si^{3+}$ are 45, 33, and 60 V/nm, respectively, and those of $C^{+}$, $C^{2+}$, and $C^{3+}$ are 142, 103, and 155 V/nm, respectively [60]. These values indicate that silicon is substantially easier to evaporate than carbon. It is likely that the silicon preferentially evaporates during laser-assisted evaporation leaving the surface of the specimen rich in carbon. Preferential field evaporation of one element is common in alloys that contain elements that differ significantly in their evaporation [61]. This could lead to observed low measurement of C content in carbides system [62].

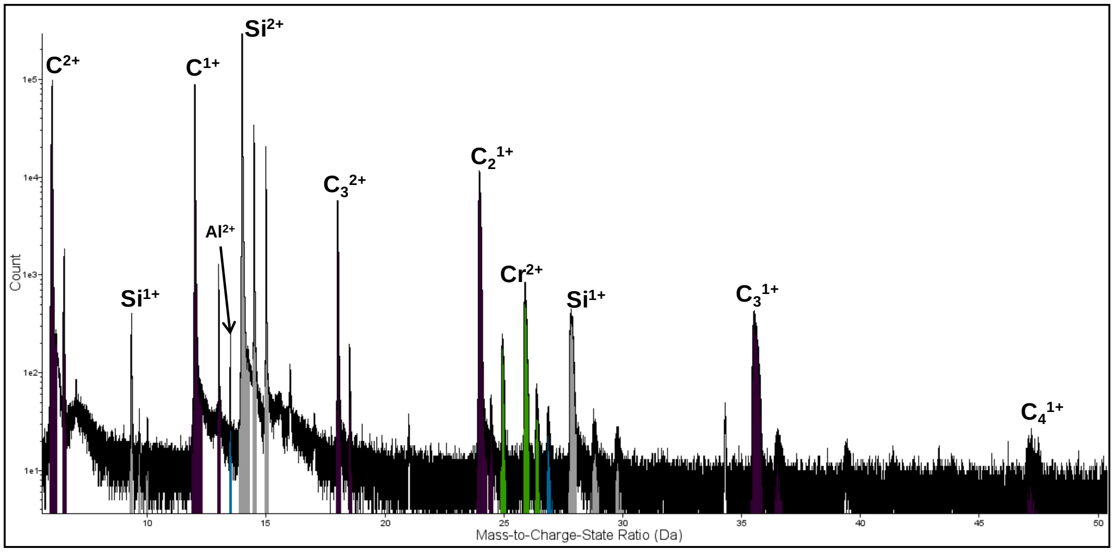

Fig. 22. Mass spectrum from SiC region.

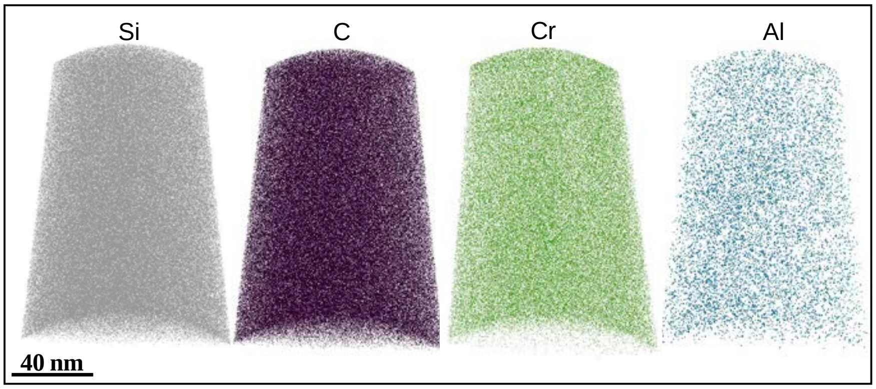

Fig. 23. 3D distribution of C, Si, Cr, and Al in the SiC matrix of Sample 2.

Table 3. Measured composition from SiC region.

| Elements | At.% |
|---|---|
| Si | 57.0 |
| C | 42.5 |
| Cr | 0.45 |
| Al | 0.03 |

The mass spectra obtained from the NFA region are shown in Fig. 24. The mass spectrum shows peaks appearing from ions such as $Fe^{1+,2+}$, (predominantly $Fe^{2+}$) $Si^{1+,2+,3+}$ (predominantly $Si^{2+}$) along with Cr, Al, Ti, V, and Mn. The 3D distribution of the elements is shown in Fig. 25.

The measured composition for the NFA precipitate is shown in Table 4. In this case, the specimen for APT was completely prepared inside the precipitate. The precipitate shows uniform distribution of impurities of Cr, Al, Ti, V, Mn, and P inside of the precipitate.

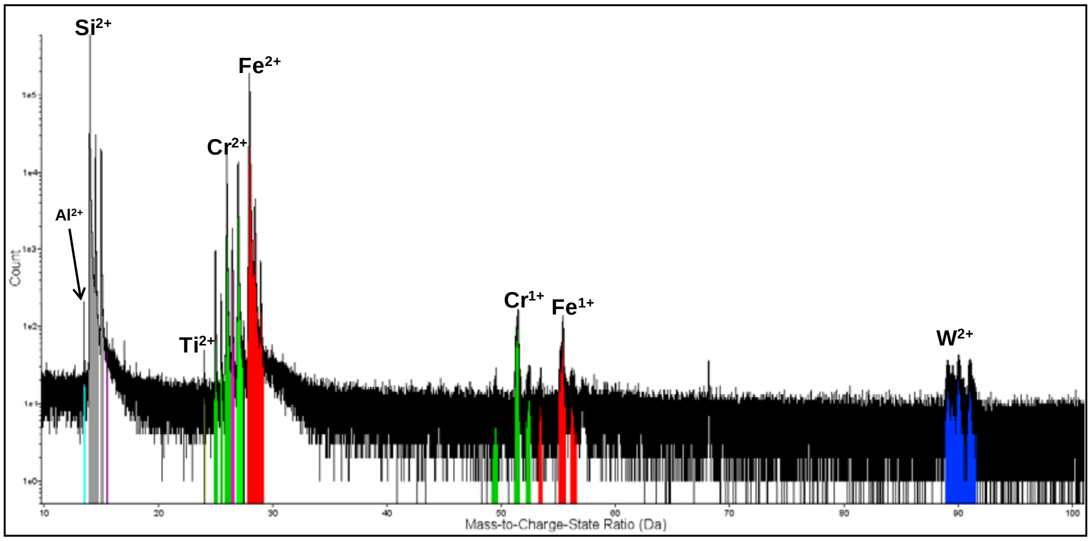

Fig. 24. Mass spectrum from the NFA region of Sample 2 (97.5% SiC-2.5% NFA).

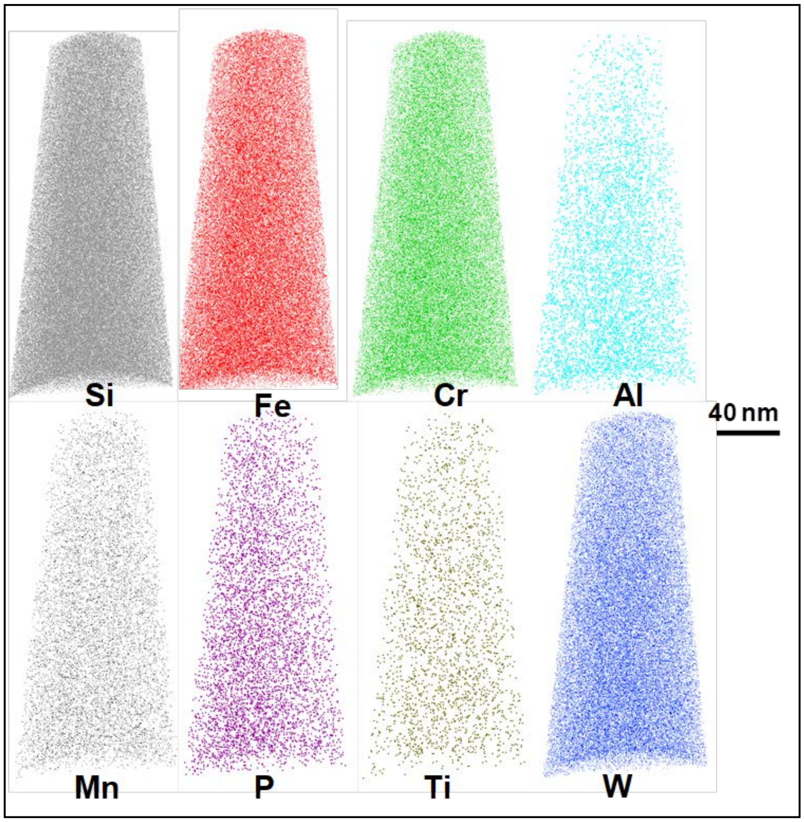

Fig. 25. 3D distribution of Si, Fe, Cr, Al, Mn, P, Ti, and W from the NFA phase from Sample 2 (97.5% SiC-2.5% NFA).

Table 4. Measured composition from the NFA phase from Sample 2 (97.5% SiC-2.5% NFA).

| Elements | At.% |
|---|---|
| Si | 49.3 |
| Fe | 46.8 |
| Cr | 3.5 |
| V | 0.34 |
| W | 0.09 |
| Al | 0.01 |
| Mn | 0.01 |
| Ti | 0.01 |
| P | 0.01 |

The APT specimen for Sample 3 was prepared at the interface of the NFA phase and the SiC matrix. Fig. 26 shows the locations where the APT tips were removed from Sample 3. The 3D distribution of Si and C is shown in Fig. 27.

Fig. 27b and Fig. 27c show high the iso-concentration map of C and Si representing the SiC phase, whereas Fig. 27h shows a high iso-concentration map for Fe representing the FeSi phase. Apart from Si and C, SiC phases show presence of impurities such as Ti, W, and P as shown in Figs. 27d, f, and k, respectively. In the FeSi phase, there is additional presence of minor elements such as Ti, Al W, Cr, and Mn as shown in Fig. 27d, e, f, i, and j, respectively.

The measured composition for the NFA phase is shown in Table 2 and those of the SiC matrix adjacent to the interface are shown in Table 5. It is noted that the SiC matrix here also contains Fe in contrast with the SiC matrix of Sample 2, which was prepared not as close from the interface itself. It is at this point unclear if the Fe is also present further away from the interface in the SiC matrix material. The composition for NFA phase has been measured by placing a cube of the size 40 nm × 40 × 40 nm inside the precipitate. The precipitate also shows impurities of Cr, Mn, Ti, and P distributed inside the NFA phase. Interestingly, Al, Mn, Ti, Cr, and W appear to be segregated at the interface between the matrix of SiC and the NFA phase.

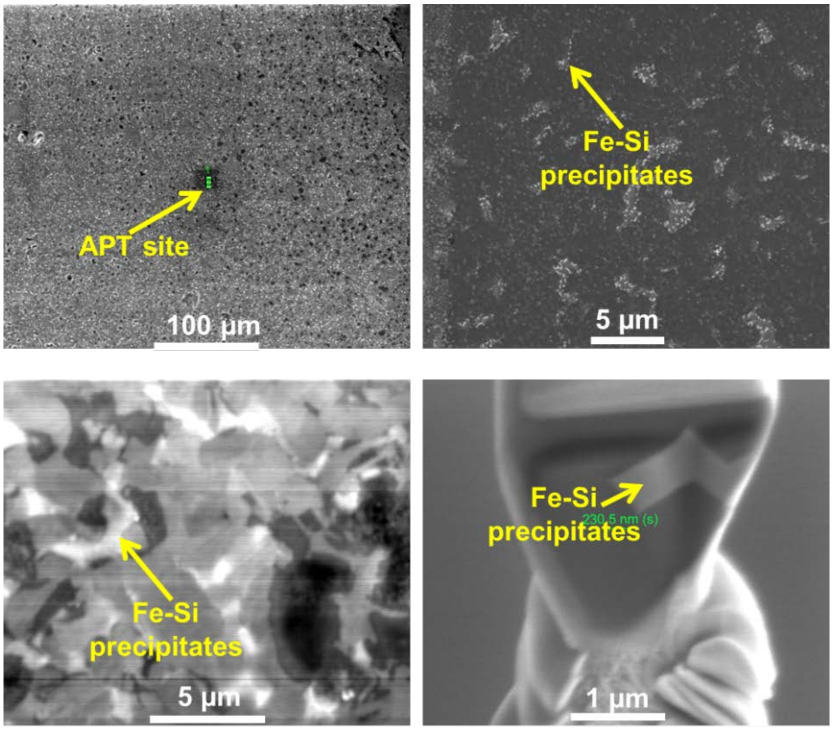

Fig. 26. Location of the APT tip preparation in Sample 3.

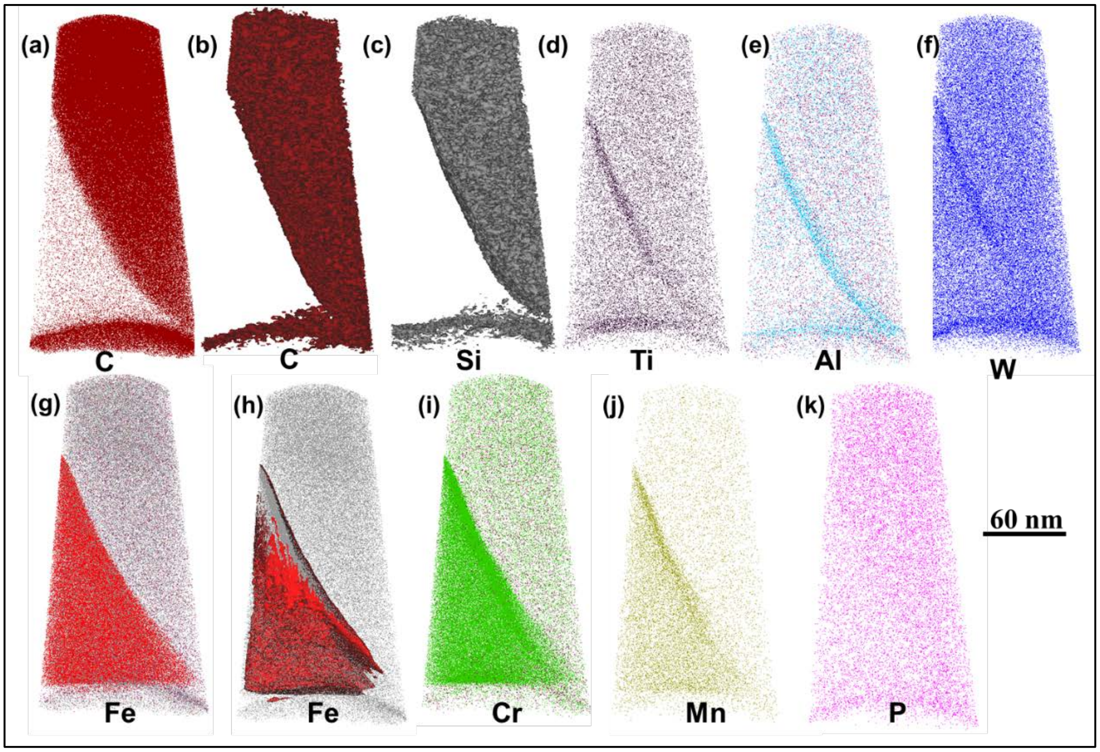

Fig. 27. 3D distribution of C, Si, Fe, Cr, Al, Mn, P, Ti, and W from the APT tip produced at the SiC-NFA interface from Sample 39 (5%SiC-5%NFA).

Table 5. Measured composition from the precipitate from Sample 3 (95% SiC-5% NFA).

| **Elements** | **At.%** |
|---|---|
| Si | 50.0 |
| Fe | 45.2 |
| Cr | 4.3 |
| V | 0.32 |
| W | 0.05 |
| Al | 0.01 |
| Mn | 0.04 |
| Ti | 0.14 |
| P | 0.01 |

The APT technique is successfully applied in determining the chemistry from the NFA phase embedded in the SiC matrix. The measured stoichiometry for Sample 2 (97.5%SiC–2.5%NFA) and Sample 3 (95%SiC–5%NFA) from the precipitate show a stoichiometry of (Fe,Cr):Si~1. Uniform distribution of impurities of Cr, Al, Ti, V, Mn, and P is found inside the precipitate of Sample 2. For the Sample 3 (95%SiC-5%NFA), Al, Mn, Ti, and W appear to be segregated at the interface of precipitate and SiC matrix.

Table 6. Measured composition from the SiC matrix from Sample 3 (95% SiC-5% NFA).

| **Elements** | **At.%** |
|---|---|
| Si | 57.75 |
| C | 40.63 |
| Fe | 0.84 |
| Cr | 0.68 |
| Au | 0.05 |
| Ni | 0.02 |
| Al | 0.02 |

## 4.4. $Y_2O_3$ coating on SiC

Fig. 28 shows the XRD patterns of the pure SiC powder, $Y_2O_3$@SiC powder, $Y_2O_3$@SiC+NFA powder mixture, and 1150°C sintered $Y_2O_3$@SiC-NFA composite. The XRD pattern of the $Y_2O_3$@SiC powder clearly shows $Y_2O_3$ peaks along with SiC peaks. Additional small intensity peaks of $Y_2O_3 \cdot SiO_2$ can also be observed. This means a small amount of $Y_2O_3 \cdot SiO_2$ has formed at the interface between the $Y_2O_3$ coating and SiC powder after the molten salt coating process. The XRD pattern of the 1150°C sintered $Y_2O_3$@SiC-NFA composite clearly shows low intensity SiC and $Y_2O_3$ peaks in addition to the NFA peaks. The XRD pattern is very similar to that of the $Y_2O_3$@SiC+NFA powder mixture except for some slight phase shift in the NFA (α-Fe) peaks. This means that the $Y_2O_3$ coating has been successful in suppression of detrimental iron silicide phases while also retaining SiC particles in the composites. The small amount of phase shift in NFA peaks indicates marginal dissolution of SiC has occurred during sintering.

Fig. 29 shows the surface morphology of the SiC particles before and after the molten salt coating process. The SiC powder without the coating clearly shows very clean faceted morphology (Fig. 29a). However, the surface morphology of the $Y_2O_3$@SiC powder indicates presence of homogeneous and dense $Y_2O_3$ coating on SiC particle. This means heterogeneous nucleation of $Y_2O_3$ on SiC particle in the molten salt at high temperature has been successful in preparing core-shell type $Y_2O_3$ coated SiC particles.

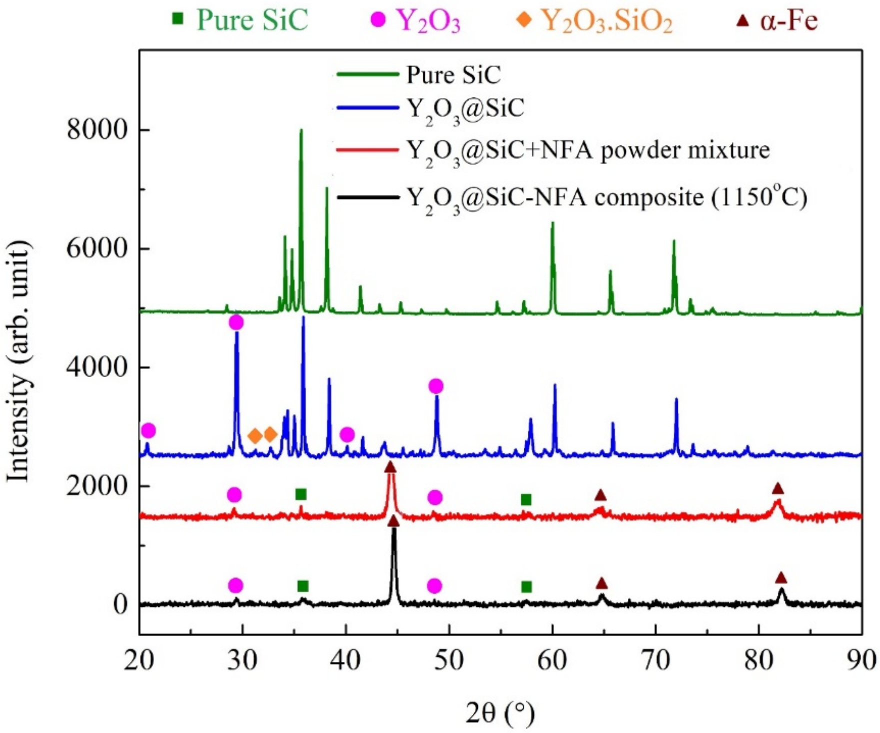

Fig. 28. XRD patterns of pure SiC powder, $Y_2O_3$@SiC powder, $Y_2O_3$@SiC+NFA powder mixture, and 1150°C sintered $Y_2O_3$@SiC-NFA composite.

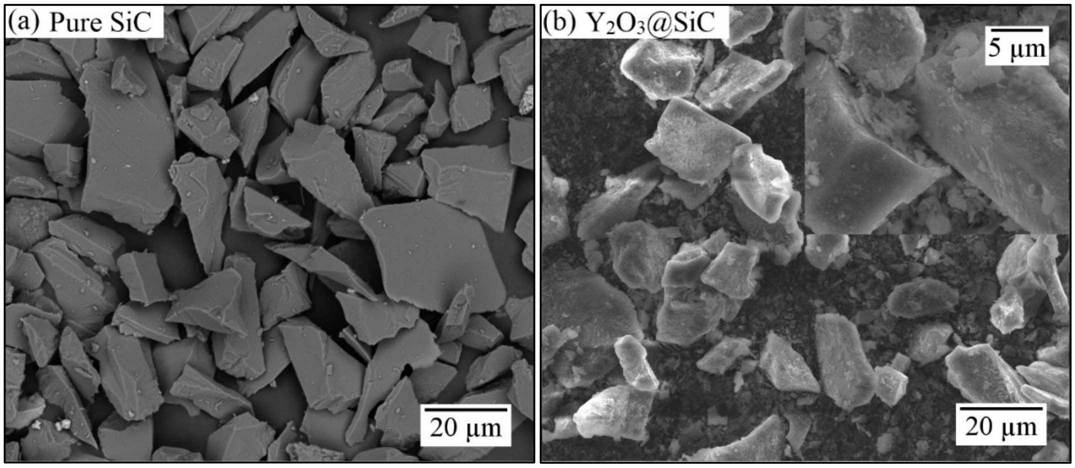

Fig. 29. Surface morphology of SiC particles (a) pure SiC, (b) with $Y_2O_3$ coating (magnified image in the corner.

### 4.5. Microstructural evolution during spark plasma sintering

Fig. 30 shows the SEM micrographs of the spark plasma sintered NFA and 25 vol% $Cr_3C_2$@SiC-NFA samples. The NFA sample shows mainly equiaxed grains along with some pores at the grain boundaries but there are no visible secondary phases as indicated in Fig. 30a. The microstructure of the 25 vol% $Cr_3C_2$@SiC-NFA sample shows fine light gray precipitates (P1) in a dark gray matrix as shown in Fig. 30b. The precipitates (P1) form interconnected structures possibly due to a large volume fraction and coalescence of adjacent growing precipitates during the spark plasma sintering process. Very fine and bright precipitates (P2) can also be seen throughout the microstructure (Fig. 30b). The P1 and P2 precipitates are identified using TEM diffraction pattern and STEM-EDS methods as $M_7C_3$ and MC type carbides (Figs. 34 and 35), and will be discussed in detail later. The dark phase in Fig. 31b is graphite precipitates as identified in our previous work [32]. All these precipitates, P1, P2, and graphite, are a result of reactions between the NFA and $Cr_3C_2$@SiC particles during the spark plasma sintering, as to be discussed later.

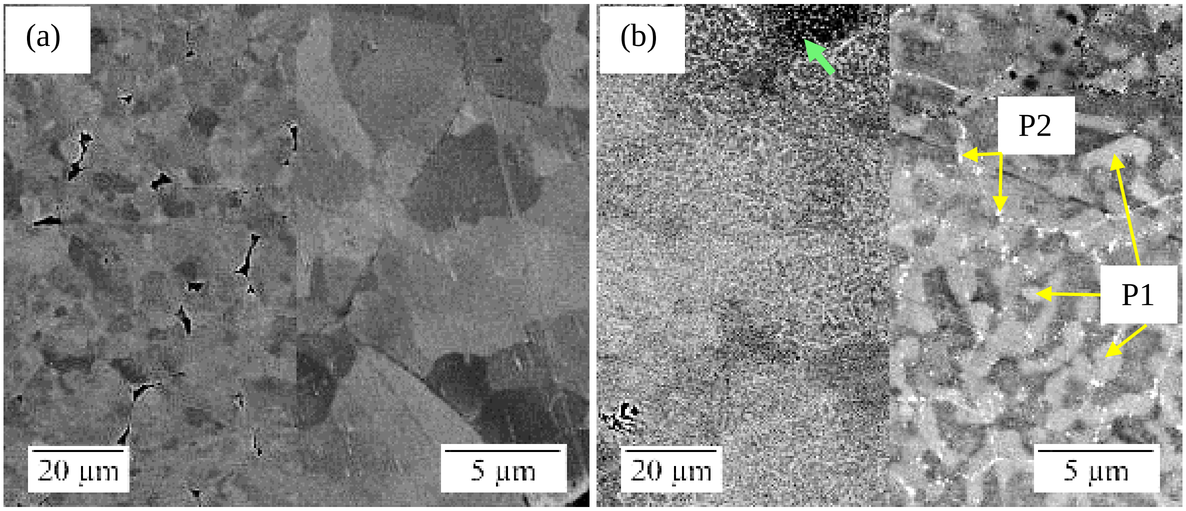

Fig. 30. SEM micrographs of (a) NFA and (b) 25 vol% $Cr_3C_2$@SiC-NFA composite after the SPS sintering (the right side is the magnified image of the left side for each sample).

Figs. 31a shows the EBSD IPF map of the SPS sintered NFA specimen. The grain size is on average 15 μm but the microstructure has a mixture of very large grains (~45 μm) and plenty of small grains (4-5 μm). Such a bimodal grain size distribution has been previously observed in various SPS sintered ODS alloys [63-65]. The behavior is attributed to variations in dislocation density and inhomogeneous distribution of Y-Ti-O nanoclusters, which create inhomogeneous grain boundary pinning effects and also local variations in heat distribution due to the joule heating effect during the SPS process. The IPF map in Fig. 31a shows no preferential grain orientation and almost fully recrystallized grains with no remnants of previously consolidated microstructures of the starting powders. Figs. 31b and 31c show the IPF maps of α-ferrite and $M_7C_3$ grains of the 25 vol% $Cr_3C_2$@SiC-NFA composite respectively. Fig. 31b shows that there is no preferential grain orientation for the α-ferrite grains. The size of the α-ferrite grains is much smaller (~3 μm) compared to that of the NFA sample (~15 μm). The overall smaller size grains in the 25 vol% $Cr_3C_2$@SiC-NFA composite can be attributed to the strong pinning effects due to the significant precipitation of the P1 and P2 phases as a result of the reactions between NFA and $Cr_3C_2$@SiC during the spark plasma sintering. Fig. 31c shows that the interconnected worm-like structure of the $M_7C_3$ (or P1) precipitates consists of small (1-1.5 μm) sized equiaxed grains with no preferential orientation. Fig. 31d shows the EBSD phase map of the 25 vol% $Cr_3C_2$@SiC-NFA composite with the α-ferrite and $M_7C_3$ phases. The shape and size of the phases correspond well with the SEM image in Fig. 30b.

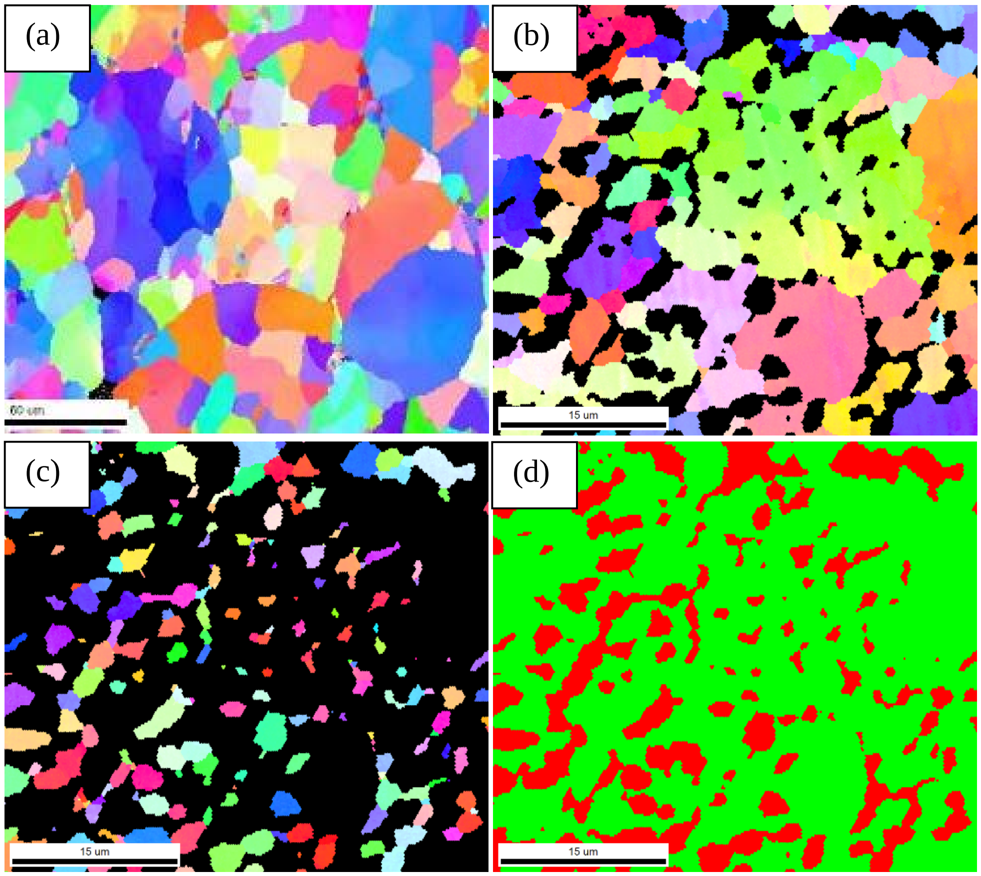

Fig. 31. (a) IPF map of the NFA sample; IPF maps of (b) α-ferrite grains and (c) $M_7C_3$ grains, and (d) phase map of the 25 vol% $Cr_3C_2$@NFA-SiC composite after the SPS sintering.

## 4.6. Effect of thermal treatment on microstructures

Fig. 32 shows the microstructures of the NFA and 25 vol% $Cr_3C_2$@SiC-NFA composite after the thermal treatment at 1000°C for 50 hours. The NFA sample (Fig. 32a) shows equiaxed grains similar to the microstructures observed before the thermal treatment. The 25 vol% $Cr_3C_2$@SiC-NFA composite after the treatment (Fig. 32b) shows dark gray NFA grains, light gray P1 precipitate, and fine bright P2 precipitate similar to that before the thermal treatment (Fig. 30b). Fig. 33 shows the size and volume fraction of the precipitates (P1, P2) before and after the 1000°C treatment. The sizes of the P1 and P2 precipitates show 160% and 104% increases, respectively, after the thermal treatment at 1000°C. The volume fractions of the P1 and P2 precipitates show 37.5% and 75% increases respectively. Therefore, the thermal treatment at 1000°C has resulted in coarsening and potentially more nucleation of the existing precipitates (P1 and P2).

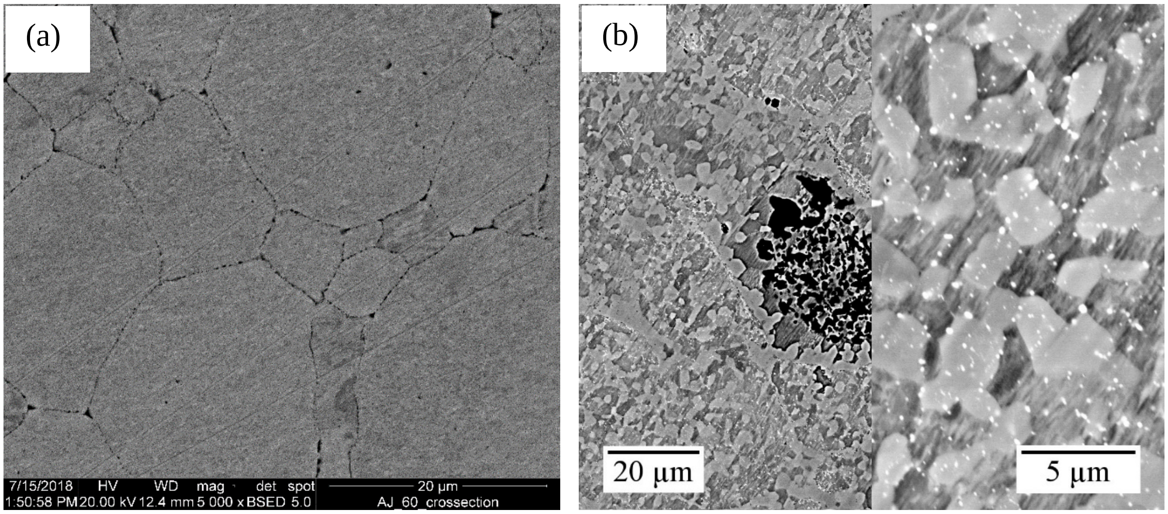

Fig. 32. SEM micrographs of (a) NFA and (b) 25 vol% $Cr_3C_2$@SiC-NFA composite after the thermal treatment at 1000°C for 50 hours (right part is magnified image of left part).

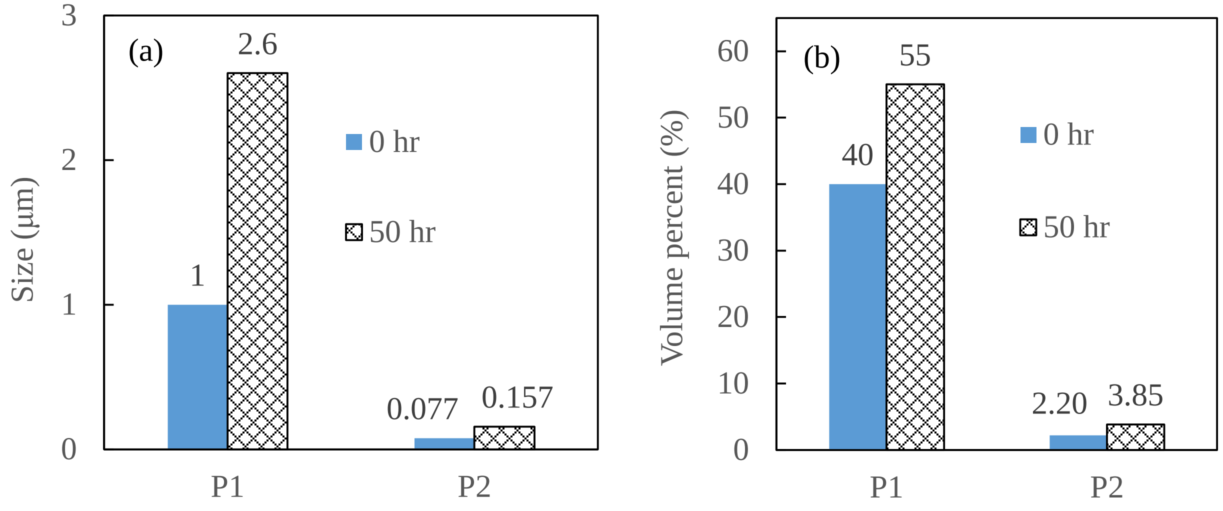

Fig. 33. (a) Size of P1 and P2 precipitates (b) volume fraction of P1 and P2 precipitates, before and after the 1000°C thermal treatment for 50 hours.

Fig. 34 shows the STEM bright field images of the 25 vol% $Cr_3C_2$@SiC-NFA composite after the thermal treatment at 1000°C for 50 hours. The bright region in Fig. 34 is Fe-rich. This phase is similar to the dark grey NFA grains in the corresponding SEM images (Figs. 30b and 32b). The dark region in Fig. 34 can be correlated with the P1 precipitate in the SEM images in Figs. 30b and 32b. The diffraction patterns corresponding to the bright region (NFA) and dark region (P1) in Fig. 34 are shown in Figs. 35a and 35b respectively. The patterns are indexed by comparing with the simulated patterns from CrysTBox and CrystalMaker™ software. The NFA region has been indexed as α-ferrite (BCC). The P1 phase is identified as $M_7C_3$ phase, which is consistent with the EBSD results from Fig. 31c. The EDS mappings in Fig. 34a show that the $M_7C_3$ phase is rich in both Fe and Cr. Therefore, the composition of the P1 precipitates should be $(Fe,Cr)_7C_3$. Some fine precipitates can be observed in both the bright and dark regions as shown in Figs. 34a and 34b. This phase is the bright fine precipitates (P2) observed in Figs. 30b and 32b. The EDS analysis shows Ti and W enrichment in these precipitates. The W enrichment explains the bright contrast in the SEM images (Figs. 30b and 32b). These precipitates are likely to be (Ti,W)C, i.e. MC type carbides [66]. It should be mentioned that the presence of $M_7C_3$ and MC carbide phases have been previously reported for various ODS and ferritic alloys.

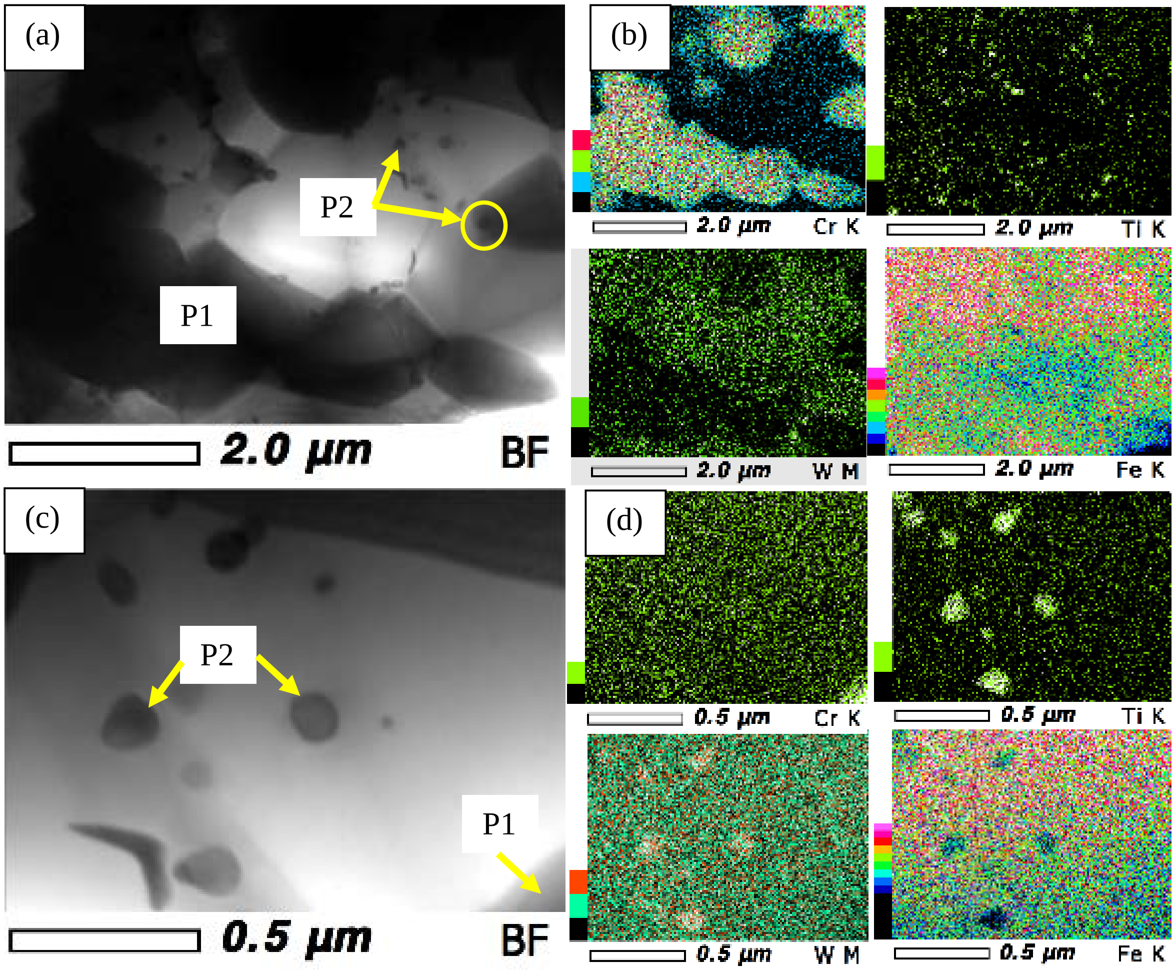

Fig. 34. STEM-BF images (a, c) with corresponding EDS mappings (b, d) for the $Cr_3C_2$@SiC-NFA composite after the 1000°C treatment for 50 hours.

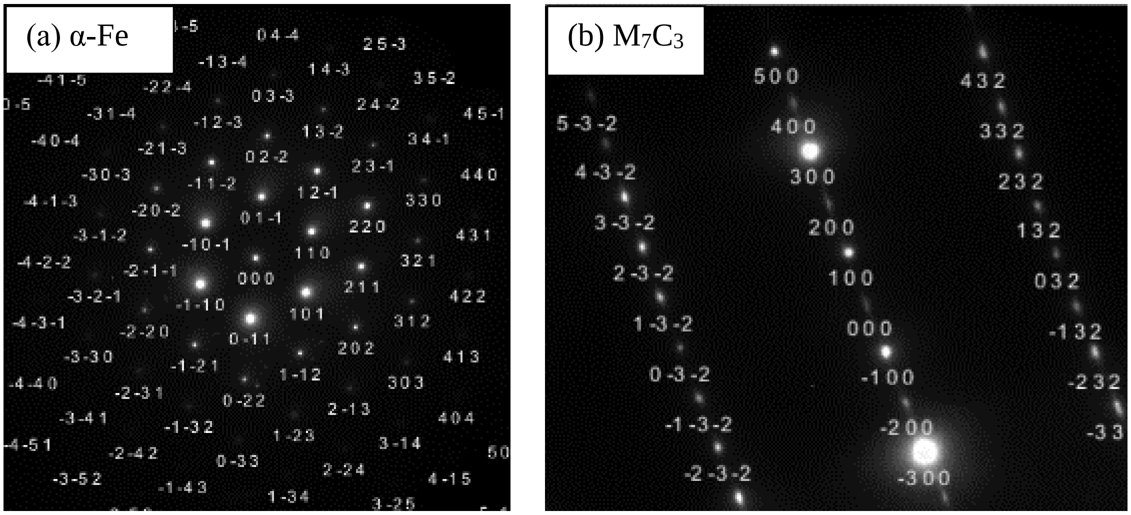

Fig. 35. (a) Diffraction patterns from the bright area, (b) diffraction pattern from the dark area (P1) in Fig. 34a.

Fig. 36b shows that the spark plasma sintering process has resulted in complete dissolution of the $Cr_3C_2$@SiC powder and formation of new phases such as $(Fe,Cr)_7C_3$, (Ti,W)C, and graphite. The reactions between SiC and NFA after the coating dissolution can be divided into two steps. The first step is dissociation of SiC into Si and C, according to Eq. (2). The dissociated Si and C atoms diffuse into NFA, thus forming Si and C containing supersaturated NFA. This supersaturated NFA then leads to the precipitation of graphite, $M_7C_3$, and MC phases as shown in Fig. 36b.

$$SiC \rightarrow Si_{NFA} + C_{NFA} \tag{2}$$

Dissolution kinetics of SiC has been studied using the DICTRA® software package as shown in Fig. 38. Within only 400 seconds around 20 μm thick SiC region is estimated to have dissolved in NFA at 950°C. This is caused by the high Si and C diffusion rates in the NFA matrix. Since the original SiC particle size was around 1-2 μm, it is likely that all the SiC particles were dissolved in the NFA matrix. Due to the very high diffusion rates of both Si and C in the NFA matrix at high temperatures, it can be assumed that supersaturated NFA formed in Eq. (2) has homogeneous Si and C compositions.

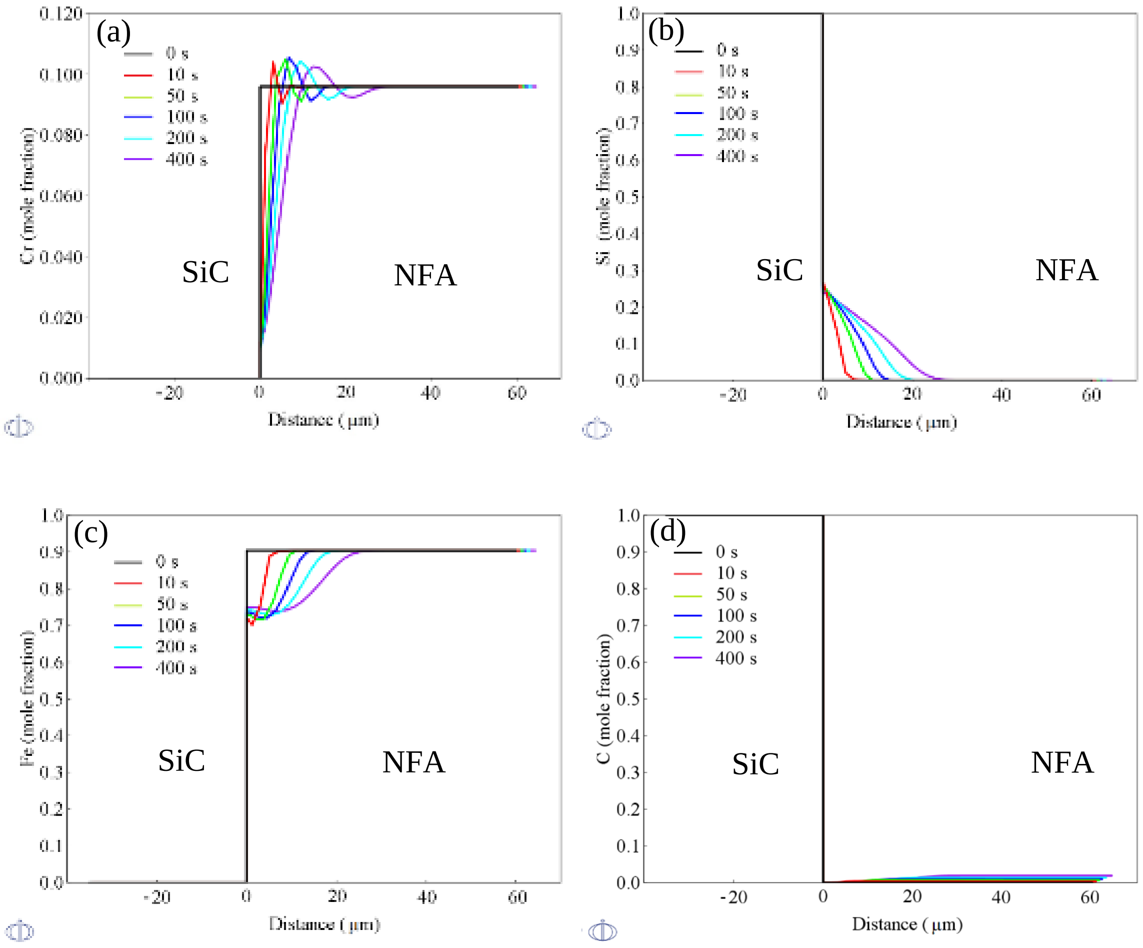

Fig. 36. Dissolution kinetics of SiC in the NFA matrix showing (a) Cr, (b) Si, (c) Fe, and (d) C diffusion behaviors using ThermoCalc-DICTRA simulations.

The second step involves formation of equilibrium phases from the newly homogenized composition. This leads to the precipitation of graphite, $M_7C_3$, and MC phases according to the reaction in Eq. (3). The phase diagram of the $Cr_3C_2$@SiC-NFA composite in Fig. 37 confirms the formation of these phases. The precipitation of the secondary phases from the supersaturated NFA can be visualized using the phase diagram in Fig. 37 and TTT diagram in Fig. 38. It shows the presence of NFA (α-ferrite), graphite, and $M_7C_3$ and MC carbides. The phase diagram was constructed using the ThermoCalc console mode, where the $Cr_3C_2$@SiC content in the NFA was varied rather than only varying a single element. The TTT diagram in Fig. 38a shows that all the precipitates form instantaneously at 950°C (during the sintering) as well as during the thermal treatment at 1000°C.

$$NFA\ (supersaturated\ with\ Si\ and\ C) \rightarrow NFA\ (Si) + M_7C_3 + MC + Graphite \qquad (3)$$

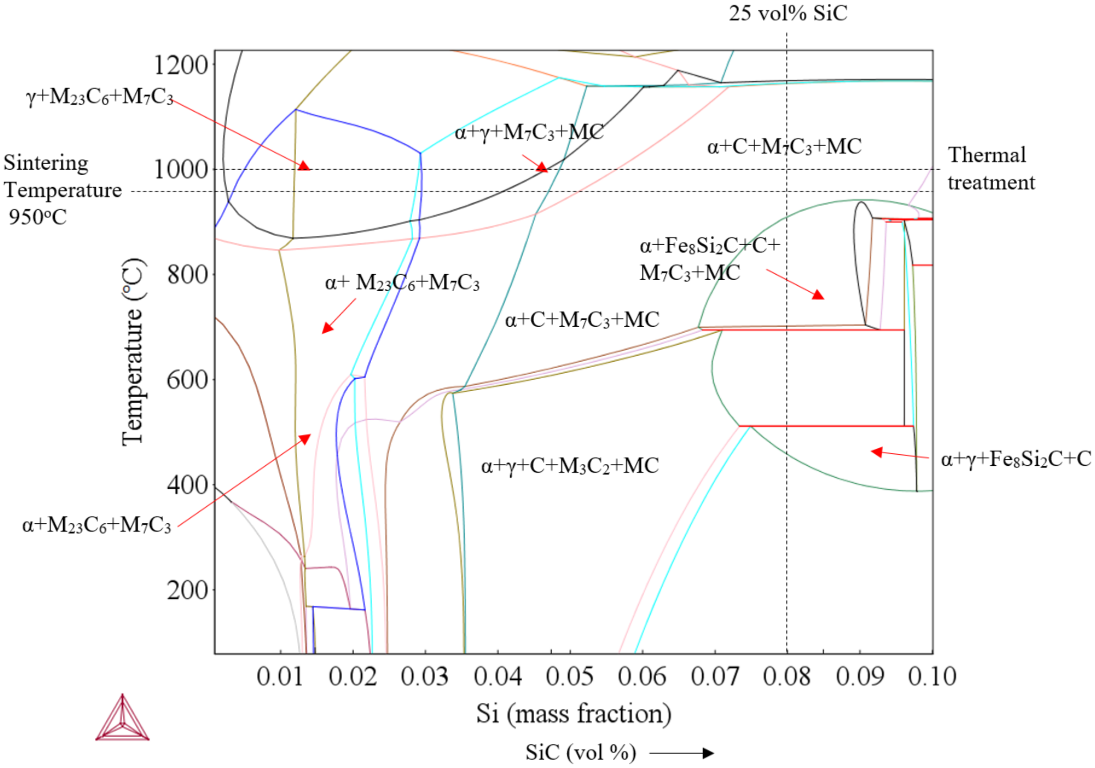

Fig. 37. Phase diagram of the $Cr_3C_2$@SiC-NFA system.

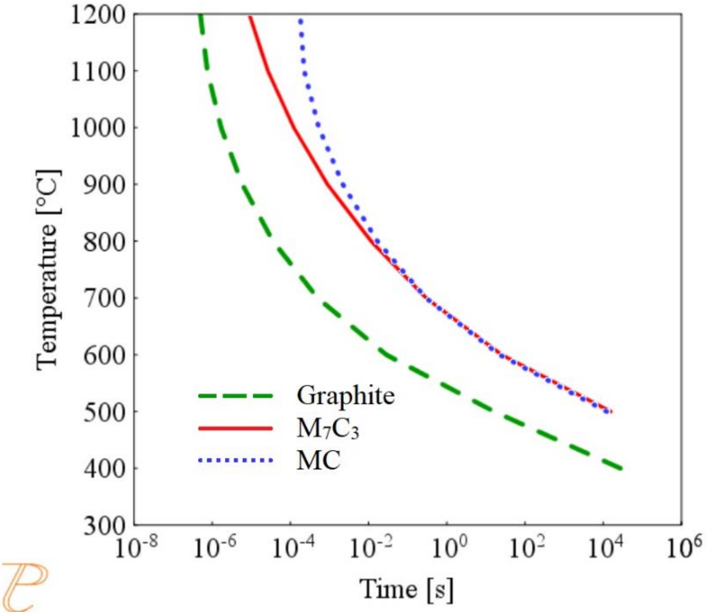

Fig. 38. TTT diagram of graphite, $M_7C_3$, and MC phases for the 25 vol% $Cr_3C_2$@SiC-NFA composite.

Precipitation simulations were carried out using the PRISMA module of the ThermoCalc software to estimate the size and volume fraction of the $M_7C_3$ and MC carbides before and after the thermal treatment. The estimated size of the $M_7C_3$ precipitate after sintering is much smaller than the actual size. The $M_7C_3$ precipitate size after the thermal treatment roughly matches with the one estimated using PRISMA as shown in Fig. 39a. The TTT diagram in Fig. 38 estimates nucleation of more $M_7C_3$ and MC type precipitates. This result can be correlated with the increase in the volume fraction of the precipitates.

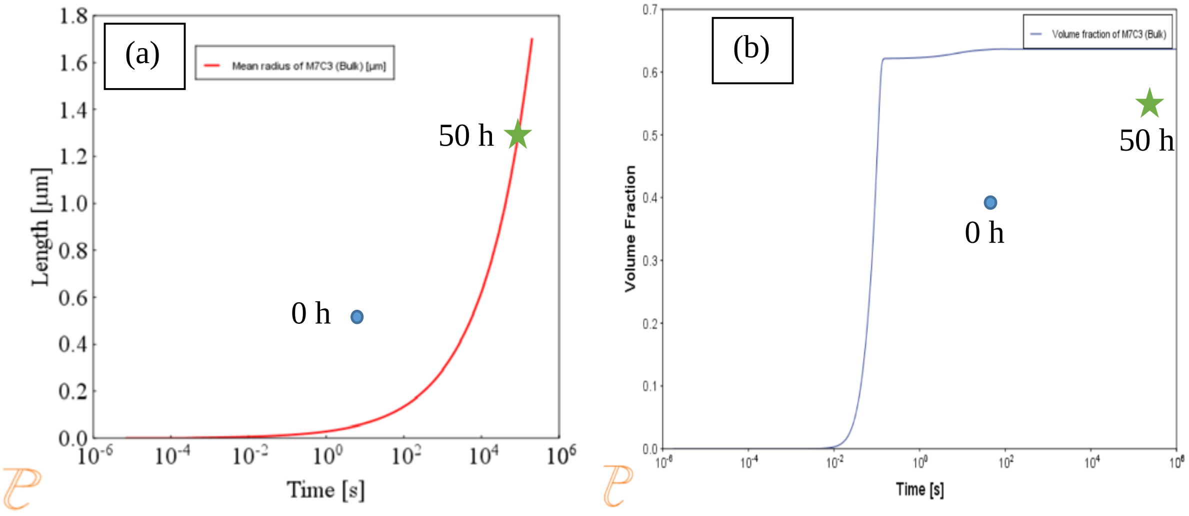

Fig. 39. ThermoCalc PRISMA simulations of the size and volume fraction of the $M_7C_3$ (a,b) and MC (c,d) precipitates.

The effect of the thermal treatment on the microstructure evolution of the 25 vol% $Cr_3C_2$@SiC-NFA composite can be divided into two parts. The first part is nucleation of the $M_7C_3$ and MC precipitates. The second part is the coarsening of the existing $M_7C_3$ and MC precipitates. Fig. 39 shows the ThermoCalc PRISMA simulation of the secondary precipitates after 50 hours of the thermal treatment. The coarsening of primary precipitates can be simulated using Thermo-Calc DICTRA software.

### 4.7. Damage profile using SRIM simulation for in-situ $Kr^{++}$ ion irradiation of SiC-C@NFA

Fig. 40a shows the plots for target displacements, vacancies, and replacement collisions obtained using the SRIM simulation. The target displacements are a sum of the target vacancies and replacement collisions. Figs. 40b and 40c show the $Kr^{++}$ ion distribution range and its trajectory along the depth direction respectively and indicate that the $Kr^{++}$ ions leave the TEM foil and do not get implanted, which is important in this experiment as the incident ions and target material are not identical. The dpa damage can be calculated using the target vacancy data obtained using the results in Fig. 40a according to Eq. (4).

$$dpa = f t d_v / d_a \tag{4}$$

Where f is fluence flux (ions/s.cm$^2$) and t is time.

$$d_v = \text{vacancies - SRIM output (number of vacancies/ion.Å)} \tag{5}$$

$$d_a = \text{atomic density (atoms/cm}^3\text{)} \tag{6}$$

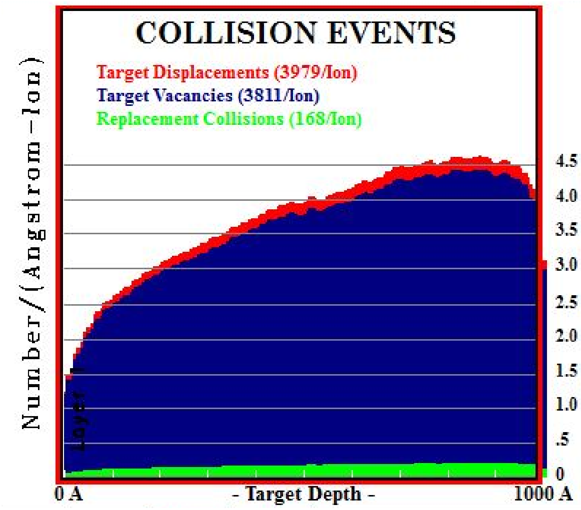

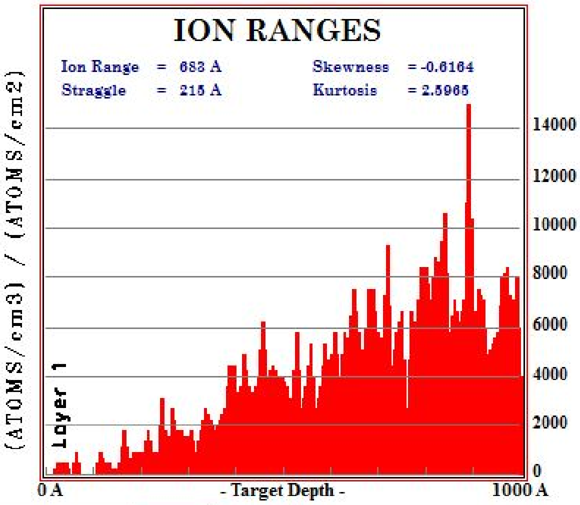

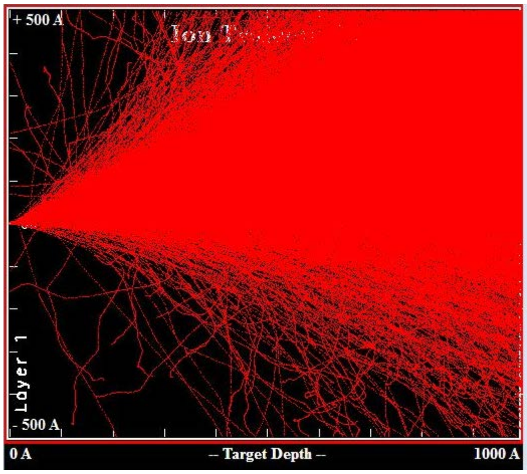

Fig. 40. SRIM simulation results showing (a) collision events, (b) $Kr^{++}$ ion distribution range, and (c) ion trajectory along the depth direction.

## 4.8. Defect evolution during ion irradiation

Fig. 41a shows the bright field TEM image of the 25 vol% SiC-C@NFA sample before ion irradiation (0 dpa) at 300°C. The dark region is Cr-rich ($M_7C_3$) and the gray region is Fe- and Si-rich (α-ferrite). Some defects can be observed in the α-ferrite region even before the ion irradiation, due to the ion milling method for the sample preparation. The TEM bright field image of the 25 vol% SiC-C@NFA composite with 3 dpa ion irradiation is shown in Fig. 41b. Some new defects can be observed in the Si-rich region (see the yellow arrows) at 3 dpa. Fig. 41c shows the TEM bright field image of the 25 vol% SiC-C@NFA composite at 5 dpa dose. The alignment of the defects in the α-ferrite grains can be observed at this dose level (see the blue arrows). Such spatial ordering of dislocations or loop string formation of dislocations has been observed earlier in some ion irradiated materials [67]. Fig. 41d shows the TEM bright field image of the 25 vol% SiC-C@NFA composite after 10 dpa dose. The sample looks completely damaged in the α-ferrite grains with a very high dislocation density. The $M_7C_3$ region is not damaged at all at all the dpa levels. This means that the $M_7C_3$ region possesses very high irradiation resistance compared to the Si-rich region.

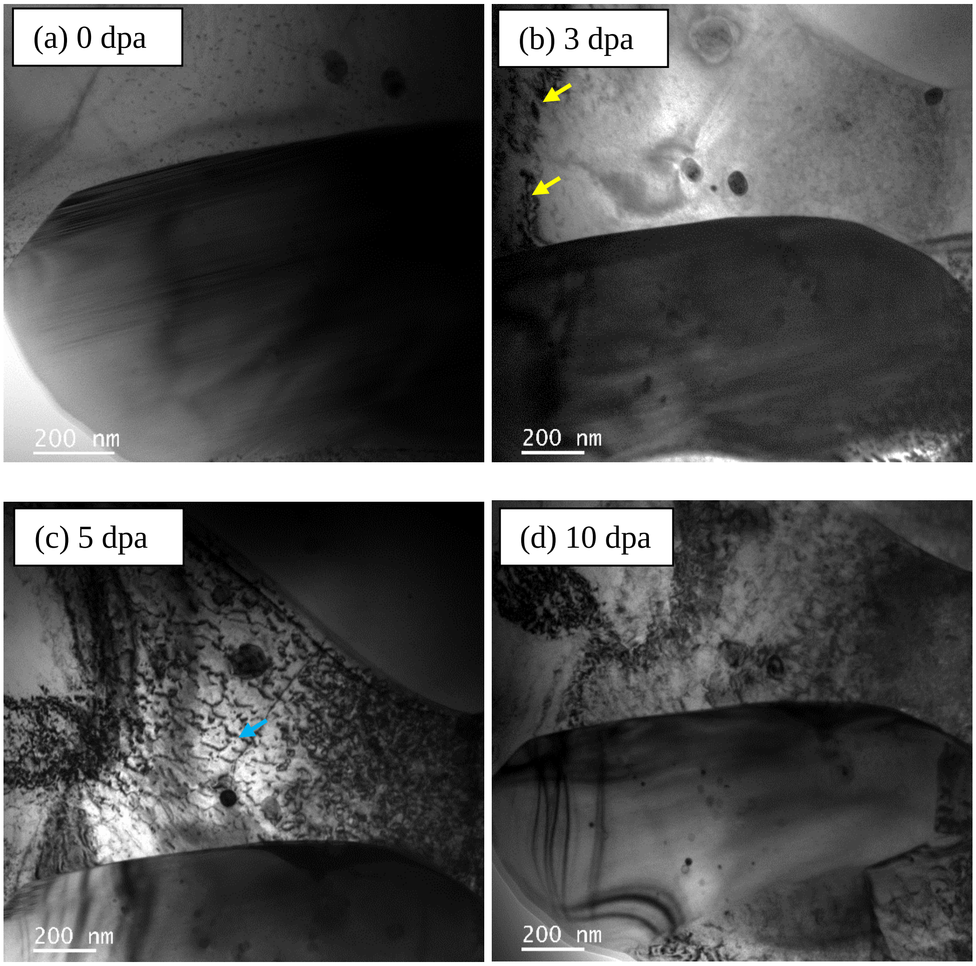

Fig. 41. In-situ ion irradiation of the 25 vol% SiC-C@NFA composite at 300$^{o}$C using different dose levels: (a) 0 dpa, (b) 3 dpa, (c) 5 dpa, and (d) 10 dpa.

Fig. 42 shows the STEM bright field image of the 25 vol% SiC-C@NFA composite after 10 dpa damage at 450$^{o}$C. The dislocation sizes are much larger and the dislocation loops are clearly visible, while the irradiation at 300$^{o}$C only generates nano-sized loops, shown only as small black dots in Fig. 42d. Many small precipitates can also be observed in Fig. 42 in addition to dislocations.

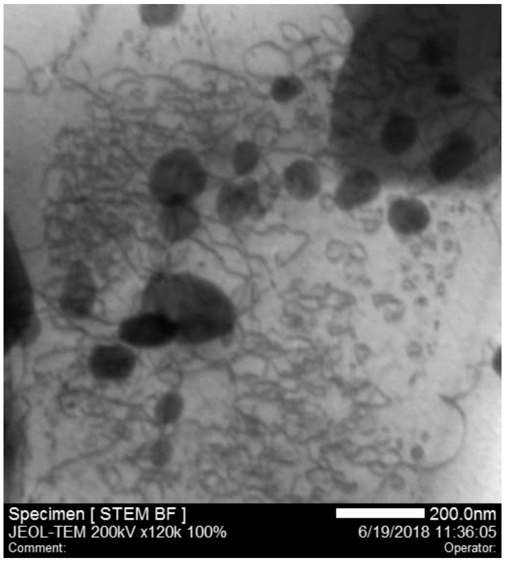

Fig. 42. STEM bright field image of the 25 vol% SiC-C@NFA composite after 10 dpa ion irradiation at 450°C.

## 4.9. Irradiation induced precipitation behavior

Fig. 43 shows the bright field TEM images of the 25 vol% SiC-C@NFA composite at different dose levels, 0, 0.2, 1, 3, 7, and 10 dpa. The 25 vol% SiC-C@NFA samples with 3, 7, and 10 dpa respectively show the formation of new precipitates due to the ion irradiation at 450°C. The EDS mapping of these new spherical precipitates in Fig. 44 shows Ti, W, and C enrichment. This means the precipitates are (Ti,W)C carbides. The number density of these (Ti,W)C carbides is plotted as a function of the dpa dose (Fig. 45). The dislocation number density shows an exponential increase at the 10 dpa dose level. The size of the precipitates is also much higher for the 10 dpa dose level compared to those at 3 and 7 dpa. This means that the combined effect of higher temperature (450°C) and $Kr^{++}$ ion irradiation has induced drastic nucleation and growth of the (Ti,W)C precipitates in the system.

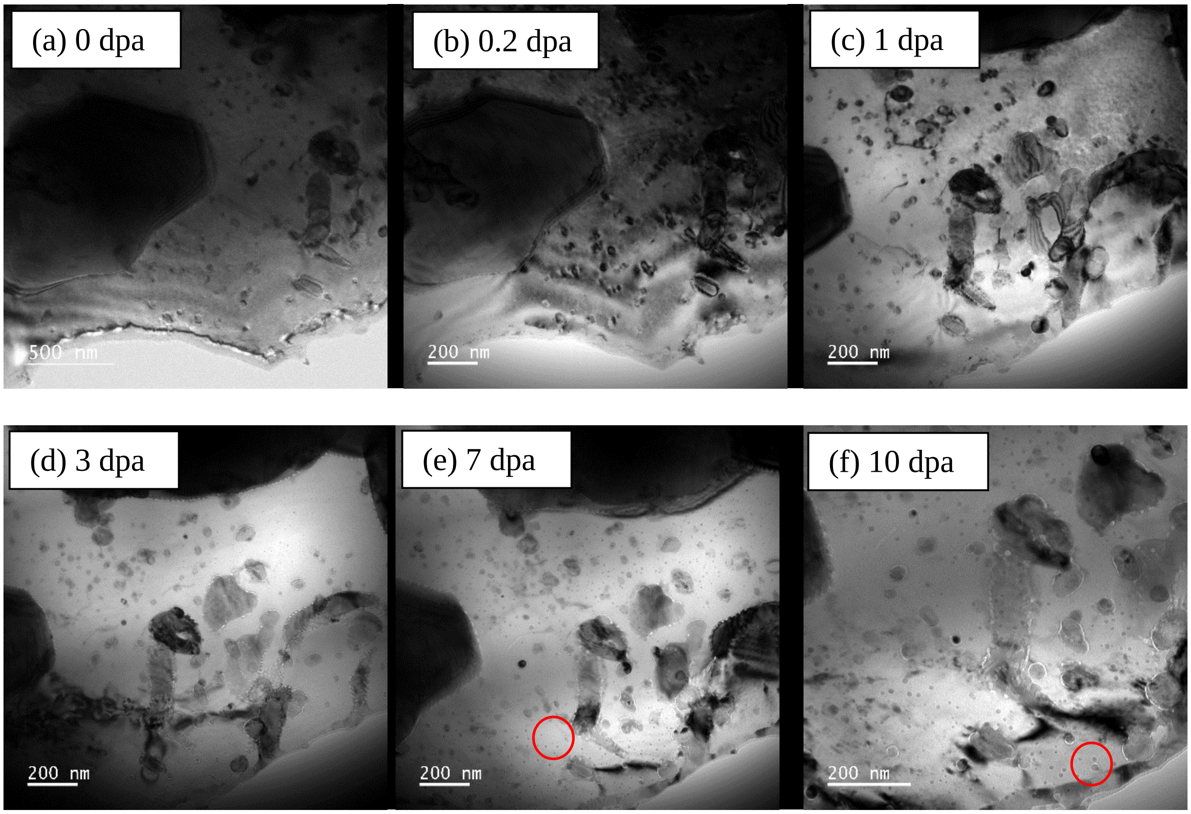

Fig. 43. In-situ ion irradiation of the 25 vol% SiC-C@NFA composite at 450°C using dose levels: (a) 0 dpa, (b) 0.2 dpa, (c) 1 dpa, (d) 3 dpa, (e) 7 dpa, and (f) 10 dpa (different mag).

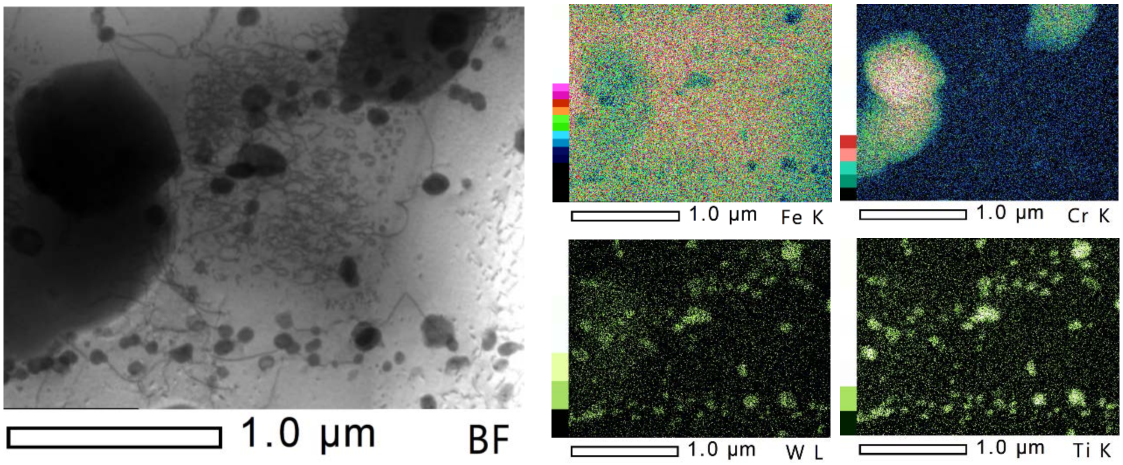

Fig. 44. EDS mapping of the 25 vol% SiC-C@NFA composite after 10 dpa ion dose at 450°C.

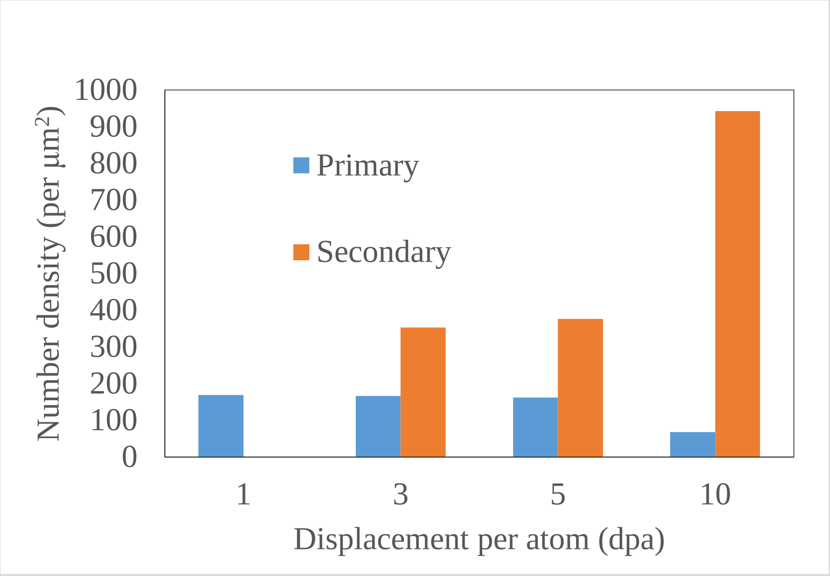

Fig. 45. Number density of primary and secondary (Ti,W)C precipitates with dpa damage.

After the ion irradiation at 300°C and 450°C with 10 dpa dose, the Cr-rich $M_7C_3$ phase shows no perceivable changes in the microstructure. This means the $M_7C_3$ phase is highly resistant to irradiation damage as compared to α-ferrite. The volume fraction of this phase is around 50% in the 25 vol% SiC-C@NFA system. Therefore, presence of such irradiation resistant phase is expected to improve the overall irradiation resistance of the SiC-C@NFA composite.

## 5. Conclusions

ODS powder is synthesized and the particle size distribution is characterized. The particle size distribution of ODS is wide and ranges from 2.98 μm to 394.24 μm. Large particles can be successfully removed by screening. The particle size of SiC is characterized. The SiC particle size distribution is narrow and ranges from 0.17 μm to 19.90 μm and is within the desired range. Large and heavy ODS particles can be successfully suspended in the SiC particle suspension. Viscosities of ODS-SiC co-suspensions with different solids loadings have been measured and the suspensions are feasible for casting purpose. Different ratios of SiC to ODS suspensions have been successfully made. Gradient SiC-ODS composites are cast and their optical images show the designed gradient structures with multiple layers of varying SiC/ODS ratios.

Several pure SiC (also named 0NFA) samples are sintered using SPS processes. The highest relative density reaches 90%, which is sintered at 2,050$^{o}$C for 10 mins holding using 80 MPa. Microstructure from the cross-sectional view for the sintered samples agrees with the density measurements.

SiC-NFA composites of 3 vol% NFA, 45 vol% NFA, and 70 vol% NFA have been prepared by spark plasma sintering under different sintering conditions. All the sintered samples have more than 90% density. After SPS, no new phase formation for high SiC or high NFA composites is detected. However, XRD patterns of the as-sintered 45 vol% NFA and 70 vol% NFA SiC composites have no peaks from SiC, which means that SiC has had severe reactions with NFA. The reaction products include iron silicides (e.g., $Fe_3Si$ and $Fe_5Si_3$) and chromium silicides (e.g., $CrSi_2$). The microstructure with three distinct phases confirms the reactions because the chemical compositions of all three phases are neither SiC nor NFA. Lowering sintering temperature and/or applying a coating on NFA should be pursued to avoid the reactions between SiC and NFA. On the other hand, the XRD patterns of the as-sintered 3 vol% NFA SiC composite only show the peaks related to the SiC. Overall, the sintering temperature plays a more important role than the holding pressure in the 3 vol% NFA SiC composite. Based on the SEM cross-sectional fracture micrographs, the most preferred sintering condition is 2,025$^{o}$C with 5 min holding under 80 MPa pressure, which yields 96% relative density for the 3 vol% NFA-SiC composite. The density of the high NFA composites increases with the sintering temperature but decreases with the SiC content. As the sintering temperature increases, pores shrink to small spherical shapes, nano $Y_2O_3$

disperses in NFA. The hardness of the high NFA composites is 13-14 GPa; the hardness of the high SiC composites is high, 37-41 GPa.

In order to avoid the severe reaction between the SiC and NFA during the sintering process, a Cr electroless coating on the NFA powder is proposed and studied under different conditions. A Cr electroless plating on the NFA powder is studied in six different conditions, which can avoid the severe reaction between the SiC and NFA during the sintering process. Examined by SEM and EDS, less sensitization and activation time (e.g., 1 min) and higher plating temperature (e.g., 80 $^{o}$C) lead to the highest concentration of Cr (28 wt%) with a relatively dense coating. The coating morphology and Cr content under different coating temperature, $CrCl_3$ concentration, and pH are examined by SEM and EDS respectively. A high $CrCl_3$ concentration (1.0 mol/L), a high electroless coating temperature (80°C), and a low pH (2.0) are desired.

The density, phase, microstructure, and mechanical properties of the pure SiC and NFA-SiC composites are studied. The density of the composite consistently increases with the increasing temperature. The addition of 2.5 vol% NFA facilitates the densification of the composite, while the addition of 5 vol% NFA hinders the densification of the composite. The fracture surface morphologies of the composite are constant with the density results. There are carbon rich phases in the NFA-SiC composites, which come from the reaction between NFA and SiC. The hardness of the composites is not affected by the sintering temperature. The addition of NFA does not decrease the hardness of the SiC matrix, but the iron rich phases that come from the reaction between NFA and SiC have a lower hardness. The fracture strength of the composites is derived from the hardness, so the fracture strength has the same trend as the hardness. The elastic modulus is also obtained. The addition of NFA does not decrease the elastic modulus of the composites.

Pure nanostructured ferritic steel alloy (NFA) and silicon carbide (SiC)-NFA composites sintered by SPS are also studied. The density of the composite consistently increases with the increasing temperature, but decreases with the addition of SiC. The microstructures of the composite are constant with the density results. Reaction phases and dispersed oxide nanoclusters are also presented. The phase transformation from $\alpha$-Fe to $\gamma$-Fe occurs during the sintering, the transformation temperature is higher for the NFA-SiC composites than for the pure NFA. The hardness of the composites is affected by three aspects. Sintering temperature generally increases the hardness of the composite. SiC improves the hardness of the composite but the reaction with Fe decreases the hardness. $\alpha \rightarrow \gamma$ Fe phase transformation decreases the hardness of the composite. The tensile strength has the same trend as the hardness. The addition of SiC decreases the elastic modulus of the composites because of the reaction between NFA and SiC.

A Cr layer is deposited on the NFA powder via electroless coating, and three parameters: temperature, $CrCl_3$ concentration, and pH value, have been studied. A higher temperature and a higher $CrCl_3$ concentration lead to a higher Cr content for the coated NFA powder, and pH value has complex effects on the quality of the Cr coating layer. The mechanism of the electroless coating and these effects have also been studied. Finally, an optimal coating condition has been provided.

After the thermal treatment of high NFA composites, these samples have similar oxidation surface (outer oxidized layer) of hematite $Fe_2O_3$ and the surface morphology evolution has the flake-donut-stub transformation with varied growth orientation depending on the thermal temperature. Both the pure NFA and the NFA-SiC composite samples have the inner oxidation layer of $(Fe,Cr)_3O_4$, while an additional small amount of $SiO_2$ phase is produced just for the NFA-SiC composites. Breakaway oxidation happens for the pure NFA samples by the intense depletion of chromium under the water vapor and leads to substantial iron oxide thickness. $SiO_2$ can act as an additional barrier for corrosion resistance in the NFA-SiC composite sample, resulting in considerably thinner oxidation layers. The oxidation mechanism for the NFA-SiC samples is strongly related to the thermal treatment temperature, sample density, and SiC addition. The NFA-SiC composites are promising nuclear cladding materials in harsh moist environments.

After the water vapor thermal treatment, the SPS sintered pure SiC and SiC-NFA composite samples are oxidized to two different protective $SiO_2$ phases, α-quartz and α-cristobalite, both of which play the critical role in corrosion resistance. α-quartz is from the oxidation of the silicides in the composites, while α-cristobalite is from the oxidation of the SiC matrix. However, the graphite phase in the composites is easily gasified and results in pores. Due to the strong corrosion resistance, only a couple of hundred nanometers thick $SiO_2$ layer is created. Both pure SiC and SiC-NFA composites have promising applications for corrosion resistance in high temperature moist environment.

The C@NFA particles have been made by precipitating sucrose on NFA particles followed by pyrolysis. SPS sintering of the SiC-C@NFA composites with 5 vol%, 15 vol%, and 25 vol% SiC are carried out at $850^{o}C$ and $950^{o}C$. Densification of the SiC-C@NFA composites is enhanced by increasing the temperature and the SiC content. The hardness increases with the SiC content at $850^{o}C$ but decreases with the SiC content at $950^{o}C$. All the composites have the major α-Fe phase without the presence of the SiC phase. In the reaction region, the Si element diffuses into NFA while C element aggregates. The break-down of the carbon coating layer during the sintering process compromises the ability of preventing the reactions between SiC and NFA. Fabrication of SiC-NFA composites by introducing a carbon barrier offers a new strategy for exploring new nuclear cladding materials.

The effectiveness of the $Cr_3C_2$ barrier layer on SiC particles is demonstrated and the SPS sintered $Cr_3C_2$@SiC-NFA composites are investigated. At 850°C, densification and hardness of the composites benefit from the increase of the SiC content. At 950°C, the densification is enhanced by more SiC content, while the hardness is compromised slightly accordingly. The $Cr_3C_2$@SiC-NFA composites have the hardness of 5-6 GPa, which are higher than zirconium base alloy and ODS alloys. All the $Cr_3C_2$@SiC-NFA composites show the main phase of α-Fe, but γ-Fe phase is present for the 5 vol% SiC composite at 950°C. The increase of the SiC content leads to the decrease of the lattice constant and hinders Fe $\alpha \rightarrow \gamma$ phase transformation. The Si element from the decomposition of SiC diffuses into the NFA matrix, while the C element forms aggregates due to its low solubility in NFA. The Si/Fe ratios in NFA matrix and reaction region are dependent on the sintering temperature and the SiC content in the composites.

The SiC-C@NFA composite is assessed to have improved microstructure due to reduced reactions between SiC and NFA from the carbon barrier. The elemental ratio of Si/Fe in the matrix region and reaction region of the $Cr_3C_2$@SiC-NFA composites is dependent on the sintering temperature and the SiC content in the composites. Self-ion irradiation with targeted 100 dpa damage for the high NFA and high SiC samples is conducted at room temperature. The high NFA sample is observed to have a rough surface after the ion irradiation but no elemental segregation or precipitation. Theoretical simulation for pure NFA and SiC is performed using SRIM 2013 in order to understand the ion irradiation process and predict the damage profile. The distribution of the implanted ions and induced recoils are produced, the energy transfer between the incident ions and the recoils are obtained, damage profiles are further predicted to be consistent with the experimental setup. The damage features of the NFA with Si diffusion are created by SRIM simulation, and the Si element in the NFA matrix is slightly lower in the maximum damage. It is expected that the as-sintered SiC-C@NFA composites to be irradiation tolerant.

Ion irradiation resistance of the SiC-NFA composites and high temperature water vapor corrosion resistance of the $Cr_3C_2$@SiC-NFA composites have been investigated from experimental and theoretical aspects for nuclear cladding. For the ion irradiation SiC-NFA samples, irregularly shaped ridges are observed on the surface due to the irradiation induced sputtering and can be explained by the B-H model. SRIM simulation reveals detailed damage profiles and energy transfers during the ion irradiation and the relatively lower displacement damage for the SiC-NFA composites. The Cr-rich and Si-rich regions are derived from the reactions between NFA and SiC. After the ion irradiation, the Cr-rich region has $Cr_{23}C_6$ crystalline phase but becomes amorphous under the ion irradiation; the Si-rich region is crystalline plus amorphous $Fe_3Si$. The defect concentration evolutions induced by the ion irradiation for NFA, $Fe_3Si$, and $Cr_{23}C_6$ are analyzed based on the defect reaction rate theory. For the thermally treated samples, the 5 vol% $Cr_3C_2$@SiC sample shows almost 40 times more oxidation damage than the 25 vol% $Cr_3C_2$@SiC sample for both 850$^{o}$C and 950$^{o}$C sintering conditions. Predominantly hematite phase is present for the 500$^{o}$C and 750$^{o}$C treated samples. $SiO_2$ phase can be observed for the 950$^{o}$C sintered 15 and 25 vol% $Cr_3C_2$@SiC samples after oxidation at 500$^{o}$C. For the thermal treatment at 1000$^{o}$C, the samples show more protective chromium rich layers with increasing $Cr_3C_2$@SiC content. For example, the 850$^{o}$C sintered 25 vol% $Cr_3C_2$@SiC sample shows $Cr_{1.7}Fe_{0.3}O_3$ phase, while the 950$^{o}$C sintered 25 vol% $Cr_3C_2$@SiC shows $FeCr_2O_4$ spinel phase. The 5 vol% $Cr_3C_2$@SiC sample shows more porous surface morphology compared to the higher $Cr_3C_2$@SiC content samples. γ-FCC phase formation in the 5 vol% $Cr_3C_2$@SiC sample is believed to be responsible for suppressing the protective $SiO_2$ formation. The results show promising applications of $Cr_3C_2$@SiC-NFA composites for harsh water vapor containing nuclear cladding environments.

Pure SiC and NFA-SiC composites are ion irradiated to 110 dpa. Isolated sand dune shapes are observed from the sample surface, which is explained based on the B-H model. The energy transfers and damage profiles from the SRIM simulation indicate that the NFA-SiC composites have slightly lower damage depth due to the Fe diffusion into the SiC lattice but maintain the same maximum displacement damage as the pure SiC. The damage layer in the SiC matrix is completely amorphous while the reaction product $(Fe,Cr)_3Si$ maintains the crystalline structure. The interphase boundary between the amorphous and crystalline SiC phases is ~100 nm thick and has numerous ion irradiation induced defect clusters. The defect evolutions in both SiC and $(Fe,Cr)_3Si$ are explained from the fundamental ion irradiation resistance point of view.

Water vapor thermally treated 5, 15 and 25 vol% $Cr_3C_2$@SiC-NFA composites under 500$^oC$, 750$^oC$ and 1000$^oC$ have been explored focusing on the cross-sectional microstructure and phase composition measurements. A three-layer cross-section structure is observed with $Fe_2O_3/(Fe,Cr)_2O_3$ phases in the outer layer, $Fe_3O_4$ phase in the middle layer and $Fe_3O_4+FeCr_2O_4+Fe_2W+Fe_2SiO_4$ phases in the inner layer. The phase diagram and diffusion data based on the Thermo-Calc simulation are further performed to obtain the fundamental understanding. Phase diagram shows the presence of γ-Fe (FCC) phase in the 5 vol% $Cr_3C_2$@SiC-NFA, while α-Fe (BCC) in the 15 and 25 vol% $Cr_3C_2$@SiC-NFA samples. The improved oxidation resistance in the 1000$^oC$ treated 15 and 25 vol% $Cr_3C_2$@SiC-NFA is attributed to the higher diffusivities of Cr and Si in the α-Fe phase than that in the γ-Fe phase. High diffusivities of Cr and Si significantly boost healing ability of the breakaway protective layer ($Cr_2O_3$ + $SiO_2$) and thus delay the onset of breakdown oxidation in the 15 and 25 vol% $Cr_3C_2$@SiC composites.

The oxidation behaviors of the pure NFA and SiC-C@NFA composites at three different temperatures, 500$^{o}$C, 750$^{o}$C, and 1000$^{o}$C, in a water vapor atmosphere, are studied. All the samples show negligible mass gain during the 500$^{o}$C and 750$^{o}$C treatments. The 25 vol% SiC-C@NFA composite shows the highest oxidation resistance during the 1000$^{o}$C treatment, 90% less than that of the pure NFA. The oxidized surfaces have a layered structure with two Fe-rich outer layers ($Fe_2O_3$, $Fe_3O_4$) and a Cr-rich inner layer ($Fe_3O_4$+$FeCr_2O_4$ +$Fe_2SiO_4$+$(Fe,Si)_2W$). A significant internal oxidation region is observed for the 1000$^{o}$C treated SiC-C@NFA composites due to the preferential oxidation of Cr- and Si-rich phases at the NFA grain boundaries. The improved oxidation resistance for the 25 vol% SiC-C@NFA composite is due to the high Cr and Si diffusivities and thus the $SiO_2$+$Cr_2O_3$ protective layer formation.

Ion irradiation of the $Cr_3C_2$@SiC-NFA composites has been implemented with highly energetic $Fe^{++}$ ions at room temperature up to ~205 dpa. The elemental distribution, phase composition, and defect structure are explored based on the TEM observations. Three different phases of $NFA|_{Si}$, C, and $Cr_3C_2$ are identified based on the electron diffraction. Crystalline $NFA|_{Si}$ is maintained and dislocation loops are produced after the ion irradiation. The C phase on the $NFA|_{Si}$ surface is more vulnerable to amorphization and the C phase in the $NFA|_{Si}$ matrix is partially amorphized. The $Cr_3C_2$ phase in the $NFA|_{Si}$ matrix is easily damaged and completely amorphized. These results offer useful guidance for nuclear cladding material development.

SPS sintered pure SiC and NFA-SiC (2.5 vol% NFA-97.5vol% SiC) materials have been irradiated by highly energetic $Si^{++}$ ions with a fluence of $2.2\times10^{18}$ ions·cm$^{-2}$. Surface morphologies and cross section microstructures are characterized using SEM and Raman spectroscopy. Under the ion irradiation, both sample surfaces undergo dramatic changes and form well defined dune microstructures. The irradiated layer has a consistent thickness of ~2.5 µm and matches with the

SRIM simulated damage depth of ~2.3 µm. The SiC composition in the irradiated layer has been completely amorphized. However, the silicide ($Fe_3Si$) in the NFA-SiC maintains the crystalline structure and demonstrates irradiation tolerance. The formation of the dune-shape structure can be explained with the B-H model. The NFA-SiC material shows increased irradiation resistance and should be promising candidate for nuclear cladding.

Microstructural evolutions in spark plasma sintered NFA and 25 vol% $Cr_3C_2$@SiC-NFA composite before and after thermal treatment at $1000^oC$ for 50 h are studied using SEM-EDS, EBSD, and Thermo-Calc® analysis. The grain sizes in the 25 vol% $Cr_3C_2$@SiC-NFA composite (~2 µm) are far smaller those in the NFA sample (~12 µm). Grain sizes for the 25 vol% $Cr_3C_2$@SiC-NFA composite slightly increase to ~4 µm after the $1000^oC$ treatment. Unique spinodal type microstructure can be observed for the 25 vol% $Cr_3C_2$@SiC-NFA composite with distinct Cr-rich and Si-rich phase separation. The current finding in the $Cr_3C_2$@SiC-NFA composite offers a useful guidance for developing new cladding composites.

SEM and subsequent digital image analysis indicate that higher concentrations of NFA enhances the formation of porosities in the evaluated samples. Elemental Si (<1%) is surprisingly identified in the pure SiC sample (Sample 1). The % NFA of Sample 2 (8.66 ± 1.41 NFA) is lower than that of Sample 3 (17.32 ± 1.94% NFA). Therefore, by means of digital image analysis it is validated that the concentration of the NFA dopant on the samples is proportional with the quantification results of the area fraction in the NFA phase.

The EBSD results shows that the NFA additions pin the grain boundaries to prevent grain growth during the high-temperature SPS process. Phase transformation from 6H to 4H SiC has been identified in all three samples and occurs most probably during the high-temperature fabrication. Further, it seems that the quantity of 4H-SiC grains increases with the increasing NFA content (up to 10% for Sample 3) because of the increasingly excess NFA sites. A random crystallographic distribution of 6H and 4H-SiC grains is determined for all three samples, although a slight indication of preference orientation in the pure SiC sample for 4H-SiC is noted.

Nanoindentation with multi cycle loading mode is conducted to explore the mechanical response of the $Cr_3C_2$@SiC-NFA material. The nanohardness data as a function of indentation depth in the reaction region and the NFA matrix of the $Cr_3C_2$@SiC-NFA material before and after the ion irradiation have been obtained. Both the NFA matrix and the reaction region have reduced hardness with the ion irradiation. This is probably because the ion irradiation further reduces the dislocation density and compromises the mechanical properties.

The APT technique is successfully applied in determining the chemistry from the NFA phase embedded in the SiC matrix. For the SiC phase, the measured low C content is attributed to the difference in the evaporation field between C and Si. Alternatively, the measured stoichiometry for Sample 2 (97.5% SiC-2.5% NFA) and Sample 3 (95% SiC-5% NFA) from the precipitate showed (Fe,Cr):Si~1. For the Sample 3 (95% SiC-5% NFA), Al, Mn, Ti, and W appear to be segregated at the interface of the precipitate and the SiC matrix.

Molten salt synthesis method (which is commonly used for preparation of nanoparticles) has been successfully used for preparing a homogeneous and dense $Y_2O_3$ coating on SiC. Investigation of the 1150$^oC$ sintered $Y_2O_3$@SiC-NFA composite using XRD shows that the $Y_2O_3$ coating is successful in suppressing the formation of detrimental iron silicides (FeSi, $Fe_3Si$). The $Y_2O_3$@SiC particles show retention in the composite with marginal dissolution in the NFA matrix.

Ion irradiation at 300$^oC$ temperature shows the evolution of dislocation loops and also loop string formation in α-ferrite phase above 5 dpa dose levels. The microstructure of the 300$^oC$ ion irradiated sample with 10 dpa dose shows complete damage in the α-ferrite phase. The sample with ion irradiation at 450°C shows much larger dislocation loops compared to that at 300°C. Ion irradiation at 450°C and above 3 dpa results in nucleation and growth of new (Ti,W)C precipitates. The $M_7C_3$ phase is highly resistant to the $Kr^{++}$ irradiation damage during the ion irradiation at both 300°C and 450°C temperatures.

## 6. Cost variance

| | | | Dec-14 | Jan-15 | Feb-15 | Mar-15 | Apr-15 | May-15 | Jun-15 | Jul-15 | Aug-15 | Sep-15 | |
|---|---|---|---|---|---|---|---|---|---|---|---|---|---|
| **Value Earned ($)** | | | 58,116 | 58,116 | 58,116 | 116,232 | 116,232 | 116,232 | 213,094 | 213,094 | 213,094 | 271,212 | |
| **Actual Costs ($)** | | | 152 | 12,177 | 12,177 | 50,170 | 61,978 | 78,180 | 95,232 | 134,397 | 134,397 | 161,553 | |
| **Cost Variance ($)** | | | 57,964 | 45,939 | 45,939 | 66,062 | 54,254 | 38,052 | 117,862 | 78,697 | 78,697 | 109,659 | |
| **Cost Variance** | | | 99.74% | 79.05% | 79.05% | 56.84% | 46.68% | 32.74% | 55.31% | 36.93% | 36.93% | 40.43% | |

| | Oct-15 | Nov-15 | Dec-15 | Jan-16 | Feb-16 | Mar-16 | Apr-16 | May-16 | Jun-16 | Jul-16 | Aug-16 | Sep-16 | |
|---|---|---|---|---|---|---|---|---|---|---|---|---|---|
| **Value Earned ($)** | 271,212 | 271,212 | 271,212 | 271,212 | 271,212 | 414,319 | 414,319 | 414,319 | 485,873 | 485,873 | 485,873 | 533,577 | |
| **Actual Costs ($)** | 161,553 | 179,223 | 184,825 | 195,712 | 218,680 | 225,523 | 245,043 | 248,047 | 270,154 | 291,098 | 312,533 | 323,579 | |
| **Cost Variance ($)** | 109,659 | 91,989 | 86,387 | 75,500 | 52,532 | 188,796 | 169,276 | 166,272 | 215,719 | 194,775 | 173,340 | 209,998 | |
| **Cost Variance** | 40.43% | 33.92% | 31.85% | 27.84% | 19.37% | 45.57% | 40.86% | 40.13% | 44.40% | 40.09% | 35.68% | 39.36% | |

| | Oct-16 | Nov-16 | Dec-16 | Jan-17 | Feb-17 | Mar-17 | Apr-17 | May-17 | Jun-17 | Jul-17 | Aug-17 | Sep-17 | |
|---|---|---|---|---|---|---|---|---|---|---|---|---|---|
| **Value Earned ($)** | 533,577 | 533,577 | 594,219 | 594,219 | 594,219 | 618,071 | 618,071 | 618,071 | 652,259 | 652,259 | 652,259 | 691,422 | |
| **Actual Costs ($)** | 336,579 | 365,899 | 380,071 | 406,791 | 414,190 | 429,337 | 445,496 | 474,046 | 482,856 | 511,206 | 528,382 | 553,950 | |
| **Cost Variance ($)** | 196,998 | 167,678 | 214,148 | 187,428 | 180,029 | 188,734 | 172,575 | 144,025 | 169,403 | 141,053 | 123,877 | 137,472 | |
| **Cost Variance** | 36.92% | 31.43% | 36.04% | 31.54% | 30.30% | 30.54% | 27.92% | 23.30% | 25.97% | 21.63% | 18.99% | 19.88% | |

| | Oct-17 | Nov-17 | Dec-17 | Jan-18 | Feb-18 | Mar-18 | Apr-18 | May-18 | Jun-18 | Jul-18 | Aug-18 | Sep-18 | Total |
|---|---|---|---|---|---|---|---|---|---|---|---|---|---|
| **Value Earned ($)** | 691,422 | 691,422 | 718,566 | 718,566 | 718,566 | 745,710 | 745,710 | 745,710 | 799,998 | 799,998 | 799,998 | 799,998 | 799,998 |
| **Actual Costs ($)** | 570,890 | 600,188 | 611,247 | 627,315 | 640,072 | 650,223 | 672,089 | 672,089 | 677,854 | 686,910 | 687,806 | 687,267 | 687,267 |
| **Cost Variance ($)** | 120,532 | 91,234 | 107,319 | 91,251 | 78,494 | 95,487 | 73,621 | 73,621 | 122,144 | 113,088 | 112,192 | 112,731 | 112,731 |
| **Cost Variance** | 17.43% | 13.20% | 14.94% | 12.70% | 10.92% | 12.80% | 9.87% | 9.87% | 15.27% | 14.14% | 14.02% | 14.09% | 14.09 |

**Note: There is a delay in posting the costs near the end of the project. By now, all the costs have been posted and the actual costs match with the value earned and the cost variance is 0%.**

## 7. Milestone variance

| | Nov-14 | Dec-14 | Jan-15 | Feb-15 | Mar-15 | Apr-15 | May-15 | Jun-15 | Jul-15 | Aug-15 | Sep-15 |
|---|---|---|---|---|---|---|---|---|---|---|---|
| Value Earned | - | - | 58,116 | 58,116 | 58,116 | 116,232 | 116,232 | 116,232 | 213,094 | 213,094 | 213,094 |
| Planned Value | 19,372 | 38,744 | 58,116 | 77,488 | 96,860 | 116,232 | 135,604 | 174,348 | 213,094 | 232,466 | 251,838 |
| Milestone Variance | -19,372 | -38,744 | - | -19,372 | -38,744 | - | -19,372 | -58,116 | - | -19,372 | -38,744 |
| Milestone Variance % | -100.00% | -100.00% | 0.00% | -25.00% | -40.00% | 0.00% | -14.29% | -33.33% | 0.00% | -8.33% | -15.38% |

| | Oct-15 | Nov-15 | Dec-15 | Jan-16 | Feb-16 | Mar-16 | Apr-16 | May-16 | Jun-16 | Jul-16 | Aug-16 | Sep-16 |
|---|---|---|---|---|---|---|---|---|---|---|---|---|
| Value Earned | 271,212 | 271,212 | 271,212 | 271,212 | 271,212 | 414,319 | 414,319 | 414,319 | 485,873 | 485,873 | 485,873 | 533,577 |
| Actual Costs | 295,063 | 318,914 | 342,765 | 366,617 | 390,468 | 414,319 | 438,170 | 462,022 | 485,873 | 509,724 | 533,575 | 557,428 |
| Cost Variance | -23,851 | -47,702 | -71,553 | -95,405 | -119,256 | - | -23,851 | -47,703 | - | -23,851 | -47,702 | -23,852 |
| Cost Variance % | -8.08% | -14.96% | -20.88% | -26.02% | -30.54% | 0.00% | -5.44% | -10.32% | 0.00% | -4.68% | -8.94% | -4.28% |

| | Oct-16 | Nov-16 | Dec-16 | Jan-17 | Feb-17 | Mar-17 | Apr-17 | May-17 | Jun-17 | Jul-17 | Aug-17 | Sep-17 |
|---|---|---|---|---|---|---|---|---|---|---|---|---|
| Value Earned | 533,577 | 533,577 | 594,219 | 594,219 | 594,219 | 618,071 | 618,071 | 618,071 | 652,259 | 652,259 | 652,259 | 691,422 |
| Actual Costs | 577,642 | 597,856 | 618,070 | 638,284 | 658,498 | 678,713 | 620,751 | 635,441 | 652,259 | 669,441 | 682,374 | 691,422 |
| Cost Variance | -44,066 | -64,280 | -23,852 | -44,066 | -64,280 | -60,643 | -2,681 | -17,371 | - | -17,182 | -30,115 | - |
| Cost Variance % | -7.63% | -10.75% | -3.86% | -6.90% | -9.76% | -8.93% | -0.43% | -2.73% | 0.00% | -2.57% | -4.41% | 0.00% |

| | Oct-17 | Nov-17 | Dec-17 | Jan-18 | Feb-18 | Mar-18 | Apr-18 | May-18 | Jun-18 | Jul-18 | Aug-18 | Sep-18 | Total |
|---|---|---|---|---|---|---|---|---|---|---|---|---|---|
| Value Earned | 691,422 | 691,422 | 718,566 | 718,566 | 718,566 | 745,710 | 745,710 | 745,710 | 799,998 | 799,998 | 799,998 | 799,998 | 799,998 |
| Actual Costs | 700,470 | 709,518 | 718,566 | 727,614 | 736,662 | 745,710 | 754,758 | 763,806 | 772,854 | 781,902 | 790,950 | 799,998 | 799,998 |
| Cost Variance | -9,048 | -18,096 | - | -9,048 | -18,096 | - | -9,048 | -18,096 | 27,144 | 18,096 | 9,048 | 0 | 0 |
| Cost Variance % | -1.29% | -2.55% | 0.00% | -1.24% | -2.46% | 0.00% | -1.20% | -2.37% | 3.51% | 2.31% | 1.14% | 0% | |

## 8. Schedule status

| Milestones | Anticipated completion date | Actual completion date |
|---|---|---|
| ODS synthesis and co-suspension of SiC-ODS -- The 9Cr NFA powder will be produced through mechanical milling and thermal treatment designed for high fracture toughness. The milling process will also be modified to produce very fine powders with reduced aggregate sizes. ODS alloy and SiC particles will be | 6/30/2015 | 6/30/2015 |

| | | |
|---|---|---|
| dispersed in an aqueous liquid using polymers such as poly(acrylic acid) as a dispersant. | | |
| Electroless coating of a protective layer on SiC | 6/30/2015 | 6/30/2015 |
| Casting of different composition suspensions to form gradient cladding composites --Use multi-step casting of different composition suspensions to form the proposed gradient cladding composites. | 9/30/2015 | 9/30/2015 |
| Spark plasma sintering of SiC-ODS -- Consolidate the gradient composites using extremely high heating rate spark plasma sintering. | 9/30/2015 | 9/30/2015 |
| Thermal treatment of the designed SiC-ODS gradient composites | 1/30/2016 | 3/31/2016 |
| Gradient composite property measurements | 5/31/2016 | 7/27/2016 |
| Corrosion tests and radiation damage | 9/30/2016 | 12/31/2016 |
| Characterization of nanocomposite microstructure evolution | 9/30/2017 | 6/30/2017 |
| Electron back scatter diffraction (EBSD) will be used to obtain crystallographic information about the phase distribution and identify any new phases formed in the matrix and at the SiC-ODS interfaces. | 9/30/2017 | 9/30/2018 |
| Atom probe tomography will be used to examine the new cladding material compositions atom by atom and identify where the species are in the composite and eventually build up the composition distribution in 3D. | 9/30/2017 | 9/30/2018 |

## 9. Products

Manuscripts to be submitted:

1. K. Bawane, K. Lu, "In-Situ $Kr^{++}$ Ion Irradiation of NFA and $Cr_3C_2$@SiC-NFA Composite at 300°C and 450°C," Journal of Nuclear Materials, to be submitted.
2. K. Bawane, K. Lu, "In-situ Ion Irradiation of a Silicon Carbide-Carbon Coated Nanostructured Ferritic Alloy System," Acta Materialia, to be submitted.

Peer-reviewed journal papers:

1. K. Bawane, K. Lu, "Microstructure Evolution for Nanostructured Ferritic Alloy with and without $Cr_3C_2$ Coated Silicon Carbide at High Temperatures," Materials and Design, submitted.

2. I. J. Van Rooyen, S. Meher, M. Bachhav, J. Rosales, K. Lu, “Advanced Characterization of SiC and SiC-Nanostructured Ferritic Alloy Composites,” Journal of Nuclear Materials, submitted.
3. K. Ning, K. Lu, “Understanding Ion Irradiation Resistance of a NFA|Si-$Cr_3C_2$-C Composite,” Journal of Materials Science, submitted.
4. K. Ning, K. Lu, R. Bortner, “High Dose Self-Ion Irradiated Silicon Carbide with Nanostructured Ferritic Alloy Aid,” Journal of Materials Science, accepted.
5. K. Bawane, K. Ning, K. Lu, “High Temperature Oxidation Behavior of Silicon Carbide-Carbon Coated Nanostructured Ferritic Alloy Composites in Water Vapor Environment,” Corrosion Science, 139, 206-214, 2018.
6. K. Ning, K. Lu, “Water Vapor Thermal Treatment of Silicon Carbide-Nanostructured Ferritic Steel Alloy (SiC-NFA) Composite Materials,” Applied Surface Science, 452, 248-258, 2018.
7. K. Ning, D. Bai, K. Lu, “Study of Self-Ion Irradiated Nanostructured Ferritic Alloy (NFA) and Silicon Carbide-Nanostructured Ferritic Alloy (SiC-NFA) Cladding Materials,” Nucl. Instr. Meth. Phys. Res. B, 427, 44-52, 2018.
8. K. Ning, K. Lu, “Ion Irradiation Effect on Spark Plasma Sintered Silicon Carbide Ceramics with Nanostructured Ferritic Alloy Aid,” Journal of the American Ceramic Society, 2018, 101:3662–3673.
9. K. Ning, K. Lu, “Water Vapor Thermal Treatment Effects on Spark Plasma Sintered Nanostructured Ferritic Alloy-Silicon Carbide Systems,” Journal of the American Ceramic Society, 101, 2208–2215, 2018.

10. K. Bawane, K. Ning, K. Lu, "High Temperature Treatment of $Cr_3C_2$@SiC-NFA Composites in Water Vapor Environment," Corrosion Science, 131, 365-375, 2018.
11. K. Ning, Z. Hu, K. Lu, "Spark Plasma Sintering of SiC-NFA Composites with Carbon Barrier Layer," Journal of Nuclear Materials, 498, 50-59, 2018.
12. K. Ning, Z. Hu, K. Lu, "Spark Plasma Sintering of Silicon Carbide (SiC)-Nanostructured Ferritic Alloy (NFA) Composites with Chromium Carbide Barrier Layer," Materials Science and Engineering A, 700 (17) 183–190, 2017.
13. Z. Hu, K. Ning, K. Lu, "Spark Plasma Sintered Silicon Carbide Ceramics with Nanostructured Ferritic Alloy as Sintering Aid," Materials Science and Engineering A, 682, 586-592, 2017.
14. Z. Hu, K. Ning, K. Lu, "Study of Spark Plasma Sintered Silicon Carbide with Nanostructured Ferritic Alloy Addition," Materials Science and Engineering A, 670, 75-80, 2016.

Conference proceeding paper:

1. K. Ning, Z. Hu, K. Lu, "Fabrication of New NFA-SiC Composites for Nuclear Applications," 2016 American Nuclear Society Winter Meeting Proceeding, ISBN: 978-0-89448-732-3.

Invited talks:

1. K. Lu, K. Bawane, K. Ning, "Nanostructured Ferritic Alloy-Silicon Carbide Composites for Nuclear Applications," 2019 TMS Annual Meeting & Exhibition, San Antonio, Texas, March 10-14, 2019.

2. K. Lu, K. Ning, “SiC-NFA Composites for Nuclear Cladding Applications,” Frontiers in Materials Processing Applications, Research and Technology, Bordeaux, France, July 9-12, 2017.
3. K. Lu, K. Ning, K. Bawane, “Fabrication of Novel NFA-SiC Composites for Nuclear Applications,” AFC Integration Meeting, Oak Ridge, TN, March 28-30, 2017.
4. K. Lu, “Material Needs and Developments in Energy Conversion, Harvesting, and Storage,” Fifth Biennial Conference of the Combined Australian Materials Societies 2016, Melbourne, Australia, December 6-8, 2016 (Keynote).
5. K. Lu, Z. Tang, Z. Hu, “Silicon Carbide and Oxide Dispersion Strengthened Steel Cladding Materials for Nuclear Applications,” Materials Science and Engineering 2015 Conference, Columbus, OH, October 4-8, 2015.

Conference presentations:

1. K. Bawane, K. Lu, J. Hu, M. Li, “In-situ Ion Irradiation Response of a Silicon Carbide-Carbon Coated Nanostructured Ferritic Alloy Composite,” 43rd International Conference and Exposition on Advanced Ceramics and Composites, Daytona Beach, FL, January 27-February 1, 2019.
2. K. Bawane, K. Lu, “Microstructural Evolution of NFA and $Cr_3C_2$@SiC-NFA Derived Materials Under Thermal Treatment,” Materials Science & Technology 2018, Columbus, OH, October 14-18, 2018.
3. K. Bawane, K. Lu, “High Temperature Oxidation of SPS Sintered NFA and $Cr_3C_2$-coated SiC-NFA Composites in Water Vapor Containing Environment,” Materials Science & Technology 2017, Pittsburgh, PA, October 9-12, 2017.

4. K. Ning, K. Lu, “Corrosion Resistance of Pure SiC and SiC-NFA Composite under High Temperature Water Vapor Conditions,” Materials Science & Technology 2017, Pittsburgh, PA, October 9-12, 2017.
5. K. Ning, K. Lu, “Study of SPS Sintered NFA and NFA-SiC Cladding Materials under High Dose Self-Ion Irradiation,” Materials Science & Technology 2017, Pittsburgh, PA, October 9-12, 2017.
6. K. Ning, K. Lu, “Water Vapor Effects on SPS Sintered Nanostructural Ferritic Alloy and Silicon Carbide Composite Materials,” Materials Research Society Fall Meeting, Boston, MA, November 27-December 2, 2016.
7. K. Ning, Z. Hu, K. Lu, “Fabrication of New NFA-SiC Composites for Nuclear Applications,” 2016 ANS Winter Meeting, Las Vegas, NV, November 6-10, 2016.
8. K. Lu, Z. Hu, K. Ning, “Oxide Dispersion Strengthened Steel and Silicon Carbide Composite Cladding Materials,” Materials Science & Technology 2016, Salt Lake City, UT, October 23-27, 2016.
9. K. Lu, Z. Hu, Z. Tang, “Oxide Dispersion Strengthened Steel and Silicon Carbide Composite Cladding Materials,” 2016 145th TMS Annual Meeting & Exhibition, Nashville, Tennessee. February 14-18, 2016.

**References**:

[1] S.J. Zinkle, K.A. Terrani, J.C. Gehin, L.J. Ott, L.L. Snead, Accident tolerant fuels for LWRs: a perspective, J Nucl Mater 448(1-3) (2014) 374-379.

[2] C. Matthews, C. Unal, J. Galloway, D.D. Keiser, S.L. Hayes, Fuel-cladding chemical interaction in U-Pu-Zr metallic fuels: a critical review, Nucl Technol 198(3) (2017) 231-259.

[3] J. Bair, M.A. Zaeem, M. Tonks, A review on hydride precipitation in zirconium alloys, J Nucl Mater 466 (2015) 12-20.

[4] B. Raj, M. Vijayalakshmi, P.R.V. Rao, K.B.S. Rao, Challenges in materials research for sustainable nuclear energy, MRS Bull 33(4) (2008) 327-337.

[5] S.J. Zinkle, G.S. Was, Materials challenges in nuclear energy, Acta Mater 61(3) (2013) 735-758.

[6] Y. Ueda, J.W. Coenen, G. De Temmerman, R.P. Doerner, J. Linke, V. Philipps, E. Tsitrone, Research status and issues of tungsten plasma facing materials for ITER and beyond, Fusion Eng Des 89(7-8) (2014) 901-906.

[7] S.J. Zinkle, L.L. Snead, Designing radiation resistance in materials for fusion energy, Annu Rev Mater Res 44 (2014) 241-267.

[8] S.J. Zinkle, A. Moslang, Evaluation of irradiation facility options for fusion materials research and development, Fusion Eng Des 88(6-8) (2013) 472-482.

[9] G.S. Was, Fundamentals of radiation materials science: metals and alloys, Springer, Berlin, 2007.

[10] W.J. Weber, Models and mechanisms of irradiation-induced amorphization in ceramics, Nucl Instrum Meth B 166 (2000) 98-106.

[11] I.A. Ovid'ko, A.G. Sheinerman, Irradiation-induced amorphization processes in nanocrystalline solids, Appl Phys A 81(5) (2005) 1083-1088.

[12] N. Swaminathan, D. Morgan, I. Szlufarska, Ab initio based rate theory model of radiation induced amorphization in β-SiC, J Nucl Mater 414(3) (2011) 431-439.

[13] G.R. Odette, M.J. Alinger, B.D. Wirth, Recent developments in irradiation-resistant steels, Annu Rev Mater Res 38 (2008) 471-503.

[14] S.J. Zinkle, J.T. Busby, Structural materials for fission & fusion energy, Mater Today 12(11) (2009) 12-19.

[15] I. Charit, K.L. Murty, Structural materials issues for the next generation fission reactors, JOM 62(9) (2010) 67-74.

[16] C.R.F. Azevedo, Selection of fuel cladding material for nuclear fission reactors, Eng Fail Anal 18(8) (2011) 1943-1962.

[17] P. Dubuisson, Y.d. Carlan, V. Garat, M. Blat, ODS Ferritic/martensitic alloys for Sodium Fast Reactor fuel pin cladding, J Nucl Mater 428(1-3) (2012) 6-12.

[18] S. Ukai, M. Fujiwara, Perspective of ODS alloys application in nuclear environments, J Nucl Mater 307–311 (2002) 749–757.

[19] S. Ukai, M. Harada, H. Okada, M. Inoue, S. Nomura, S. Shikakura, K. Asabe, T. Nishida, M. Fujiwara, Alloying design of dispersion strengthened ferritic steel for long life FBRs core material, J Nucl Mater 204 (1993) 65-73.

[20] N. Baluc, J.L. Boutard, S.L. Dudarev, M. Rieth, J.B. Correia, B. Fournier, J. Henry, F. Legendre, T. Leguey, M. Lewandowska, R. Lindau, E. Marquis, A. Muñoz, B. Radiguet, Z. Oksiuta, Review on the EFDA work programme on nano-structured ODS RAF steels, J Nucl Mater 417(1-3) (2011) 149-153.

[21] T.S. Byun, J.H. Kim, J.H. Yoon, D.T. Hoelzer, High temperature fracture characteristics of a nanostructured ferritic alloy (NFA), J Nucl Mater 407(2) (2010) 78-82.

[22] G.R. Odette, M.J. Alinger, B.D. Wirth, Recent developments in irradiation-resistant steels, Ann Rev Mater Res 38(1) (2008) 471-503.

[23] R.B. Rebak, Nuclear applications of oxide dispersion strengthened and nano-featured alloys: an introduction, JOM 66(12) (2014) 2424-2426.

[24] R.B. Rebak, Alloy selection for accident tolerant fuel cladding in commercial Light Water Reactors, Metal Mater Trans E 2(4) (2015) 197-207.

[25] M.P. Brady, Y. Yamamoto, M.L. Santella, L.R. Walker, Composition, microstructure, and water vapor effects on internal/external oxidation of alumina-forming austenitic stainless steels, Oxid Met 72(5-6) (2009) 311-333.

[26] L. Hallstadius, S. Johnson, E. Lahoda, Cladding for high performance fuel, Prog Nucl Energy 57 (2012) 71-76.

[27] B.A.P. Kurt A. Terrani, Chad M. Parish, Chinthaka M. Silva, Lance L. Snead, and, Y. Katoh, Silicon carbide oxidation in steam up to 2 MPa, J Am Ceram Soc 97(8) (2014) 2331-2353.

[28] B.A. Pint, K.A. Terrani, M.P. Brady, T. Cheng, J.R. Keiser, High temperature oxidation of fuel cladding candidate materials in steam–hydrogen environments, J Nucl Mater 440(1-3) (2013) 420-427.

[29] P. Yvon, F. Carré, Structural materials challenges for advanced reactor systems, J Nucl Mater 385(2) (2009) 217-222.

[30] Z. Hu, K. Ning, K. Lu, Study of spark plasma sintered nanostructured ferritic steel alloy with silicon carbide addition, Mater Sci Eng A 670 (2016) 75-80.

[31] Z. Hu, K. Ning, K. Lu, Spark plasma sintered silicon carbide ceramics with nanostructured ferritic alloy as sintering aid, Mater Sci Eng: A 682 (2017) 586-592.

[32] K. Ning, H.-F. Ju, K. Bawane, K. Lu, Spark plasma sintering of silicon carbide-nanostructured ferritic alloy composites with chromium carbide barrier layer, Mater Sci Eng A 700 (2017) 183-190.

[33] Z.H. Hu, K.J. Ning, K. Lu, Spark plasma sintered silicon carbide ceramics with nanostructured ferritic alloy as sintering aid, Mat Sci Eng A-Struct 682 (2017) 586-592.

[34] K. Ning, K. Bawane, Z. Hu, K. Lu, Spark plasma sintering of silicon carbide (SiC)-nanostructured ferritic alloy (NFA) composites with carbon barrier layer, J Nucl Mater 498 (2018) 50-59.

[35] K. Bawane, K. Ning, K. Lu, High temperature treatment of $Cr_3C_2$@SiC-NFA composites in water vapor environment, Corros Sci 131 (2018) 365-375.

[36] J.F. Ziegler, M.D. Ziegler, J.P. Biersack, SRIM - The stopping and range of ions in matter (2010), Nucl Instrum Meth B 268(11-12) (2010) 1818-1823.

[37] K. Ning, K. Lu, K. Bawane, Z. Hu, Spark plasma sintering of silicon carbide (SiC)-nanostructured ferritic alloy (NFA) composites with carbon barrier layer, Journal of Nuclear Materials 498 (2018) 50-59.

[38] K. Bawane, K. Ning, K. Lu, High temperature oxidation behavior of silicon carbide-carbon coated nanostructured ferritic alloy composites in air + water vapor environment, Corrosion Science 139 (2018) 206-214.

[39] A. PerezRodriguez, Y. Pacaud, L. CalvoBarrio, C. Serre, W. Skorupa, J.R. Morante, Analysis of ion beam induced damage and amorphization of 6H-SiC by Raman scattering, J Electron Mater 25(3) (1996) 541-547.

[40] S. Sorieul, J.M. Costantini, L. Gosmain, L. Thome, J.J. Grob, Raman spectroscopy study of heavy-ion-irradiated α-SiC, J Phys-Condens Mat 18(22) (2006) 5235-5251.

[41] G.Z. Yue, J.D. Lorentzen, J. Lin, D.X. Han, Q. Wang, Photoluminescence and Raman studies in thin-film materials: transition from amorphous to microcrystalline silicon, Appl Phys Lett 75(4) (1999) 492-494.

[42] Z.F. Sui, P.P. Leong, I.P. Herman, G.S. Higashi, H. Temkin, Raman analysis of light-emitting porous silicon, Appl Phys Lett 60(17) (1992) 2086-2088.

[43] A.A. Sirenko, J.R. Fox, I.A. Akimov, X.X. Xi, S. Ruvimov, Z. Liliental-Weber, In situ Raman scattering studies of the amorphous and crystalline Si nanoparticles, Solid State Commun 113(10) (2000) 553-558.

[44] G. Gouadec, P. Colomban, Raman Spectroscopy of nanomaterials: how spectra relate to disorder, particle size and mechanical properties, Prog Cryst Growth Ch 53(1) (2007) 1-56.

[45] J. Schwan, S. Ulrich, V. Batori, H. Ehrhardt, S.R.P. Silva, Raman spectroscopy on amorphous carbon films, J Appl Phys 80(1) (1996) 440-447.

[46] M. Yoshikawa, G. Katagiri, H. Ishida, A. Ishitani, T. Akamatsu, Raman-spectra of diamondlike amorphous-carbon films, J Appl Phys 64(11) (1988) 6464-6468.

[47] M. Gorman, S.A. Solin, Direct evidence for homonuclear bonds in amorphous SiC, Solid State Commun 15(4) (1974) 761-765.

[48] W. Bolse, J. Conrad, T. Rodle, T. Weber, Ion-beam-induced amorphization of 6H-SiC, Surf Coat Tech 74-75(1-3) (1995) 927-931.

[49] K.J. Ning, K. Lu, Ion irradiation effect on spark plasma sintered silicon carbide ceramics with nanostructured ferritic alloy aid, J Am Ceram Soc 101 (2018) 3662-3673.

[50] P. Sigmund, Theory of sputtering .I. sputtering yield of amorphous and polycrystalline targets, Phys Rev 184(2) (1969) 383-416.

[51] P. Sigmund, A mechanism of surface micro-roughening by ion bombardment, J Mater Sci 8(11) (1973) 1545–1553.

[52] R.M. Bradley, J.M.E. Harper, Theory of ripple topography induced by ion-bombardment, J Vac Sci Technol A 6(4) (1988) 2390-2395.

[53] S. Park, B. Kahng, H. Jeong, A.L. Barabasi, Dynamics of ripple formation in sputter erosion: nonlinear phenomena, Phys Rev Lett 83(17) (1999) 3486-3489.

[54] A. Keller, S. Facsko, W. Moller, Evolution of ion-induced ripple patterns on $SiO_2$ surfaces, Nucl Instrum Meth B 267(4) (2009) 656-659.

[55] U. Valbusa, C. Boragno, F.B. de Mongeot, Nanostructuring surfaces by ion sputtering, J Phys-Condens Mat 14(35) (2002) 8153-8175.

[56] B. Eren, L. Marot, I.V. Ryzhkov, S. Lindig, A. Houben, M. Wisse, O.O. Skoryk, M. Oberkofler, V.S. Voitsenya, C. Linsmeier, E. Meyer, Roughening and reflection performance of molybdenum coatings exposed to a high-flux deuterium plasma, Nucl Fusion 53(11) (2013) 113013[1-9].

[57] c. find), Standard practice for determining the inclusion or second-phase constituent content of metals by automatic image analysis, West Conshohocken, PA : ASTM2003.

[58] M.L. Dunzik-Gougar, I.J.v. Rooyen, C.M. Hill, T. Trowbridge, J. Madden, J. Burns, Effect of sample preparation techniques on grain boundary characterization of annealed TRISO-coated particles, Nucl Technol 196  111-120.

[59] W.M. Guo, H.N. Xiao, J.X. Liu, J.J. Liang, P.Z. Gao, G.M. Zeng, Effects of $B_4C$ on the microstructure and phase transformation of porous SiC ceramics, Ceram Int 41(9) (2015) 11117-11124.

[60] M.K. Miller, P. Angelini, A. Cerezo, K.L. More, Pulsed laser atom probe characterization of silicon-carbide, J Phys-Paris 50(C8) (1989) C8459-C8464.

[61] D.W. Saxey, Correlated ion analysis and the interpretation of atom probe mass spectra, Ultramicroscopy 111(6) (2011) 473-479.

[62] M. Thuvander, J. Weidow, J. Angseryd, L.K.L. Falk, F. Liu, M. Sonestedt, K. Stiller, H.O. Andren, Quantitative atom probe analysis of carbides, Ultramicroscopy 111(6) (2011) 604-608.

[63] A. García-Junceda, M. Campos, N. García-Rodríguez, J.M. Torralba, On the role of alloy composition and sintering parameters in the bimodal grain size distribution and mechanical properties of ODS ferritic steels, Metall Mater Trans A 47(11) (2016) 5325-5333.

[64] I. Hilger, F. Bergner, T. Weißgärber, D. Bouvard, Bimodal grain size distribution of nanostructured ferritic ODS Fe-Cr alloys, J Am Ceram Soc 98(11) (2015) 3576-3581.

[65] H. Zhang, Y. Huang, H. Ning, C.A. Williams, A.J. London, K. Dawson, Z. Hong, M.J. Gorley, C.R.M. Grovenor, G.J. Tatlock, S.G. Roberts, M.J. Reece, H. Yan, P.S. Grant, Processing and microstructure characterisation of oxide dispersion strengthened Fe–14Cr–0.4Ti–0.25$Y_2O_3$ ferritic steels fabricated by spark plasma sintering, J Nucl Mater 464 (2015) 61-68.

[66] J.H. Jang, C.-H. Lee, Y.-U. Heo, D.-W. Suh, Stability of (Ti,M)C (M=Nb, V, Mo and W) carbide in steels using first-principles calculations, Acta Mater 60(1) (2012) 208-217.

[67] S.L. Dudarev, K. Arakawa, X. Yi, Z. Yao, M.L. Jenkins, M.R. Gilbert, P.M. Derlet, Spatial ordering of nano-dislocation loops in ion-irradiated materials, 455 (2014) 16-20.

# Appendix A

## Digital Image Analysis

Table A-1. Digital image analysis of Sample 1.

| Image No. | Si/ Alloy (%) | SiC (%) | Porosity (%) |
|---|---|---|---|
| 1 | 0.53 | 99.465 | 0.04 |
| 2 | 0.98 | 99.02 | 0.14 |
| 3 | 0.85 | 99.15 | 0.20 |
| 4 | 0.92 | 99.08 | 0.16 |
| 5 | 0.58 | 99.42 | 0.24 |
| 6 | 0.59 | 99.41 | 0.46 |
| 7 | 1.12 | 98.88 | 0.04 |
| 8 | 0.53 | 99.47 | 0.018 |
| 9 | 0.4 | 99.6 | 0.11 |
| 10 | 0.59 | 99.41 | 0.23 |
| Avg | 0.71 | 99.29 | 0.16 |
| Std Deviation | 0.23 | 0.23 | 0.12 |

Table A-2. Digital image analysis of Sample 2.

| Image No. | Si/ Alloy (%) | SiC (%) | Porosity (%) |
|---|---|---|---|
| 1 | 31.43 | 68.57 | 0.124 |
| 2 | 29.37 | 70.63 | 0.035 |
| 3 | 21.44 | 78.56 | 0.168 |
| 4 | 27.5 | 72.5 | 0.406 |
| 5 | 17.83 | 82.17 | 0.043 |
| 6 | 21.45 | 78.55 | 0.509 |
| 7 | 24.76 | 75.24 | 0.253 |
| 8 | 27.67 | 72.33 | 0.02 |
| 9 | 24.57 | 75.43 | 0.023 |
| 10 | 22.75 | 77.25 | 0.28 |
| Avg | 24.88 | 75.12 | 0.19 |
| Std Deviation | 3.95 | 3.95 | 0.16 |

Table A-3. Digital image analysis of Sample 3.

| Image # | NFA (%) | SiC (%) | Porosity (%) |
|---|---|---|---|
| 1 | 15.05 | 84.95 | 2.47 |
| 2 | 15.16 | 84.84 | 3.08 |
| 3 | 15.77 | 84.23 | 3.84 |
| 4 | 15.16 | 84.84 | 3.67 |
| 5 | 17.35 | 82.65 | 2.07 |
| 6 | 16.9 | 83.1 | 5.66 |
| 7 | 18.8 | 81.2 | 1.95 |
| 8 | 18.95 | 81.05 | 2.47 |
| 9 | 20.7 | 79.3 | 2.61 |
| 10 | 19.43 | 80.57 | 3.78 |
| Avg | 17.33 | 82.67 | 3.16 |
| Std Deviation | 1.94 | 1.94 | 1.06 |